

# Micromachined tunable filters using MEMS switches and electromagnetic bandgap structures

Muhammad Faeyz Karim

2008

Muhammad, F. K. (2008). Micromachined tunable filters using MEMS switches and electromagnetic bandgap structures. Doctoral thesis, Nanyang Technological University, Singapore.

<https://hdl.handle.net/10356/41452>

<https://doi.org/10.32657/10356/41452>

# **Micromachined Tunable Filters using MEMS Switches and Electromagnetic Bandgap Structures**

**Muhammad Faeyz Karim**



**School of Electrical & Electronic Engineering**

A thesis submitted to the Nanyang Technological University  
in fulfillment of the requirement for the degree of  
Doctor of Philosophy

**2008**



**Statement of Originality**

I hereby certify that the work embodied in this thesis is the result of original research and has not been submitted for a higher degree to any other university or institution.

1/4/2008.  
Date

M Faeyz  
Muhammad Faeyz Karim

*This PhD thesis is dedicated to my Creator, Father, Mother,*

*Wife, Brother & Daughter*

***This PhD thesis is dedicated to my Creator, Father, Mother,  
Wife, Brother & Daughter***

## ACKNOWLEDGEMENTS

First and foremost, I would like to express my heart-felt appreciation to my supervisor Associate Professor Liu Ai Qun, who spared a lot of his time in giving me valuable guidance and advice. He has given me a lot of inspiration and innovative ideas for my research project. His greatness and forgiving nature has motivated me to continue to move forward.

I would also like to express my gratitude to Associate Professor Arokiaswami Alphones for his numerous advices and encouragement. Many thanks to Dr Chia Wai Mun for helping me out during my PhD study.

Special thanks to Dr Yu Aibin for his help in many aspects in the completion of my PhD work. I would also like to thank two of my friends, Mr Khoo Eng Huat and Mr Liang Xiaojun for their advice and teaching they had shared with me to brighten my research life. I would also like to take this opportunity to express my appreciation to all MEMS group member at the School of Electrical and Electronic Engineering, NTU for their friendships. They are Dr Wu Jiuhui, Dr Tang Min, Dr Zhang Xuming, Dr Li Jing, Dr Zhang Xinjun, Ms Palei Win, Dr Selin Teo Hwee Gee, Ms Sun Yi, Ms Cai Hong, and Dr Huang Jianmin.

This work would not be possible without the assistance of the technicians in Photonics Laboratory 1 and the Position and Wireless Technology Centre (PWTC).

I would also like to express my greatest gratitude to my parents and brother for keeping my moral high and thankful for their long lasting support. I would never forget to thank my wife Anum Faeyz and daughter Lamiyah Karim Kidwai for their

encouragement and support. Last but not the least, I appreciate all those who helped me in transforming my efforts into a fruitful endeavor.



## SUMMARY

Wireless communication is showing an explosive growth of emerging consumer and military applications of radio frequency (RF), microwave, and millimeter-wave circuits and systems. Future handheld devices, ground communications systems as well as communications satellites necessitate the use of highly integrated and reconfigurable RF front-ends, featuring small size, low weight, high performance and low cost. Continuing chip scaling has contributed to the extent that off-chip bulky passive RF components, like high-Q inductors, ceramic and SAW filters, varactor diodes and discrete PIN diode switches application have become limiting. Micro-machining or microelectromechanical systems (MEMS) technology is now rapidly emerging as an enabling technology to yield a new generation of high-performance RF-MEMS devices to replace these off-chip passives components in wireless communication sub-systems.

Thus, the objective of this thesis is to conduct research on high performance tunable RF filters using electromagnetic bandgap structures (EBG) with micromachined switches. MEMS capacitive switch is developed based on the result of coplanar waveguide (CPW) structure. Capacitance and inductance values of the MEMS switch are investigated using an equivalent electrical model. Mechanical design of the switch is also carefully studied. A new method of calculating the propagation characteristics of the periodic MEMS bridges is introduced. Switching time and the pull down voltage are calculated. The switch is fabricated using surface micromachining process on high resistive silicon substrate. The measurement results show that the contact area between the bridge and the dielectric layer is remarkably increased by 63%, and the isolation of the switch is improved by 2.2 dB at 15 GHz (29.3% improvement) and 10 dB at 40 GHz (58.8%

improvement) as compared to non-planarized case. The insertion loss of the switch is 0.1 dB at 15 GHz.

A bandstop filter using unloaded and loaded EBG structures is investigated. An equivalent circuit model for both the structures is derived based on circuit analysis theory. Frequency characteristics of the unit EBG cells are demonstrated using different circuit parameters. The propagation characteristics of the EBG structures are studied using a dispersion diagram. The filter is designed using commercial softwares IE-3D and Agilent's momentum. A new tunable EBG bandstop filter is realized using the MEMS capacitive bridges, where the bridges are loaded on the bandstop filter to act as variable capacitors when bias voltage is applied. The equivalent circuit model is developed and its values are extracted. The measurement results of the tunable bandstop filter show the tuning range from 19 GHz to 17.3 GHz. The insertion loss is well within 0.7 dB to 2.2 dB.

A new Fabry-Perot tunable bandpass is realized using the EBG structures. A defect cavity is created between periodic structures which behave as Fabry-Perot resonator. The dimensions of various parameters are studied and different types of phenomena such as variable bandwidth, high Q, and rejection level are observed. Fabry-Perot filters shows a narrow bandwidth and with good tunability range. The measurement results show that the center frequency at 0 V is 11.4 GHz, the insertion loss is 4 dB and the Q factor is 70. When the voltage is increased from 18 V to 34 V, the frequency shifts from 11.04 GHz to 10.4 GHz. A two state reconfigurable filter is designed and fabricated. The filter can provide both bandpass and bandstop function at the same resonant frequency by switching the DC contact MEMS switches. The measurement results show that the

insertion loss of the bandpass filter is 1.55 dB and for the bandstop, the band rejection level is  $> 20$  dB and the insertion loss in the pass band is 1.2 dB.

The successful implementation of the micromachined capacitive switches in the development of tunable bandstop filter, tunable bandpass filter and reconfigurable filter has evidenced the effectiveness of the MEMS technology in enhancing the specifications like low insertion loss, low cost, high tuning range and miniaturization.

# TABLE OF CONTENTS

<b>Acknowledgement</b>	i
<b>Summary</b>	iii
<b>Table of Contents</b>	vi
<b>List of Figures</b>	x
<b>List of Tables</b>	xvii
<b>List of Symbols</b>	xix
<b>1. Introduction</b>	1
1.1 Motivation	1
1.2 Objectives	4
1.3 Major contribution of the thesis	7
1.4 Organization of thesis	9
<b>2. Literature Review</b>	11
2.1 RF MEMS and switching circuits	11
2.1.1 RF MEMS switches	12
2.1.2 RF MEMS switching and reconfigurable circuits	15
2.2 Micromachined tunable filters	17



2.2.1	Basic concept of the filters	17
2.2.2	MEMS tunable filters	19
2.3	Electromagnetic bandgap (EBG) structures and filters	24
<b>3.</b>	<b>Micromachined Transmission Line and Capacitive Switches</b>	<b>32</b>
3.1	Silicon based CPW transmission line	33
3.1.1	Characteristics impedance and effective dielectric constant	33
3.1.2	Losses of CPW structure	39
3.1.2.1	Dielectric loss	40
3.1.2.2	Conductor loss	41
3.1.3	Effects of material properties	43
3.1.4	Effects of metal thickness	46
3.1.5	Experimental results and discussions	47
3.2	RF MEMS capacitive switches	50
3.2.1	Electrical modeling of the RF MEMS capacitive switch	50
3.2.2	Mechanical design	53
3.2.3	Planarization and roughness effect	64
3.2.4	Fabrication process flow of MEMS switches	65
3.2.5	Experimental results and discussions	67
3.3	Summary	73
<b>4.</b>	<b>Micromachined Tunable Bandstop Filters</b>	<b>74</b>
4.1	Electromagnetic bandgap (EBG) bandstop filter	75

4.1.1 Unloaded EBG structure	75
4.1.1.1 Influence of the unloaded aperture size	76
4.1.1.2 Influence of the transverse slot width	77
4.1.1.3 Influence of the transverse slot length	78
4.1.1.4 Modeling of the unloaded EBG	79
4.1.1.5 Propagation characteristics of the unloaded unit EBG	83
4.1.2 Loaded EBG structure	87
4.1.2.1 Effect of the square etched hole-Loaded EBG structure	88
4.1.2.2 Modeling of the loaded EBG structure	90
4.1.2.3 Propagation characteristics of the loaded unit EBG	95
4.1.3 Experimental results and discussions	97
4.1.3.1 Unloaded EBG bandstop filter	97
4.1.3.2 Loaded EBG bandstop filter	99
4.2 Design of the micromachined tunable bandstop filter	102
4.2.1 Experimental results and discussions	109
4.3 Summary	113
<b>5. Micromachined Tunable Bandpass Filters</b>	<b>115</b>
5.1 Fabry-Perot tunable filter	116
5.1.1 Theory of the Fabry-Perot tunable filter	116
5.1.2 Design of the EBG circuit	119
5.1.2.1 Capacitively loaded transmission line circuit analysis	120

5.1.3	Design of the Fabry-Perot tunable bandpass filter	124
5.1.3.1	Effect of number of EBG cells	126
5.1.3.2	Effect of the defect length	129
5.1.3.3	Effect of the slot dimension	129
5.1.3.4	Effect of propagation characteristics	130
5.1.4	Experimental results and discussions	133
5.2	A reconfigurable switching filter	138
5.2.1	Design of the reconfigurable filter	138
5.2.1.1	Unit reconfigurable cell structure and its modeling	140
5.2.1.2	Propagation characteristics of unit EBG cell	144
5.2.1.3	Effect of the bigger slot width	146
5.2.1.4	Effect of the transverse slot width	148
5.2.2	Experimental results and discussions	150
5.3	Summary	156
<b>6.</b>	<b>Conclusions</b>	<b>157</b>
6.1	Conclusions	157
6.2	Recommendations	159
	<b>Bibliography</b>	<b>160</b>
	<b>Author's Publications</b>	<b>177</b>

## LIST OF FIGURES

Fig. 2-1	Tunable millimeter wave filter using micromachined capacitor [54].	21
Fig. 2-2	Distributed MEMS transmission line for tunable filters [55].	21
Fig. 2-3	MEMS switchable interdigital coplanar filter [56].	22
Fig. 2-4	Miniature and tunable filters using MEMS [57].	23
Fig. 2-5	Bandstop EBG filter with sinusoidal variation of characteristics impedance [63].	25
Fig. 2-6	1-D electromagnetic bandgap microstrip transmission line [64].	26
Fig. 2-7	A beam-steerer using reconfigurable PBG ground plane [25].	27
Fig. 2-8	Non-uniform electromagnetic bandgap microstrip low pass filters [27].	28
Fig. 3-1	Schematic of the coplanar waveguide (CPW) structure.	34
Fig. 3-2	Characteristics impedance of coplanar waveguide versus different dielectric constant of the substrate material.	37
Fig. 3-3	Simulation result shows the top view for the current distribution of the coplanar waveguide.	37
Fig. 3-4	Simulation result of characteristics impedance of CPW with different metal thickness.	39
Fig. 3-5	Simulation results of attenuation constant due to conductor loss as a function of frequency of the CPW structure.	42
Fig. 3-6	Simulation results of coplanar waveguide attenuation constant versus characteristic impedance with the aspect ratio, $S/(S+2W)$ .	43
Fig. 3-7	Comparison of the simulated results of the HR silicon and LR silicon (a) Return loss, $S_{11}$ and (b) Insertion loss, $S_{21}$ .	45



Fig. 3-8	Simulation result of the conductor loss versus different conductor thickness $t$ at 20 GHz.	46
Fig. 3-9	Simulations results of the insertion loss versus different thickness of metal.	47
Fig. 3-10	Top view of SEM micrograph of the CPW structure.	48
Fig. 3-11	Measurement results of RF properties of the CPW using different material for the conductor layer (a) Return loss, $S_{11}$ , (b) Insertion loss, $S_{21}$ .	49
Fig. 3-12	Schematic of the RF capacitive switch; (a) Top view and (b) Cross sectional view	50
Fig. 3-13	Equivalent circuit of the capacitive shunt switch.	52
Fig. 3-14	Simulation results of frequency and capacitance versus different height of the bridge.	54
Fig. 3-15	Relationship between the applied voltage and the bridge height; (a) Pull in voltage effect and (b) Elimination of pull-in effect via varying different values of series capacitor.	56
Fig. 3-16	(a) Spring constant of the beam with $t/l = 0.005$ ; (b) Spring constant versus residual stress.	59
Fig. 3-17	Simulation results of the pull down time for different height of the bridge.	63
Fig. 3-18	Schematic view of contact condition after bridge pulled down.	65
Fig. 3-19	Fabrication process flow.	66
Fig. 3-20	Surface profiles of the capacitive shunt switch (a) Switch A: without fill-in photoresist and (b) Switch B: with fill-in photoresist	68

Fig. 3-21	SEM micrograph of the capacitive shunt switch (a) Switch A: without fill-in photoresist and (b) Switch B: with fill-in photoresist.	69
Fig. 3-22	Comparison of simulated and measured S-parameters for up state capacitance (a) Return loss, $S_{11}$ and (b) Insertion loss, $S_{21}$ .	71
Fig. 3-23	Comparison of simulated and measured S-parameters of down state capacitance (a) Return loss, $S_{11}$ and (b) Insertion loss, $S_{21}$ .	72
Fig. 4-1	Schematic of unloaded unit EBG structure.	75
Fig. 4-2	Simulated S-parameters of the unloaded unit EBG structure versus variation of square aperture size $a$ .	77
Fig. 4-3	Simulated S-parameter of the unloaded unit EBG structure versus variation of the transverse slot width $d_s$ .	78
Fig. 4-4	Simulated S-parameter of the unloaded unit EBG structure versus variation of the transverse slot length $w_s$ .	79
Fig. 4-5	Equivalent parallel resonant circuit for the unloaded unit EBG structure.	80
Fig. 4-6	Comparison on parameter extraction and EM simulation results of the unloaded unit EBG structure.	82
Fig. 4-7	Schematic of unloaded EBG bandstop filter	84
Fig. 4-8	Simulated dispersion diagram of unloaded EBG structure with $d_s = 60 \mu m$ and $a = 500 \mu m$ .	85
Fig. 4-9	Simulation results of complex characteristics impedance of the unloaded unit EBG structure.	87
Fig. 4-10	Schematic of the loaded unit EBG structure.	88

Fig. 4-11	Simulated S-parameter of the loaded unit EBG structure, versus different center slot within the ring $b$ .	89
Fig. 4-12	Comparison on parameter extraction and EM simulation results of the loaded unit EBG structure.	91
Fig. 4-13	Equivalent circuit for a unit cell of the cascaded parallel resonant EBG structure.	91
Fig. 4-14	Schematic of loaded EBG bandstop filter	95
Fig. 4-15	Simulated dispersion diagram of the loaded unit EBG structure.	96
Fig. 4-16	Complex characteristics impedance of the unloaded unit EBG structure.	96
Fig. 4-17	SEM graph of the unloaded EBG bandstop filter.	98
Fig. 4-18	Comparison of measurement and the simulation results (EM and circuit simulations) of the unloaded EBG bandstop filter.	98
Fig. 4-19	SEM graph of the loaded EBG bandstop filter.	99
Fig. 4-20	Comparison of the measurement and simulation results of the loaded EBG bandstop filter.	100
Fig. 4-21	Comparison of the measurement results of the loaded and unloaded EBG bandstop filters.	101
Fig. 4-22	Simulation results of number of the unit EBG cells; (a) Insertion loss and rejection level; (b) Bandwidth variation.	103
Fig. 4-23	Schematic of the tunable bandstop filter using MEMS bridges.	104
Fig. 4-24	Equivalent parallel resonant circuit for the tunable bandstop filter.	105

Fig. 4-25	Simulation result of the current distribution in the micromachined tunable filter; (a) Overview and (b) Zoom view.	106
Fig. 4-26	Dispersion diagram of the micromachined brides loaded on CPW transmission line (a) At a period of $200\ \mu m$ (b) At a period of $400\ \mu m$ (c) at a period of $600\ \mu m$ .	108
Fig. 4-27	SEM micrograph of the fabricated MEMS tunable EBG bandstop.	110
Fig. 4-28	Comparison of the simulation and measurement results of the S-parameters of tunable EBG bandstop filter (zero bias voltage).	110
Fig. 4-29	Measurement results of the tunable bandstop filter (a) Return loss, $S_{11}$ , and (b) Insertion loss, $S_{21}$ .	111
Fig. 5-1	Schematic representation of Fabry-Perot filter with multilayer parallel plates.	117
Fig. 5-2	Equivalent circuit of periodically loaded transmission line.	120
Fig. 5-3	Schematic of EBG Fabry-Perot filter.	124
Fig. 5-4	Equivalent circuit model of the EBG Fabry-Perot tunable filter.	125
Fig. 5-5	Simulation results for the relationship between the Q factor versus the number of EBG cells.	126
Fig. 5-6	Simulation results versus the number of EBG holes.	127
Fig. 5-7	Simulation result of the varying defect lengths (a) For $n = 4$ EBG cells; and (b) For $n = 6$ EBG cells.	128
Fig. 5-8	Simulation result of the varying slot length, $t$ .	130
Fig. 5-9	Dispersion diagram of EBG F-P filter (a) Attenuation curve (b) Propagation curve.	131
Fig. 5-10	Simulation results of current distribution of the tunable F-P filter at 11.4 GHz (a) Overview and (b) Magnified image of the region as highlighted in (a).	132



Fig. 5-11	Comparison between the simulation and measurement results (a) Return loss, $S_{11}$ (b) Insertion loss, $S_{21}$ .	134
Fig. 5-12	Tunable Fabry-Perot EBG filter (a) Photograph of the F-P filter (b) Enlarged view of MEMS bridges.	135
Fig. 5-13	Measurement result of the tunable F-P EBG filter (a) Return loss, $S_{11}$ (b) Insertion loss, $S_{21}$ .	136
Fig. 5-14	Schematic of the MEMS reconfigurable filter.	138
Fig. 5-15	Schematic of the unit reconfigurable cell structure.	139
Fig. 5-16	Equivalent circuit model of the unit reconfigurable cell structure.	140
Fig. 5-17	Comparison of parameter extraction and EM simulation results of the unit reconfigurable cell (dotted line).	141
Fig. 5-18	Comparison of circuit simulation results and EM simulation results of the unit reconfigurable cell.	142
Fig. 5-19	Simulation results of the current distribution for reconfigurable filter; (a) Bandpass response, (b) Bandstop response.	143
Fig. 5-20	Simulated dispersion characteristics of unit cell structure; (a) Bandstop filter phenomena; (b) Bandpass filter phenomena.	145
Fig. 5-21	Simulated phase response of the reconfigurable filter.	146
Fig. 5-22	Simulation results of the change in the bigger slot width $b$ , (a) Return loss, $S_{11}$ and , (b) Insertion loss, $S_{21}$ .	147
Fig. 5-23	Simulation results of the change in the transverse slot width $t$ , (a) Return loss, $S_{11}$ and , (b) Insertion loss, $S_{21}$ .	149
Fig. 5-24	SEM graph of the reconfigurable filter with MEMS switches, (a) Overview of the reconfigurable filter, and (b) Magnified image of the region with rectangular highlighted in (a).	151

Fig. 5-25	The equivalent circuit of the reconfigurable filter.	152
Fig. 5-26	Cross section of the MEMS DC contact switch.	152
Fig. 5-27	Simulation results of the S-parameters of the reconfigurable filter (a) OFF state of switch, reconfigurable filter behaves as a bandpass filter and (b) ON state of switch, reconfigurable filter behaves as a bandstop filter.	153
Fig. 5-28	Measurement results of S-parameters of the reconfigurable filter (a) OFF state of switch, reconfigurable filter behaves as a bandpass filter and (b) ON state of switch, reconfigurable filter behaves as a bandstop filter.	155

## LIST OF TABLES

Table 1-1	Performance comparison of RF MEMS, PIN diodes and FETs as RF switches	2
Table 1-2	Specifications of the MEMS capacitive switch.	5
Table 1-3	Specifications of the MEMS tunable bandstop filter.	6
Table 1-4	Specifications of the MEMS tunable bandpass filter.	7
Table 2-1	Different configurations of MEMS switches.	13
Table 2-2	Literature survey of RF MEMS tunable filters.	20
Table 3-1	Properties of the dielectric materials.	41
Table 3-2	Designed parameters of the capacitive switch.	51
Table 3-3	Comparison of down-state isolations and capacitances.	70
Table 4-1	Extracted equivalent circuit parameters for the unloaded unit EBG structure, with variation in square aperture size $a$ .	81
Table 4-2	Extracted equivalent circuit parameters for the unloaded EBG unit structure, with variation in the transverse slot width $d_s$ .	83
Table 4-3	Extracted equivalent circuit parameters for the loaded EBG unit structure.	93
Table 4-4	Extracted equivalent circuit parameters for the tunable EBG structure.	105
Table 5-1	Extracted circuit parameters for tunable F-P EBG filter.	125

Table 5-2	Measurement results of the tunable F-P EBG filter.	137
Table 5-3	Extracted circuit parameters of the reconfigurable filter.	141
Table 5-4	Extracted parameters for the change in the bigger slot width $b$ .	148
Table 5-5	Extracted parameters for the change in the transverse slot $t$ .	150

# LIST OF SYMBOLS

$\epsilon_{eff}$	Effective dielectric constant
$Z_0$	Characteristics impedance
$\alpha$	Attenuation
$K$	Complete elliptic integral of first kind
$\epsilon_0$	Permittivity of free space
$\alpha_d$	Dielectric loss
$\lambda_0$	Free space wavelength
$\epsilon_r$	Relative permittivity
$\tan \delta_e$	Loss tangent
$\sigma$	Bulk conductivity
$\alpha_c$	Conductor loss
$\delta$	Skin depth
$\omega$	Angular frequency
$E$	Young's modulus
$I$	Moment of inertia
$\nu$	Poisson's ratio
$\mu$	Air viscosity

$\omega_c$	3 dB cut-off angular frequency
$k_0$	Wave number
$\eta_0$	Intrinsic impedance
$\beta$	Propagation constant
$\lambda_g$	Guided wavelength

# **CHAPTER1**

## **INTRODUCTION**

### **1.1 Motivation**

The device development based on microelectromechanical systems (MEMS) for radio-frequency (RF) applications, or RF MEMS, have gained rapid ground during the last five years. This new technology has made possible discrete micro-scale mechanical circuits, which are capable of low-loss filtering, mixing, switching, and frequency generation [1-3]. The real accomplishment is the beginning of integration of RF MEMS together with the integrated circuits (IC). In this way, the industry is making measurable strides toward a major intermediate objective of a single-chip transceiver [3-6]. This PhD research focuses on the development of high performance and low cost MEMS switches and MEMS tunable filters which can be integrated onto a single chip.

Many RF MEMS components, such as switches, voltage tuned capacitors, high quality factor micromachined inductors, and MEMS resonators and filters are currently under development in laboratories [3]. Among these, MEMS switches are attracting vast interest from the research community for RF applications. MEMS switches have several advantages compared with the traditional FET or p-i-n diode switches [7-11]. First, RF MEMS switches with low up-state capacitance (series switches) and low insertion loss at microwave frequencies usually offer more superior performance compared to solid-state



Chapter 1 Introduction

switches for low to medium power applications. Second, compared with p-i-n diode the contact resistance associated with ohmic contacts is eliminated, resistive losses in the device can be reduced significantly. Current and power consumption of the switches are also negligible. Third, without a semiconductor junction, RF MEMS switches are linear devices. The switches are mechanically stiff (large spring constant design) which can tolerate large RF voltage swings without generating any significant levels of intermodulation products. They are simply near-ideal elements for tunable filters and matching networks. Table 1-1 compares the performance of the MEMS switches with the p-i-n diode and FET's. RF MEMS switches demonstrate over all superiority in term of performance.

Table 1-1 Performance comparison of RF MEMS, PIN diodes and FETs as RF switches.

Parameters	RF MEMS	PI N	FET
Current (mA)	0	3-20	0
Power consumption, (mW)	0.05-0.1	5-100	0.05-0.1
Switching time	1-300 $\mu$ s	1-100 ns	1-100 $\mu$ s
C <sub>up</sub> (series), fF	1-6	40-80	70-140
R <sub>s</sub> (series), $\Omega$	0.5-2	2-4	4-6
Capacitance ratio	40-500	10	N/A
Isolation (10-40 GHz)	Very high	High	Medium
Loss (dB)	0.05-0.2	0.3-1.2	0.4-2.5
Third order intercept point (dBm)	66-80	27-45	27-45

## Chapter 1 Introduction

---

The goal of many commercial and military systems is the ability to easily reconfigure the frequency of operation [12-14]. However, a single filter cannot be used to fulfill this reconfigurability for its operating bands. The use of multiple filters occupy a large surface area, therefore employing tunable filters constitute an interesting and logical solution to this problem. The filters must be custom machined, carefully assembled, tuned and calibrated. Typically tracking filters are mechanically tuned by adjusting the cavity dimensions of the resonator or magnetically altering the resonant frequency of a ferromagnetic YIG element [14-15], which have multioctave bandwidths and high quality-factor (Q) resonators [16]. They also consume considerable amount of DC power (0.75–3 W), and their linearity is not high. Neither of these approaches can result in miniaturization or produced in large volumes for wireless communication products. Solid-state varactors can provide a wide tuning range, but there are losses and linearity problems at microwave frequencies [17-18]. The semiconductor based varactors have a quality factor (Q) as low as 2 or 3. They can be associated with fixed capacitors in series in order to increase the Q of the resulting resonator, but in this case the tuning range is decreasing. In general, losses can reduced by using a weak coupling between the resonator and the varactor; higher Q means lower tuning. In contrast, employing MEMS technology enables the construction of miniaturized tunable filters that exhibit low loss, low-power consumption, and excellent linearity. The successful application of MEMS fabrication process can reduce the overall size, weight, and cost of RF integrated systems and making them attractive for many commercial and military applications [1-3].

Electromagnetic bandgap (EBG) structures, also known also as photonic bandgap (PBG) structures, are considered extensively for applications in microwave devices,

## Chapter 1 Introduction

---

especially for implementation in high-impedance surfaces and frequency-selective surfaces (FSSs) [19-22]. Planar EBG structures offer tremendous application possibilities for active and passive devices because these structures exhibit wide bandpass and band rejection properties at microwave and millimeter wave frequencies [23-27]. For compact design, the passband of the EBG structures is used as a slow wave medium. On the other hand, the stopband is used to suppress the surface waves, leakage and spurious transmission. Tunable bandgap and bandpass performance are desirable in many applications. Semiconductor varactor diodes have been considered in tunable EBGs. Although semiconductor varactors offer integration possibilities, EBG structures based on such varactors suffer from high losses and small tunability at high microwave frequencies, where integration is potentially possible due to the small wavelengths and sizes. By incorporating RF MEMS switches and the EBG filters, a new paradigm has been opened for the development of state of the art tunable filters. These tunable filters are miniaturized, exhibit high Q, wider rejection level, low insertion loss and able to generate tunable bandpass and bandstop or both at the same frequency.

### 1.2 Objective

The main objective of this PhD project is to develop high performance MEMS switches and switching filter which have low insertion loss, low actuation voltage and high isolation from DC ~ 20 GHz. The MEMS switches are designed on a coplanar waveguide (CPW) transmission line. Different design parameters are investigated to improve and optimize the performance of the CPW transmission line. An electrical model and a mechanical design of the MEMS switches are studied extensively. The electrical

Chapter 1 Introduction

model of RF MEMS capacitive switch is used to find the capacitances at both up-state and down-state. A membrane planarization method on uneven surfaces of sacrificial layer is developed to enhance the isolation of the capacitive shunt switch. The surface contact area between the metal bridge and the dielectric layer is greatly improved after the planarization. Surface micromachining fabrication process compatible to CMOS devices is developed for future integration. CPW configuration and the RF capacitive switches are incorporated to design, fabricate, and test the CPW based EBG bandstop filter and the micromachined tunable filters. The MEMS capacitive switch is designed according to the specification summarized in Table 1-2.

Table 1-2 Specifications of the MEMS capacitive switch.

Parameters	Specifications
Insertion loss	< 0.3 dB at 15 GHz
Up state return loss	> 20 dB at 15 GHz
Down state return loss	< 1 dB at 15 GHz
Isolation	> 10 dB at 15 GHz
Switching voltage	< 50 volts

The research focuses on EBG structures to realize a bandstop filter which shows better insertion loss, wide rejection bandwidth and compact size. A circuit modeling is required so that circuit parameters can be extracted to validate and compare the distributed and lumped designs. The frequency characteristics of the EBG structures are demonstrated by employing different circuit parameters. A tunable bandstop filter is

Chapter 1 Introduction

realized by incorporating electromagnetic bandgap (EBG) structures and the micromachined switches. The propagation characteristic of the periodic micromachined switches is determined by studying the dispersion behavior using a new approach. The MEMS tunable filter is designed according to the specification summarized in Table 1-3.

Table 1-3 Specifications of the MEMS tunable bandstop filter.

Parameters	Specifications
Tuning range	5 % tuning in K band
Ripples	<0.6 dB
20 dB bandwidth	> 7 GHz
In-band insertion loss	< 4 dB
Input VSWR (at 50 ohms)	< 1.5
Number of tunable/switchable bands	> 3

The challenge for the microwave community is to develop MEMS tunable bandpass filters and a reconfigurable filter with low insertion loss, wide tuning range and compact design. It is the objective of the study to focus on the development of a MEMS tunable bandpass filter. A tunable Fabry-Perot (F-P) filter is realized using a defect cavity in the EBG structures. The filter has high Q and compact design. The theoretical aspect of the F-P cavity and the EBG structure are discussed. MEMS bridges are placed in the defect cavity to change the capacitance and the resonant frequency can be tuned. A reconfigurable filter using DC contact micromachined switches is designed. This filter can be switched from bandpass to bandstop at the same frequency. An equivalent circuit

model is derived for the reconfigurable cell structure. Extracted parameters show the characteristics of both bandpass and bandstop filters. The specification of the bandpass filter is summarised in Table 1-4.

Table 1-4 Specifications of the MEMS tunable bandpass filter.

Parameters	Specifications
Tuning range	5 % tuning range around $f_0$ $8 \text{ GHz} < f_0 < 12 \text{ GHz}$
3-dB bandwidth	100 ~ 400 MHz
Q factor	>40
In-band insertion loss	< 5 dB
Stop-band rejection	> 20 dB
Number of switchable bands	> 3

1.3 Major contributions

The major contributions of the thesis are the design, fabrication and experimental testing of two different types of tunable filters realized using micromachined capacitive switches and EBG structures. The main contributions are as follows:

Different parametric analyses are applied to obtain an optimized design for a CPW structure. The CPW structure is fabricated using three different types of materials. Among aluminum, gold and copper, gold is preferred for better insertion loss and reliability. The results of the CPW transmission line shows insertion of less than 0.2 dB at 15 GHz.

## Chapter 1 Introduction

---

A MEMS capacitive switch is designed, simulated and fabricated. An equivalent electrical model and a mechanical design are investigated in detail. A new method of calculating the propagation characteristics of the periodic MEMS bridges is discussed. Switching time and pull down voltage are also calculated. A new planarization method is used to improve the isolation of the capacitive shunt switch. The switch is fabricated using surface micromachining process. The contact area between the bridge and the dielectric layer is remarkably increased by 63%, and the isolation of the switch is improved by 2.2 dB at 15 GHz (29.3 % improvement).

Bandstop filters using unloaded and loaded EBG structure are investigated. New equivalent circuit models for the unloaded and loaded structures are derived using circuit analysis theory. Dispersion diagrams are obtained to analyze the propagation characteristics of the EBG structures. The loaded structures show better performance in terms of insertion loss of less than 2 dB and bandwidth greater than 13 GHz.

A new tunable bandstop filter is realized using the EBG structure with MEMS capacitive bridges. The bridges are loaded on the bandstop filter. These bridges act as variable capacitors when bias voltage is applied to the filter. The tunable filter shows low insertion loss from 0.7 to 2.2 dB and wide tuning range of 8% in K band.

A tunable bandpass is realized using Fabry-Perot EBG structures. A defect cavity is created between periodic structures which behave as a F-P resonator. The dimensions of various parameters are studied. A different phenomena such as variable bandwidth, high Q, and rejection level are observed. F-P EBG filters can provide a quality factor of 70 and good tunability range of 7%.

A novel reconfigurable filter using the EBG structure is designed. An important milestone is achieved because the reconfigurable filter can be switched using DC contact MEMS switches from the bandpass filter to bandstop filter at the same operating frequency. The reconfigurable filter shows low insertion loss of less than 1.7 dB and higher rejection level of greater than 20 dB for both bandpass and bandstop filters.

## 1.4 Organization of the thesis

The thesis consists of six chapters as follows:

Chapter 1 is an introduction of the thesis which covers the motivation, objective and major contributions. The motivation section emphasis on the specified field which has prompted us to carry out the PhD work. The objective part is focused on the main challenges of the two different types of tunable filters with MEMS switches. Finally the major contributions elucidates the major goal, achievements and research impacts.

Chapter 2 presents a comprehensive literature survey on different types of the micromachined switches and its application. The literature review on the micromachined tunable bandpass and the EBG bandstop filters is presented in the second section.

Chapter 3 investigates the basic coplanar waveguide structure and the MEMS capacitive switch. Different parameters of the CPW structures are designed and optimized. The electrical and mechanical designs of the MEMS capacitive switch are also investigated. The switch is fabricated using surface micromachining process and its measurement results are discussed.

Chapter 4 focuses on the design and fabrication of tunable bandstop filter using unloaded and loaded EBG structures. The frequency characteristics of the unit cells are studied. The dispersion diagram is derived to analyze the propagation characteristics. The



## ***Chapter 1 Introduction***

---

micromachined capacitive bridges are loaded on the EBG bandstop filter to tune the bandstop filter. The simulation and the measurement results are also discussed and analyzed.

In Chapter 5 Fabry-Perot tunable bandpass filter is designed using the EBG structure with the defect cavity. It shows a narrow bandwidth with good tunability. A new type of reconfigurable filter is realized which can be switched from the bandpass to bandstop using the DC contact MEMS switches. The circuit model, EM simulation and the measurement results are compared and discussed.

Finally, the conclusions and recommendations for future research are given in Chapter 6.

## CHAPTER 2

### LITERATURE SURVEY

#### 2.1 RF MEMS switch and switching circuits

Microelectromechanical systems (MEMS) represent a very large family of devices which can be considered to result from the integration of mechanical elements, sensors, actuators, and electronics on a common silicon substrate through the application of various microfabrication technologies [1-3]. While the electronic components are fabricated using integrated circuit (IC) process (e.g., CMOS, bipolar, or BICMOS processes), while the micromechanical components are fabricated using compatible "micromachining" processes that selectively etch away parts of the silicon wafer or add new structural layers to form the mechanical and electromechanical devices [4-7]. MEMS promises to revolutionize nearly every product category by bringing together silicon-based microelectronics with micromachining technology, making possible the realization **Systems-on-a-Chip**. MEMS technology has made possible the design and fabrication of control devices suitable for switching microwave signals. RF MEMS switches for low-frequency applications were demonstrated in the early 1980s but remained a laboratory curiosity for a long time. In 1990s, the first MEMS switch was specially designed for microwave applications [28]. RF MEMS components that are currently under development in laboratories around the world include switches, voltage tuned capacitors, high quality factor micromachined inductors, and MEMS resonators and filters.

### 2.1.1 RF MEMS switches

The advent of the bulk and surface micromachining technologies during 1970's enabled the emergence of MEMS. A typical RF MEMS switch consists of a thin metal cantilever, an air bridge, or a diaphragm electrically configured in series or parallel with an RF transmission line and designed to open the line or shunt it to ground upon actuation of the electronic signal [29-36]. Such switches display excellent RF characteristics. The advantage of MEMS switches over the other solid state counterparts, such as FETs and p-i-n diodes is their extremely low series resistance and low drive power requirements. In addition, since MEMS switches do not contain a semiconductor junction, they exhibit low intermodulation distortions and can be fabricated on almost any substrate. The disadvantages of the RF MEMS switch are low switching speed, high actuation voltage, and hot switching in high RF power applications. These disadvantages may be tolerated in many applications such as low loss high isolation telecommunications switches and radars with relatively low scanning rates.

The RF MEMS switch consists of two distinct parts of actuation; a mechanical section and an electrical section. The forces required for the mechanical movement can be obtained using electrostatic, magnetostatic, piezoelectric, or thermal designs. The switches can also move vertically or laterally, depending on their layout. To date electrostatic-type thermal switches and magnetostatic switches have been demonstrated at 0.1-100 GHz with high reliability (100 million to 60 billion cycles) and wafer scale manufacturing techniques. Electrostatic actuation is the most prevalent technique in use today due to its virtually zero power consumption, small electrode size, thin layers used,

relatively short switching time, 50-20  $\mu N$  of achievable contact forces, and the possibility of biasing the switch using high resistance bias lines. Table 2-1 summarizes the different configuration of the MEMS switches.

Table 2-1 Different configurations of MEMS switches.

Type of actuations	Voltage (V)	Current (mA)	Power (mW)	Size	Switching time ( $\mu s$ )	Contact force ( $\mu N$ )
Electrostatic	20-80	0	0	Small	1-200	50-1000
Thermal	3-5	5-100	0-200	Large	300-10000	500-4000
Magnetostatic	3-5	20-150	0-100	Medium	300-1000	50-200
Piezoelectric	3-20	0	0	Medium	50-500	50-200

There are two basic types of switches used in RF to millimeter wave circuit design: the series metal-to-metal contact switches [37-40] and the shunt capacitive switches [41-44]. The ideal series switch results in an open circuit in the transmission line when no bias voltage is applied (up-state position), and it results in a short-circuit in the transmission line when a bias voltage is applied (down-state position). The ideal series switches have infinite isolation in the up-state position and have zero insertion loss in the down-state position. The MEMS series switches are used extensively for 0.1 GHz to 40 GHz applications [45-46]. They offer high isolation of -50 dB to -60 dB at 1 GHz. In the down-state position, they result in very low insertion loss of 0.1 to 0.2 dB at 0.1 GHz to 40 GHz. The shunt switch is placed in shunt between the transmission line and the ground. A dielectric layer is used to DC isolate the switch from the CPW centre

---

*Chapter 2 Literature Survey*

---

conductor. The ideal shunt switch results in zero insertion loss when no bias voltage is applied (up-state position) and infinite isolation when a bias voltage is applied (down-state position). The shunt capacitive switches are more suitable for higher frequencies (5-100 GHz). In the up-state position, it has low insertion loss of typically 0.04 dB to 0.1 dB at 5 GHz - 50 GHz. In the down-state position, the isolation is more than 20 dB at 10 GHz - 50 GHz [36-39].

RF MEMS devices are usually fabricated using low temperature processes and are therefore compatible with post-CMOS, SiGe, or GaAs integration. In fact, most of the MEMS switches and filters are fabricated using surface micromachined processes [38-39]. Surface micromachining is a repetitive sequence of depositing thin films on a wafer and patterning them using photolithography and wet etching. In order to create moving, functioning machines, these layers are alternating thin films of a structural material (e.g. polysilicon) and a sacrificial material (typically silicon dioxide). The structural material forms the mechanical elements, and the sacrificial material creates the gaps and spaces between the mechanical elements. At the end of the process, the sacrificial material is removed, and the structural elements are free to move.

A large down/up capacitance ratio is always desirable for the capacitive switch. For instance, a ratio larger than 20 is necessary for high isolation in the down-state. This can be achieved by (a) using dielectric material with high relative dielectric constant, such as strontium titanate oxide (STO) with a relative dielectric constant ranging between 30 and 120 [29]; or (b) improving the contact condition between the metal bridge and the dielectric layer.

The flatness of the bridge and roughness of the dielectric layer are two important factors that affect the contact between the metal bridge and the dielectric layer. A flat metal bridge is one of the desired properties in the design and development of RF MEMS capacitive switches as it increases the contact area between the bridge and the dielectric layer when the bridge is pulled down [3]. As a result, in obtaining a flat metal bridge, a planar and smooth surface of the sacrificial layer plays a critical role. A planar and smooth surface for the sacrificial layer is desirable because the bridge is deposited on the sacrificial layer directly and has a similar surface profile as the sacrificial layer. However, in most RF MEMS devices fabricated using surface micromachining processes, the initial flat wafer surface may develop topography of significant step heights. While topographical features may be essential in creating the desired structure, they also interrupt the process flow as no subsequent photolithographic patterning is possible [47]. Chemo-Mechanical Polishing (CMP) process is one of the most commonly used methods in dealing with the surface non-planarity for any device including MEMS switches [48]. Unfortunately, this method remains relatively costly and less viable. In addition, the CMP process is a Cu/SiO<sub>2</sub> back-end process and its usage is only restricted to polish Cu and SiO<sub>2</sub>. As a result of these shortcomings, CMP is less desirable in solving the problem of surface non-planarity in the fabrication of RF MEMS switches. The following subsection will discuss the applications of the MEMS switches.

### **2.1.2 RF MEMS switching and reconfigurable circuits**

The goal of many commercial and military systems is the ability to easily reconfigure or switch the frequency of operation, the output power, and the input impedance of the

system. Changing the frequency of operation means the resonant frequency must be reconfigured, together with the bandpass filter central frequency, the local oscillator frequency, and the matching networks for the low noise amplifiers and the power amplifiers. In satellite systems, the switching networks are used for coaxial switches, while in base station systems, they are implemented using PIN diodes except after the power amplifiers. PIN diode switches are less expensive compared to coaxial switches, but require input and output amplifiers to compensate for the loss introduced by the switching networks. Coaxial switches result in outstanding isolation, insertion loss and can handle high power, but they are heavy, bulky and very expensive. RF MEMS switches can easily meet the isolation requirement of  $N \times N$  switching matrices with slightly higher insertion loss. However, it is much smaller and lighter system which is essential for satellite communications [3].

In certain cases, the frequency of operation remains fixed but the power amplifier output impedance changes with the time and one must retune the output matching network to result in the highest system efficiency. In many portable applications, the antenna input impedance is strongly dependent on the position of the portable device, and low loss reconfigurable matching network at the input of the antenna would result in a substantial performance improvement. Reconfigurable MEMS circuits can also be used to generate a large range of impedance loci which are necessary for transistor and diode characterization (gain, noise, conversion loss, etc.). Moreover, the RF MEMS devices generate low intermodulation products which are essential if the reconfigurable circuit is before the low noise amplifier / mixer chain.

The RF MEMS devices may also allow the development of low power systems based

on tunable antennas, low noise tunable oscillators, tunable filters and tunable matching networks. The ultimate goal is to integrate the whole front end system on a chip. The main bottleneck is represented not by the inductors or switches but by the low loss (high Q) filters, diplexers and crystal reference. The filters are currently being addressed using Film Bulk Acoustic Resonator (FBAR) technology and MEMS resonators. Using the RF MEMS devices (switches, varactors, and high Q planar inductors) it is possible to eliminate the off-chip inductor in the oscillator circuit or integrate the tunable filter on a silicon chip.

## **2.2 Micromachined tunable filters**

### **2.2.1 Basic concept of the filters**

The emergence of wireless applications, as perhaps the most financially significant market, has fully exploited the advantages of RF frequency utilization. The role of filters is very important in many RF/microwave applications. The demand for increasingly higher rates of data transmission requires the development of a mature technology where bandwidth capacity can be managed by state of the art RF filters. They are primarily used to separate or combine different frequencies [12-14]. As the electromagnetic spectrum is limited and has to be shared, the filters are used to select or confine the RF/microwave signals within assigned spectral limits. The challenge of the RF/microwave filters is to meet the ever more stringent requirements of higher performance, smaller size, lighter weight and lower cost. Depending on the requirements and specifications, the RF/microwave filters may be designed as lumped elements or distributed elements circuits. They may be realized in various transmission line structures such as waveguide, coaxial line and microstrip. Normally, the microwave filter is a two-port, reciprocal, and



passive device, which attenuates heavily unwanted signal frequencies while permits for the transmission of wanted frequencies. Important performance specifications to consider when searching for RF filters include resonant frequency,  $f_r$ , bandwidth, ripple, insertion loss, and voltage standing wave ratio (VSWR) [14]:

- For bandpass and bandstop filters, the  $f_r$  refers to the center frequency and the specified frequency for a low pass and a high pass filter is known as cut-off or cut-on frequency, respectively.
- Bandwidth is the range of frequency the RF filters passes with minimal attenuation or in the case of a band reject filter, maximum attenuation.
- Ripple is the peak-to-peak variation of the passband response, which is expressed in decibels and is a function of the impedance match of the device in the system.
- Insertion loss is the total RF power transmission loss resulting from the insertion of a device in a transmission line. It is defined as the ratio of signal power at the output to the input signal power at the input of the inserted device. When there are impedance mismatches in a system, some energy transmitted through is reflected back to the source. Different amounts of energy are reflected back depending on the frequency of the signal.
- VSWR is a unitless ratio ranging from 1 to infinity, expressing the amount of reflected energy. A value of one indicates that all the energy passes through, while any other value indicates that a portion of the energy is reflected.

The RF filters are also classified according to the range of frequencies which are allowed to pass, which include low pass, high pass, band pass and band stop filters.

A low pass filter is a circuit offering easy passage to low-frequency signals and

difficult passage to high-frequency signals. All low-pass filters are rated at a certain cutoff frequency ( $f_{co}$ ). That is, the frequency above which the output voltage falls below 70.7% of the input voltage. The examples of low pass filters are the stepped-impedance, open stub and semilumped element filters, respectively.

The high pass filter performs the opposite operation rejecting all frequencies below  $f_{co}$  and passing the frequencies above it. Practical examples are the optimum distributed highpass and quasilumped high pass filters, respectively.

Bandpass filters are active or passive circuits which allow signals within the desired frequency band to pass through, but impede signals outside this passband from getting through. Practical examples are end coupled, parallel coupled, interdigital and combline filters, respectively.

Bandstop filter is a tuned circuit that does not pass a specified band of frequencies, also known as a notch filter. Practical examples are open circuited stub bandstop, and electromagnetic bandgap structures filters, respectively.

### 2.2.2 MEMS tunable filters

Tunable filters are very important for RF communications and finding growing interest in many civil and military telecommunication/radar equipments such as electronic warfare, software programmable RF front-end and digital receivers. Some communication systems use the tunable filters for switching frequency bands in multiband systems.

Traditional microwave tunable filters can be classified into three basic types depending on the basic principle of their tunability: mechanically, magnetically, and

Chapter 2 Literature Survey

electronically tunable filters [12-14]. None of these filters, however, can satisfy the requirements of miniaturization and mass-production. The filters must be custom machined, carefully assembled, tuned, and calibrated. For high frequencies, where the resonators are very small, neither the conventional machining nor the mechanical tuning is suitable. Different configurations of MEMS switches can be applied for the tunable filter applications. Research is now focused on developing miniaturized high performance MEMS based- tunable filters.

Table 2-2 Literature survey of RF MEMS tunable filters.

Different types of MEMS tunable filter	Tuning range %	3 dB bandwidth %	In band loss (dB)	Stop band rejection (dB)	Input VSWR (dB)	No of tunable bands
CPW micromachined filter [54]	2.3 %	4.7 %	4.9	>30	>35	2
DMTL tunable filters [55]	3.8 %	12 %	3.6	>35	> 35	3
Interdigital filter [56]	12.8 %	14 %	3.5	>30	>10	2
Miniature and tunable filter using MEMS [57]	17 %	20 %	3.9	>40	>25	6
Widely tunable filter [58]	35 %	4.0 %	3.5	>20	>30	5
RF MEMS tunable filter [59]	11%	19%	3-5	>30	>15	6
Varactor tuned filter [18]	60 %	16 %	3.0	>40	>10	5

RF MEMS switches are extremely linear devices since they do not contain a semiconductor junction and, therefore, an exponential current versus voltage relationship does not exist. MEMS switches and filters can be designed to be mechanically stiff and can tolerate large RF voltages swings without generating levels of intermodulation

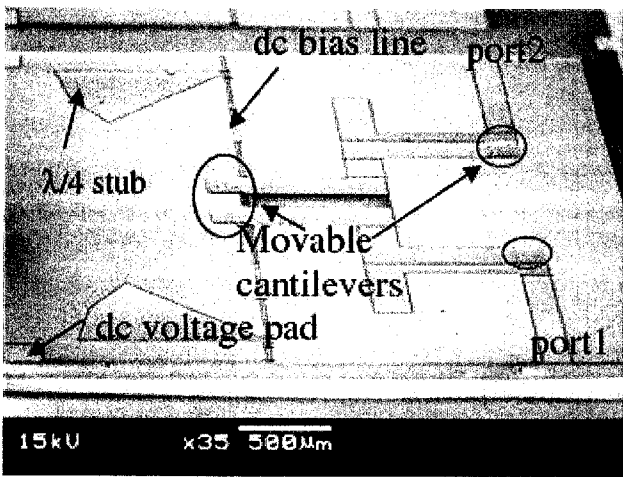


Fig. 2-1 Tunable millimeter wave filter using micromachined capacitor [54]

products. They are simply near ideal elements for tunable filters and matching networks [49-53]. Based on these advantages of MEMS switches and micromachined tunable filters, the summary of literature survey on micromachined tunable filter is shown in Table 2-2.

Initially, the micromachined tunable filters were implemented using lumped elements and resonators as shown in Fig. 2-1 [54]. The frequency tunability was achieved by changing the gap between the coplanar waveguide ground plane and a movable cantilever beam, resulting in a tuning range of 3%.

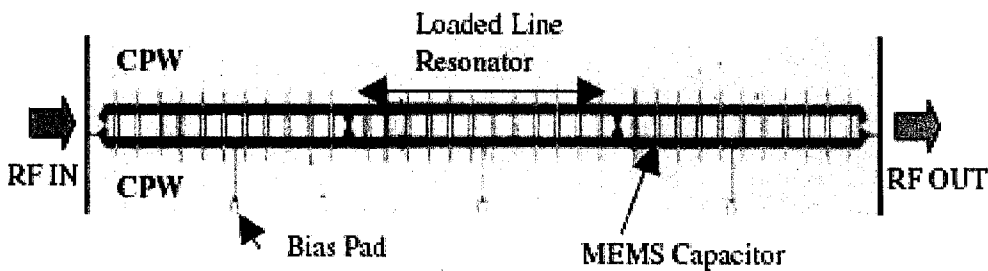


Fig. 2-2 Distributed MEMS transmission line for tunable filters [55]

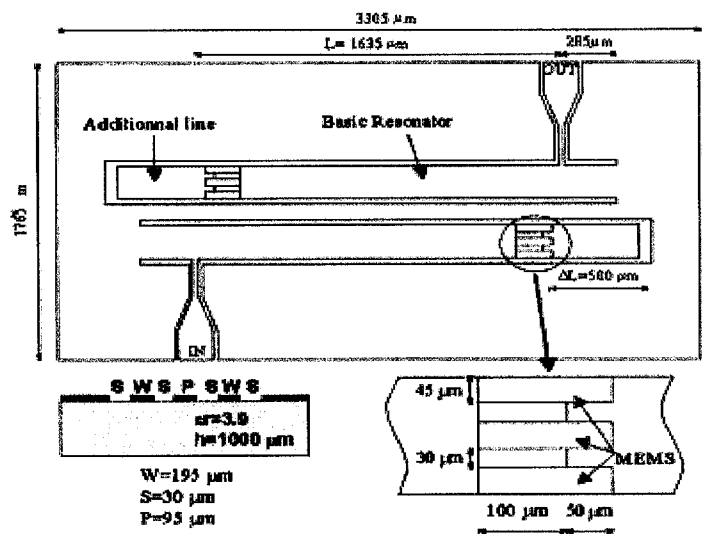


Fig. 2-3 MEMS switchable interdigital coplanar filter [56]

The distributed MEMS transmission line technique has been used to implement the millimeter wave tunable filters by electronically varying the loading capacitance of the switches as shown in Fig. 2-2 [55]. The loading capacitance at zero bias is 12-13 fF for each micromachining bridge, and is achieved using a 30  $\mu\text{m}$  wide of the bridge suspended 3  $\mu\text{m}$  above the centre conductor. The filter is fabricated on glass substrate, and has a tuning range of 4%, insertion loss of 3.6 dB and quality factor of 60.

The switchable interdigital filter uses a different concept of tuning the frequency by changing the length of the resonator. It is a two pole filter based on a shortened  $\lambda/4$  CPW resonator on a quartz substrate. Three inline MEMS gold cantilever capacitive series switches with  $C_r = 20$  are used in order to get a low impedance connection between resonator and the extra section. The centre frequency can be switched from 18.5 GHz to 21.05 GHz with return loss less than 15 dB and insertion loss of 3.5 dB as shown in Fig. 2-3 [56].

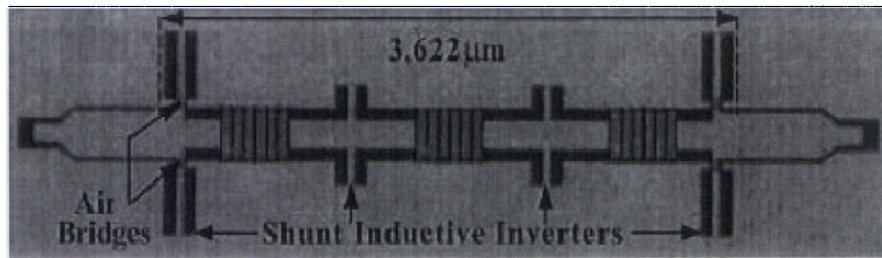


Fig. 2-4 Miniature and tunable filters using MEMS switches [57]

Fig. 2-4 shows MEMS slow wave resonators based on CPW lines which are inductively coupled to form a miniature three pole filters and show excellent frequency response in the passband and rejection band. The centre frequency tunes from 18.6 GHz to 21.44 GHz with the pass band covering 17.9 GHz ~ 22.23 GHz. The fractional bandwidth is 7.5% over the whole tuning range. The mid band insertion loss was measured at 3.84 dB ~ 4.15 dB [57].

A tunable filter capacitively coupled two pole Chebyshev filter was developed for 40 MHz to 60 MHz applications [60], which has a 10 % fractional bandwidth and a characteristic impedance of 1390 ohms. The input and output ports were therefore matched to 50 ohms with tapped inductors. The measured insertion loss is less than 1 dB and the return loss is better than 15 dB over the tuning range. A two pole 26.8 GHz filter was also built on a glass substrate and it was based on a lumped element design with a 1 dB bandwidth of 3% [54]. The calculated inductance of each spiral inductor is 0.52 nH and the mutual inductance is 0.3 nH. The measured filter produces a tuning range of 0.6 GHz for a 50 V varactor bias voltage, along with an insertion loss of 4.9 dB.

The two pole tunable filter using MEMS switched capacitors at 110 MHz – 160 MHz was developed using MEMS interdigital varactors at 240-360 MHz. The filter uses two 8

bit capacitors with switched capacitor values of 0.8/1.5/2.4/3.8/7.5/12/16/22 pF for precise frequency control. Measurement results indicate an insertion loss of 5 dB over the tuning range that produces a measured output intermodulation product of -71.5 dBm for an output power of 20 dBm at 112 MHz, where all the switches are in the down-state position.

Recently, wide band tunable filters based on the distributed MEMS transmission line (DMTL) concept have also been proposed, which have a constant bandwidth in the tuning range because the capacitive gap varies with the MEMS switches [59]. They have achieved the largest tuning range of 35 %.

### **2.3 Electromagnetic Bandgap (EBG) Structures and filters**

Periodic structures have recently attracted much attention in the microwave and millimeter-wave community due to their filtering properties or inhibition of signal propagation in certain directions. Electromagnetic crystal structures are invented for microwave as well as for optical wavelengths [19-22]. They exhibit bandpass and bandstop characteristics at microwave frequencies. These structures have been usually referred to as electromagnetic bandgap structures (EBGs) or electromagnetic crystals.

The term of EBG may also be used in relatively loose fashion when it is applied to some structures such as one dimensional (1D) periodic structures and defected microstrip ground structures. However, applying the EBG concept allows one to extend the horizon of imagination greatly when conceiving novel structures to control the behavior of electromagnetic waves, such as guided waves, surface waves or radiation waves. According to the locations of the EBG holes, the EBG structures can be embedded in the

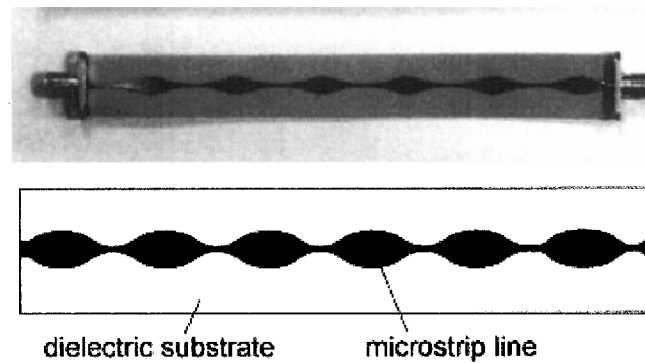


Fig. 2-5 EBG bandstop filter with sinusoidal variation of characteristics impedance [63]

dielectric substrate or etched on the metal layer, which can suppress the surface waves and give a better radiation pattern and higher antenna efficiency [61]. The EBG structures realized on metal layer are useful for constructing filters including bandstop filters as shown in Fig. 2-5 and Fig. 2-6 [62-64], lowpass filter [65-67], phase shifters as shown in Fig. 2-7 [25], and antennas [26]. Examples of EBG structures patterned on metal layer are the microstrip transmission line with EBG etched holes on the ground plane as shown in Fig. 2-8 [27] or on the signal line [68, 69].

The achievement of broad band harmonics tuning is typically cumbersome for active integrated antenna amplifiers and for power amplifiers in general. The harmonics filtering is required which necessitates larger transmission stopbands. These types of larger stopbands can be achieved with the use of EBG ground plane. The implementation of the so-called EBG ground plane in power amplifiers results in intrinsic, broadband harmonics with out the need of any stub or filtering element. In the design of the broadband power amplifier the EBG periodic structures are integrated with a slot antenna where the periodic structures are used to tune in the second harmonic. The measured power added efficiency (PAE) is better than 50% over an 8% bandwidth (3.7 to 4 GHz) with second



harmonics tuning only. In the combined approach, where the microstrip patch with shorting pins is used to tune the second harmonic and the periodic structure is used to tune out the third for a class AB power amplifier, then PAE was 61% with output power of 21.9 dBm. Tuning of second and third harmonics provides an efficient power amplifier [70]. A comparison is made between an amplifier assisted with EBG microstrip line and a reference amplifier with a standard 50  $\Omega$  microstrip line. The EBG assisted amplifier provides 10% improvement of PAE and 13 dB increase in output power. The EBG assisted structure also provides 37 dB additional suppression for the second harmonics and at least 30 dB for the third harmonics. The implementation of the entire system using EBG structure results in a compact and high performance power amplifier for a wide range of wireless applications [71].

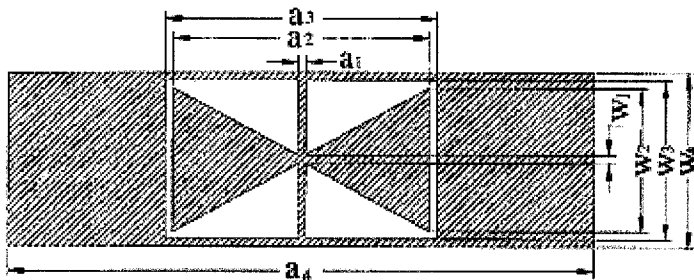


Fig. 2-6 1-D electromagnetic bandgap microstrip transmission line [64]

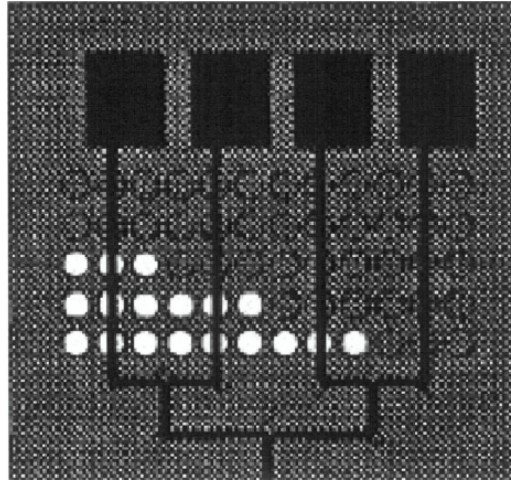


Fig. 2-7 A beam-steerer using reconfigurable PBG ground plane [25]

Another study is the CPW with etched holes on the ground plane [72] or on both the ground and signal lines [73]. CPW offers greater design flexibility and requires single metal layer as compared to the microstrip structures. The CPW structures are more attractive because of the ease of characterization and fabrication, not forgetting its promising applications in microwave integrated circuits (MICs), monolithic microwave integrated circuits (MMICs), and microelectromechanical systems (MEMS) devices. In a CPW, an extra ground plane is normally used in its backside to increase mechanical strength to realize mixed CPW microstrip circuits or provide a heat sink [74]. This type of conductor backed CPW (CB-CPW) can excite a parallel plate mode which deteriorates the performance of CPW. Using posts to short the unwanted plate mode or using a multi-layer substrate to shift the dispersion curve of the parallel plate mode are different approaches to solve this problem. The uniplanar-compact EBG (UC-EBG) is a promising technique to solve this leakage because of its deep stopband characteristics. This can be

easily etched in the top ground plane of a CB-CPW circuit without using extra masks or

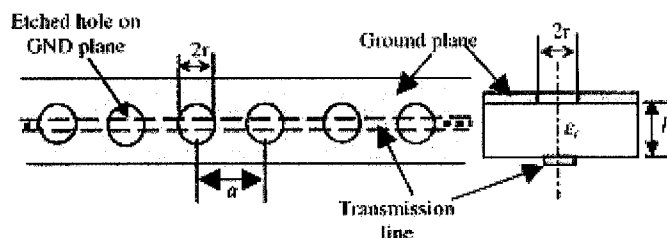


Fig. 2-8 Non-uniform electromagnetic bandgap microstrip low pass filters [27]

via holes. The result shows that for the conventional CB-CPW the significant leakage is observed at all frequencies. This type of CB-CPW may find its potential application in CPW-fed slot antenna [75-81]. The transverse electromagnetic (TEM) waveguide is very promising technique as feeding structure for quasi-optical power combining amplifiers. The use of a waveguide in power combining is very popular as the diffraction loss can be avoided in this case [82]. Though dielectric loaded or oversized waveguides are often used in combined amplifiers arrays for achieving uniform aperture field distribution [83], as yet they are not suitable at small size compared to the conventional empty waveguide. The UC-EBG structure can be used to build a TEM waveguide with a uniform field distribution. Replacing two side walls of a rectangular waveguide with a UC-EBG structure constitutes TEM waveguide providing PMC surface at the wider stopband. This structure can be fabricated on a thin substrate using a standard etching technique. The EBG waveguide [84] produces a fairly uniform field distribution and the phase velocity is close to the speed of light that ensures a TEM propagation. This type of waveguide also finds its application to TEM cells in EMC measurements.

The UC-EBG ground plane had been used to replace the conventional ground plane in the conductor-backed CPW (CBCPW) structure [72], since the EBG structures are distributed across the ground plane of the CPW for mechanical strength reasons. CPW EBG structures with rectangular aperture patterns etched on the ground plane and located adjacent to the gap between the signal and ground had been reported [85-86]. The research is now focusing on developing bandpass filters using EBG structures. Recently, bandpass filters using EBG are realized in CPW, microstrip and stripline configurations [87] to obtain a high Q filter. The defect mode concept of the EBG structure generates a high Q image guide resonator, which is used in oscillator to generate low noise oscillations [88]. Generally, EBG structure generates stopband function when  $\beta a = \pi$ , where  $\beta$  is the propagation constant and  $a$  is the period of the EBG structures. On the other hand, a sharp, high Q defect mode is obtained when the cavity is formed in the middle of the EBG lattice with a length  $l$ , illustrated by FDTD simulations [88]. This image guide is excited by the modulated Gaussian pulse at a location outside the EBG grooves. The peak transmission frequency is 8.255 GHz, which is determined by using the Fourier spectrum of the field inside the cavity. The measured transmission coefficient  $S_{21}$ , indicates that a single, high Q cavity mode exists in 0 ~ 20 GHz frequency range. The measured peak frequency is 8.276 GHz, which is in agreement with the FDTD simulation results (0.25 % error). The measured result  $Q_u$  is 697, when the RT-Duroid 6010 ( $\tan\delta = 0.002$ ) is used.

EBG engineered structures may have different forms such as bumpy or corrugated surfaces, metal pads or high impedances surface and planar EBG structures. Normally, the ground plane is perturbed by EBG structures with different shape and different lattice

structures. The shape may be uniform or non-uniform circular, square, rectangular, triangular patterned and the structures are named on the basis of the grid arrangement such as square, rectangular, triangular and honey-comb etc. Different shapes and sizes of EBG structures provide different S-parameters performance. Due to their unique properties, the EBG structures can be used to design microwave components and devices for different applications such as filters [89-100], mixers, antennas [101-112], oscillator, power amplifiers [70-71], and phase array etc.

Conventional parallel coupled bandpass filters need extra filters to suppress the spurious transmission that results in the increase of the insertion loss [97-100]. It is reported that the use of extra filters can be avoided by applying the EBG structures to obtain a compact microstrip bandpass filter with intrinsic spurious rejection. The well-matched microstrip on the UC-EBG ground plane is suitable as a low-loss transmission line. Spurious passbands at higher frequencies can be suppressed using the EBG structures because they provide a wide and deep stopband. The physical length of the filter circuit is reduced due to the slow wave effect of the UC-EBG structure. At 12 GHz and 17 GHz, the transmission co-efficients of a conventional bandpass filter are -10 dB and -5 dB. On the other hand, the UC-EBG assisted filter provides the spurious suppression of 30-40 dB. EBG structures fabricated on the silicon substrate have also been investigated [113]. A conventional open-ended tunable bandstop filter using piezoelectric transducers has been reported [114]. However, this design has bulky structure. Another type of tunable EBG bandstop filter using varactor diodes has also been reported [115]. Unfortunately, this design yields relatively high insertion loss and ripples in the passband region due to the properties of the varactor diodes.

## *Chapter 2 Literature Survey*

---

Most researchers have focused mainly on the possibility of developing a stopband in EBG structures. However, only a few studies have been reported on the modeling, performance and tuning of the bandstop filters. Similarly, a micromachined reconfigurable filter, which can be switched from bandpass filter to bandstop filter, has not been reported yet.

In chapters 4 and chapter 5, the PhD research will be focused on EBG structures used with the MEMS switches to design tunable bandstop, tunable bandpass and reconfigurable filters.

## **CHAPTER 3**

# **MICROMACHINED TRANSMISSION LINE AND CAPACITIVE SWITCHES**

In this chapter, the CPW transmission line is designed, fabricated and experimented. Different design parameters are optimized to improve the performance of the CPW transmission line. Mathematical expressions are derived for the calculation of the effective dielectric constant and characteristic impedance. The effect of the conductor loss and the dielectric loss from high resistivity (HR) silicon and low resistivity (LR) silicon on the performance of the CPW transmission line are analyzed. The CPW transmission line is fabricated using the MEMS surface micromachining process.

MEMS shunt capacitive switches are also designed, simulated and fabricated. An electrical modeling and a mechanical design of such a MEMS switch are studied extensively. The up-state and the down-state capacitances of the switch are calculated using this electrical model. A new planarization fabrication process is developed to enhance the isolation of the capacitive shunt switch. The surface contact area between the metal bridge and the dielectric layer of the switch can be greatly improved after the surface planarization. Finally, the measurement results and the effects of the surface planarization on isolation are discussed.

### 3.1 Silicon based CPW transmission line

A coplanar waveguide (CPW) consists of a center strip conductor with semi-infinite ground planes on either side as shown in Fig. 3-1. The dimensions of the center strip, the gap, the thickness and permittivity of the dielectric substrate are determined by the effective dielectric constant  $\epsilon_{eff}$  the characteristic impedance  $Z_0$  and the attenuation,  $\alpha$  of the line. This structure supports a quasi-TEM mode of propagation. The CPW offers several advantages over the conventional microstrip line [116-125]:

- It simplifies fabrication
- Easy shunt as well as series surface mounting of active and passive devices
- It eliminates the need for wraparound and via holes, and
- It reduces radiation loss

#### 3.1.1 Characteristic impedance and effective dielectric constant

The cross-sectional view of CPW is shown in Fig. 3.1. The CPW center strip conductor width  $S$  is  $2a$  and the distance between the two ground planes is  $2b$ . Consequently, the slot width  $W$  is equal to  $b - a$ . The CPW conductors and the dielectric substrates are assumed to have perfect conductivity and relative permittivity, respectively. Hence, the structure is considered to be low loss and the dielectric substrate materials are considered to be isotropic.



## Chapter 3 Micromachined Transmission Line and Capacitive Switches

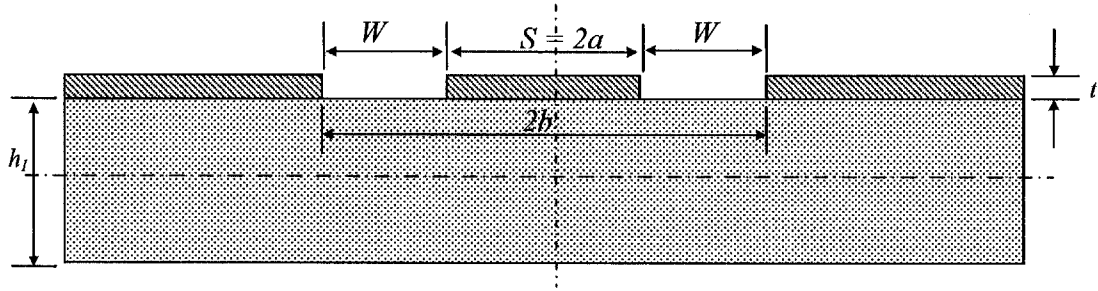


Fig. 3-1 Schematic of the coplanar waveguide (CPW) structure.

In this section, the mathematical derivations of  $\epsilon_{eff}$  and  $Z_0$  using the conformal mapping techniques are presented. Two assumptions are made. First, the conductor thickness  $t$  is zero, and second, the magnetic walls are present along all the dielectric boundaries including the CPW slots. The CPW is then divided into several partial regions and the electric field is considered to exist only in the partial region. In this manner, the capacitance of each partial region is determined separately. The total capacitance is the sum of the partial capacitances [126]. The total capacitance  $C_{CPW}$  can be expressed as [127],

$$C_{CPW} = C_1 + C_{air} \quad (3-1)$$

where

$$C_1 = 2\epsilon_0 (\epsilon_{r1} - 1) \frac{K(k_1)}{K(k_1')} \quad (3-2a)$$

where  $K$  is complete elliptic integral of first kind, and the modulus of the elliptic integrals  $K(k_1)$  and  $K(k_1')$  [127] are given by,

---

**Chapter 3 Micromachined Transmission Line and Capacitive Switches**

---

$$k_1 = \frac{\sinh(\pi S/4h_1)}{\sinh\{\llbracket \pi(S+2W) \rrbracket /4h_1\}} \quad (3-2b)$$

and

$$k_1' = \sqrt{1 - k_1^2} \quad (3-2c)$$

where  $h_1$  is the height of the substrate,  $S$  is the CPW central strip conductor width and

$W$  is the slot width. The capacitance  $C_{air}$  is given by [127],

$$C_{air} = 2\varepsilon_0 \frac{K(k_3)}{K(k_3')} + 2\varepsilon_0 \frac{K(k_4)}{K(k_4')} \quad (3-3a)$$

where,

$$k_3 = \frac{\sinh(\pi S/4h_3)}{\sinh\{\llbracket \pi(S+2W) \rrbracket /4h_3\}} \quad (3-3b)$$

$$k_4 = \frac{\sinh(\pi S/4h_4)}{\sinh\{\llbracket \pi(S+2W) \rrbracket /4h_4\}} \quad (3-3c)$$

$$k_3' = \sqrt{1 - k_3^2} \quad (3-3d)$$

$$k_4' = \sqrt{1 - k_4^2} \quad (3-3e)$$

Substituting  $h_3 = h_4 = \infty$  into Eqs. (3-3a), (3-3b) and (3-3c), we have,

$$C_{air} = 4\varepsilon_0 \frac{K(k_0)}{K(k_0')} \quad (3-4a)$$

where,

$$k_3 = k_4 = k_0 = \frac{S}{S+2W} \quad (3-4b)$$

$$k_1' = k_0' \quad (3-4c)$$

Substituting Eqs (3-2a) and (3-4a) into Eq. (3-1),  $C_{cpw}$  is expressed as,

### Chapter 3 Micromachined Transmission Line and Capacitive Switches

$$C_{CPW} = 2\varepsilon_0(\varepsilon_{r1} - 1) \frac{K(k_1)}{K(k_1')} + 4\varepsilon_0 \frac{K(k_0)}{K(k_0')} \quad (3-5)$$

Under the quasi-static approximation,  $\varepsilon_{eff}$  is defined as [127]:

$$\varepsilon_{eff} = \frac{C_{CPW}}{C_{air}} \quad (3-6)$$

Substituting Eqs. (3-4a) and (3-5) into Eq. (3-6) is expressed as,

$$\varepsilon_{eff} = 1 + \frac{\varepsilon_{r1} - 1}{2} \frac{K(k_1)}{K(k_1')} \frac{K(k_0')}{K(k_0)} \quad (3-7)$$

The characteristics impedance  $Z_0$  is defined as [127],

$$Z_0 = \frac{1}{cC_{air}\sqrt{\varepsilon_{eff}}} \quad (3-8)$$

Substituting Eq. (3-4a) into Eq. (3-8) gives,

$$Z_0 = \frac{1}{4c\varepsilon_0\sqrt{\varepsilon_{eff}}} \frac{K(k_0')}{K(k_0)} \quad (3-9a)$$

where,  $c = 3 \times 10^8$  m/s and  $\varepsilon_0 = 8.854 \times 10^{-12}$  farad/m, so Eq. (3-9a) simplifies as,

$$Z_0 = \frac{30\pi}{\sqrt{\varepsilon_{eff}}} \frac{K(k_0')}{K(k_0)} \quad (3-9b)$$

In Fig. 3-2, the characteristics impedance curve is plotted with different slot and conductor width values. The characteristic impedances for different dielectric substrates are also included. For the same ratio,  $S/(S+W)$  of the slot conductor, the substrate with a lower dielectric constant has a higher characteristic impedance.

Chapter 3 Micromachined Transmission Line and Capacitive Switches

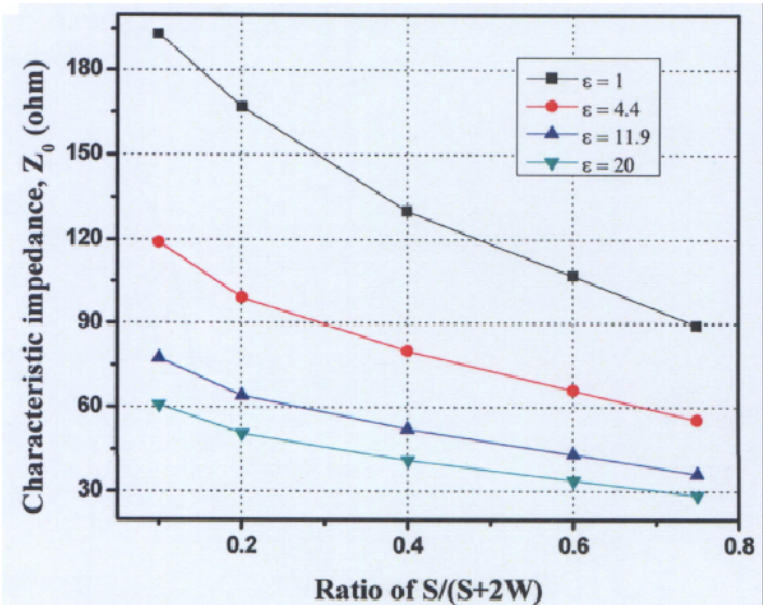


Fig. 3-2 Characteristics impedance of coplanar waveguide versus different dielectric constant of the substrate material.

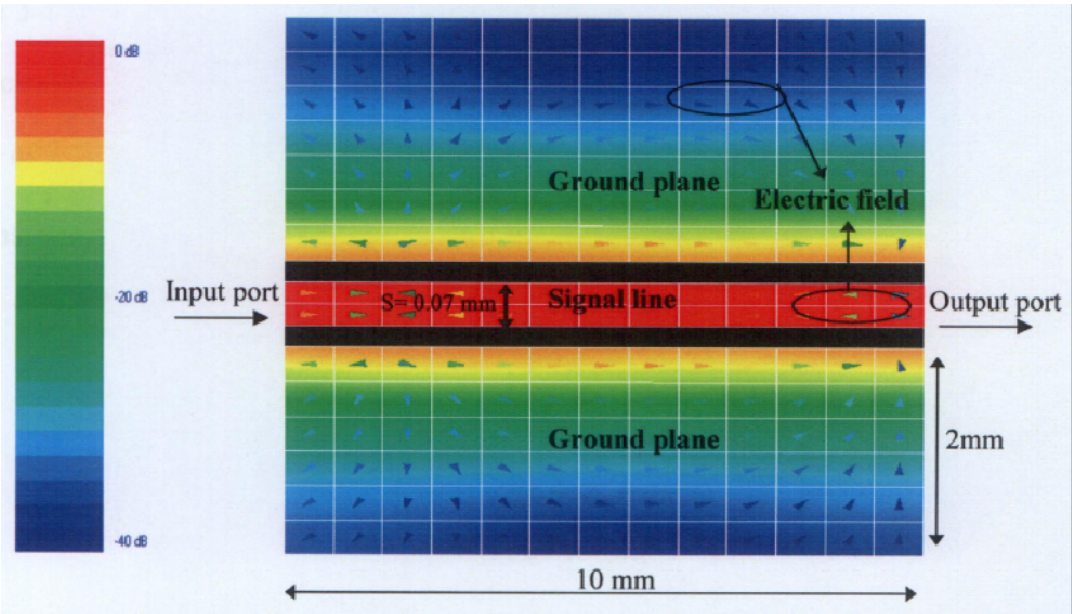


Fig. 3-3 Simulation result shows the top-view for the current distribution in the coplanar waveguide.

### Chapter 3 Micromachined Transmission Line and Capacitive Switches

---

The vector current distribution of the coplanar waveguide is calculated using method of moment software IE-3D as shown in Fig. 3-3. In CPW transmission line the electric field radiates from the centre signal conductor to the two ground conductors and into the substrate i.e. the dominant mode for this kind of transmission line is quasi-transverse electromagnetic (TEM) mode, while the magnetic field lines encloses around only the center signal conductor. The calculated electric current using IE-3D is 250.3 amp/m, which is dominant compared to magnetic current of  $1 \times 10^{-5}$  V/m. This explains the reason for the strong penetration of the E-field from the signal line to ground plane and into the substrate. The low dielectric loss substrate is also to contribute a strong penetration of the E-field and vice versa [13]. In Fig. 3-3, the bar indicates the different colour representation in decibels for different attenuation levels. As noticed, the signal passes with minimum attenuation of 0.1-0.3 dB from input to the output port.

Figure 3-4 shows that for fixed  $(S+2W)$  and aspect ratio  $S/(S+2W)$ , the  $Z_0$  decreases as the thickness of the metal  $t$  increases for silicon substrate. For a fixed aspect ratio  $S/(S+2W)$  of 0.1 and the metal thickness is  $t = 0.5 \mu\text{m}$ , the characteristics impedance is 78.37 ohms. On the other hand, when the metal thickness is  $10 \mu\text{m}$  the characteristic

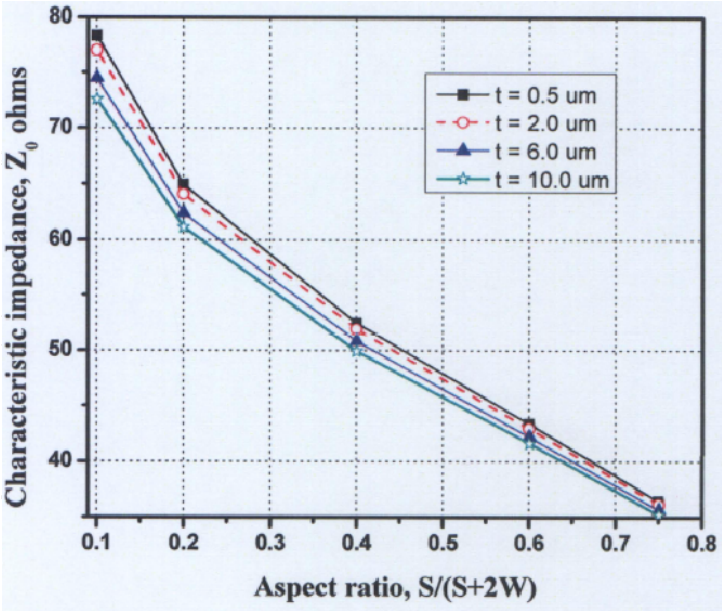


Fig. 3-4 Simulation result of characteristics impedance of CPW with different metal thickness.

Figure 3-4 shows that for fixed  $(S+2W)$  and aspect ratio  $S/(S+2W)$  the  $Z_0$  decreases as the thickness of the metal  $t$  increases for silicon substrate. For a fixed aspect ratio  $S/(S+2W)$  of 0.1 and the metal thickness is  $0.5 \mu m$ , the characteristic impedance is 78.37 ohms. On the other hand, when the metal thickness is  $10 \mu m$  the characteristic impedance is 72.54 ohms, while for a fixed aspect ratio of 0.75, the characteristic impedance is 37.5 ohms for  $10 \mu m$  and 38.4 ohms for  $2 \mu m$  metal thickness, respectively.

3.1.2 Losses of CPW structure

For the CPW structure, two major factors are considered for the transmission line losses. The total CPW attenuation is expressed as the sum of the attenuation due to the

### Chapter 3 Micromachined Transmission Line and Capacitive Switches

---

dielectric losses in the substrate and that due to the conductor losses in the strip and the ground planes.

#### 3.1.2.1 Dielectric loss $\alpha_d$

The dielectric loss is due to the displacement current in the guiding medium of the CPW transmission line. The attenuation constant due to the dielectric loss is expressed as [12],

$$\alpha_d = \frac{\pi}{\lambda_0} \frac{\epsilon_r}{\sqrt{\epsilon_{eff}}} q \tan \delta_e \quad (\text{Nepers/ meter}) \quad (3-10)$$

where  $\lambda_0$  is the free space wavelength in meters,  $\epsilon_r$  is the relative permittivity of the substrate,  $\tan \delta_e$  is the dielectric loss tangent,  $\epsilon_{eff}$  is the effective dielectric constant. The loss tangent  $\tan \delta_e$  remains constant with respect to the frequency for different dielectric materials. However, the dielectric loss  $\alpha_d$  increases linearly with the frequency. The loss tangent is an important factor to be taken into consideration as there are material losses due to bulk conductivity  $\sigma$ . The loss tangent is defined as,

$$\tan \delta_e = \frac{\sigma}{\omega \epsilon_0 \epsilon_{eff}} \quad (3-11)$$

The material with high loss tangent results in a higher dielectric loss. The material or substrate properties are listed in Table 3-1.

Chapter 3 Micromachined Transmission Line and Capacitive Switches

Table 3-1 Properties of the dielectric materials.

Materials	$\epsilon_r$	$\tan \delta_e$
High resistivity (HR) Silicon	11.9	0.025 S×m
Low resistivity (LR) Silicon	11.9	100 S×m
Air	1.0	0.0 S×m

3.1.2.2 Conductor loss  $\alpha_c$

The attenuation constant due to the conductor loss  $\alpha_c$  in the central strip conductor and the ground planes of the CPW is given below. In deriving this expression, the thickness  $t$  of the CPW conductors is assumed to be greater than the skin depth  $\delta$  in the metal. The conductor loss  $\alpha_c$  is defined as [12],

$$\alpha_c = \frac{R_c + R_g}{2Z_0} \tag{3-12}$$

where  $R_c$  is the series resistance in ohms per unit length of the centre conductor given by,

$$R_c = \frac{R_s}{4S(1-k_0^2)K^2(k_0)} \left[ \pi + \ln\left(\frac{4\pi S}{t}\right) - k_0 \ln\left(\frac{1+k_0}{1-k_0}\right) \right] \tag{3-13}$$

$R_g$  is the distributed series resistance in ohms per unit length of the ground planes and is given by,

$$R_g = \frac{k_0 R_s}{4S(1-k_0^2)K^2(k_0)} \left[ \pi + \ln\left(\frac{4\pi(S+2W)}{t}\right) - \frac{1}{k_0} \ln\left(\frac{1+k_0}{1-k_0}\right) \right] \tag{3-14}$$

$R_s$  is the skin effect surface resistance given by,



Chapter 3 Micromachined Transmission Line and Capacitive Switches

$$R_s = \frac{1}{\delta \sigma} \tag{3-15}$$

where  $\sigma$  is the conductivity, and  $\delta$  is the skin depth. Therefore, the total attenuation  $\alpha$  can be expressed as,

$$\alpha = \alpha_c + \alpha_d \tag{3-16}$$

Based on Eq. 3-10, the dielectric loss is linearly proportional with frequency. Fig. 3-5 shows the relationship between the frequency and the attenuation. The attenuation at the frequency of 20 GHz is 0.37 dB/cm.

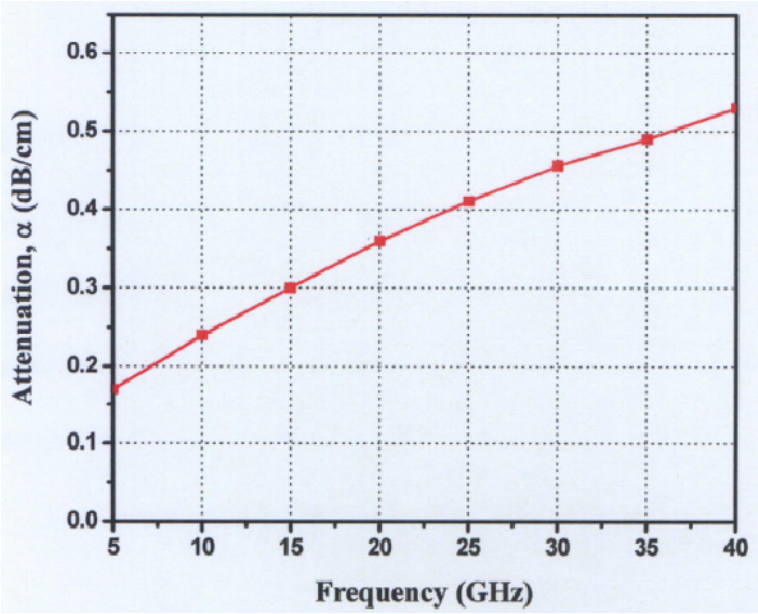


Fig. 3-5 Simulation results of attenuation constant due to conductor loss as a function of frequency of the CPW structure.

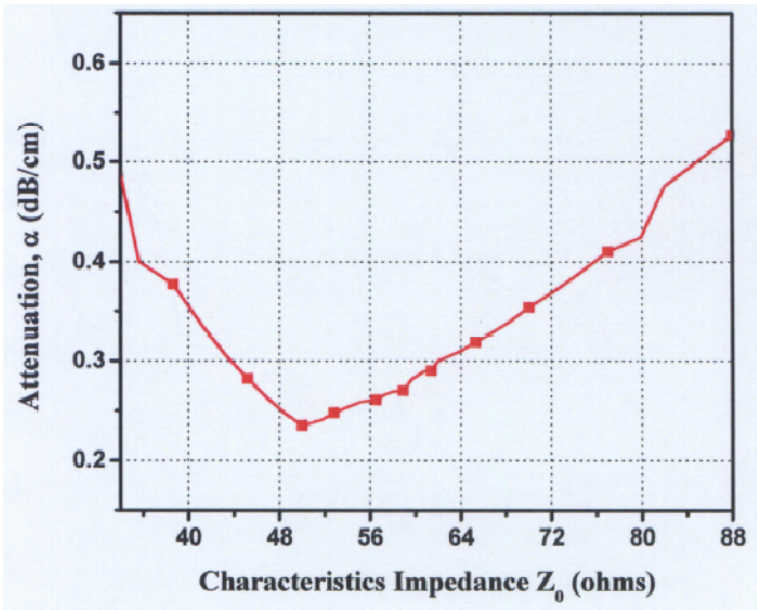


Fig. 3-6 Simulation results of coplanar waveguide attenuation constant versus characteristic impedance for an aspect ratio,  $S/(S+2W)$ .

Figure 3-6 shows the simulation results of the attenuation constant  $\alpha$  and the characteristic impedance  $Z_0$  when the ground plane separation ( $S+2W$ ) is constant. It is noted that the attenuation decreases slowly with the increase in characteristic impedance. Minimum attenuation occurs at the characteristic impedance which is close to 50 ohms. When the characteristic impedance is raised above 50 ohms, the attenuation increases gradually.

3.1.3 Effects of material properties

The material properties have a significant effect on the performance of the CPW structure. They affect both the insertion loss and the RF transmission properties of the structure. Usually the insertion loss of the CPW structure should be made as low as

---

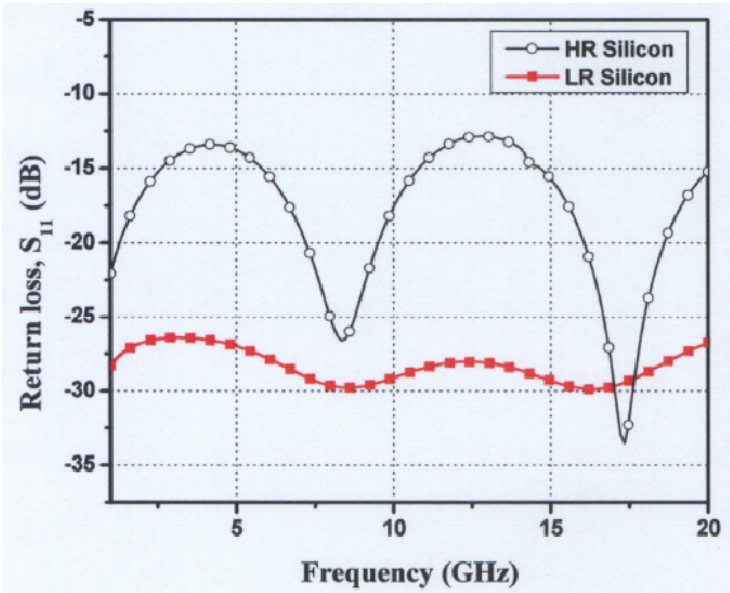
*Chapter 3 Micromachined Transmission Line and Capacitive Switches*

---

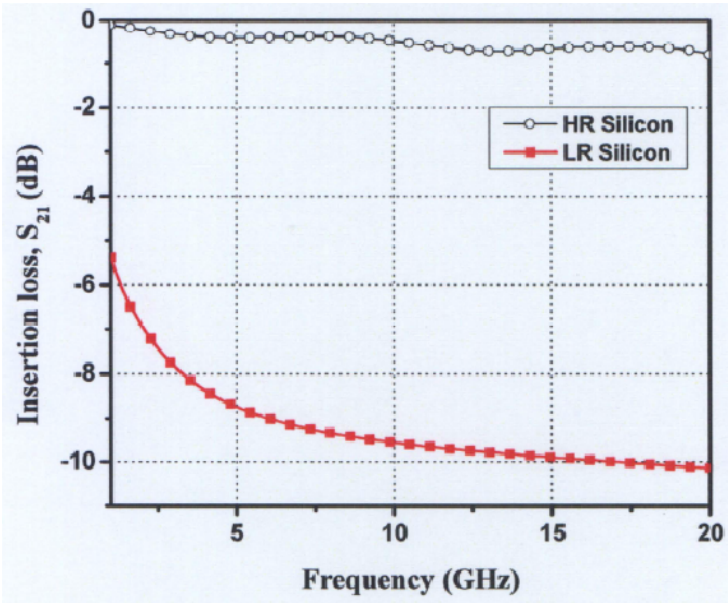
possible so that its influence on the performance of any microwave devices, such as filters, switches, and couplers etc, is negligible. The CPW structure length is 10 mm.

The simulation results of the high resistivity (HR) silicon and low resistivity (LR) silicon are as shown in Fig. 3-7. The resistivity of HR silicon is  $4000 \Omega \times \text{cm}$ , while that of LR silicon is  $20 \Omega \times \text{cm}$ . The thickness of the metal layer is  $2 \mu\text{m}$ . At 5 GHz, the insertion losses for HR silicon and LR silicon are 0.3 dB and 8.5 dB, respectively. Similarly, at 15 GHz the insertion loss for the HR silicon is 0.7 dB and for LR silicon is 10 dB. Therefore, it can be concluded that a CPW structure realized on LR silicon has higher attenuation compared to HR silicon. As a result, silicon with high resistivity is preferred in RF MEMS device fabrication.

Chapter 3 Micromachined Transmission Line and Capacitive Switches



(a)



(b)

Fig. 3-7 Comparison of the simulated results of the HR silicon and LR silicon

(a) Return loss  $S_{11}$  and (b) Insertion loss  $S_{21}$ .

Chapter 3 Micromachined Transmission Line and Capacitive Switches

3.1.4 Effects of metal thickness

The effect of metal thickness  $t$  of the CPW transmission line at the fixed frequency of 20 GHz is shown in Fig. 3-8. As expected, the attenuation rises rapidly when the metal thickness becomes less than two to three times the skin depth  $\delta$ . Fig. 3-9 shows the EM simulation results of the effect of the metal thickness on the insertion loss. The metal is gold (Au) with a conductivity of  $4.1 \times 10^7$  Siemens/m. When the metal thickness is  $4 \mu\text{m}$  and  $6 \mu\text{m}$ , the insertion losses are 0.2 dB at 5 GHz and 0.40 dB at 15 GHz, respectively. When the metal thickness is reduced to  $2 \mu\text{m}$ , a higher insertion loss of 0.75 dB at 15 GHz is observed. Therefore, it can be concluded that the thicker the deposition layer of Au, the lower the conductor loss.

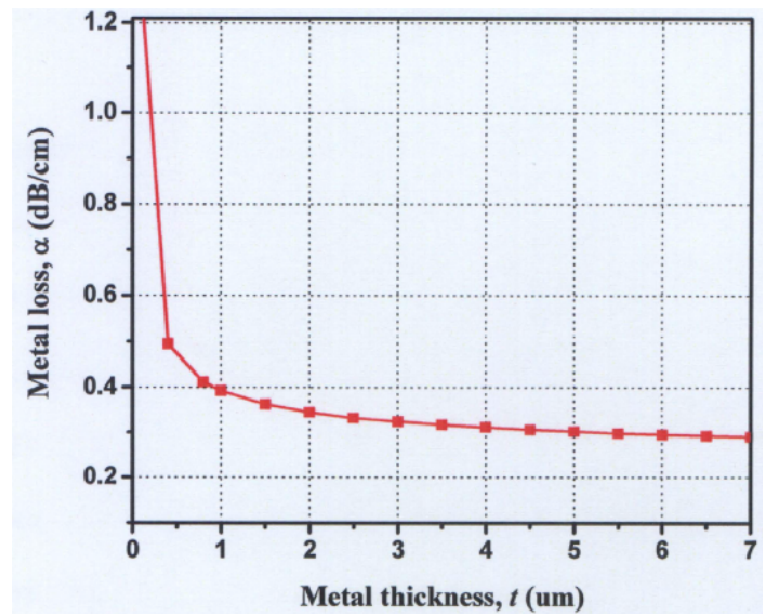


Fig. 3-8 Simulation result of the conductor loss versus different conductor thickness  $t$  at 20 GHz.

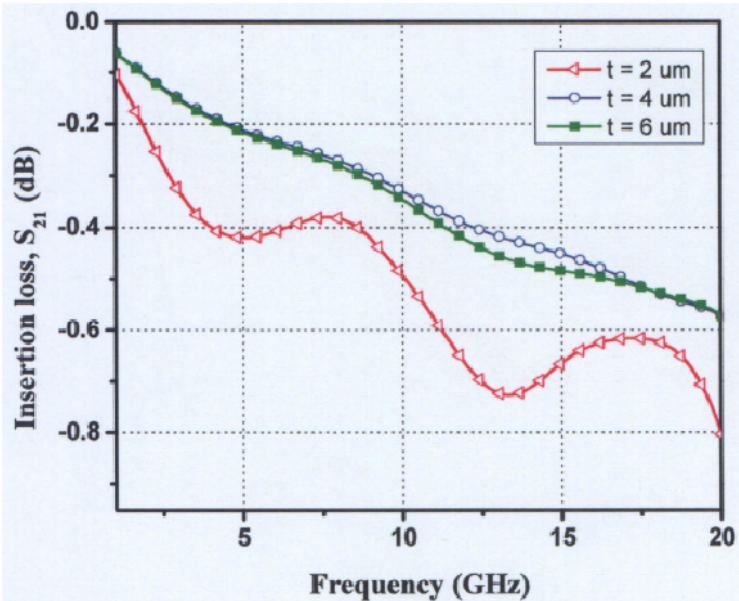


Fig. 3-9 Simulations results of the insertion loss versus frequency with different metal thickness as parameter.

3.1.5 Experimental results and discussions

The RF performance of the silicon CPW structure are measured using the HP 8510C vector network analyzer with gold tip -150  $\mu\text{m}$  pitch from cascade microtech ground-signal-ground coplanar probes. The system is calibrated using standard short-open-load-through (SOLT) on wafer calibration technique. A 5 mm plastic plate is placed between the probe chuck and the sample to remove higher order modes of propagation. All experiments are performed in the room environment without packaging. Scanning electronic microscopy (SEM) of the CPW structure is shown in Fig. 3-10.



### Chapter 3 Micromachined Transmission Line and Capacitive Switches

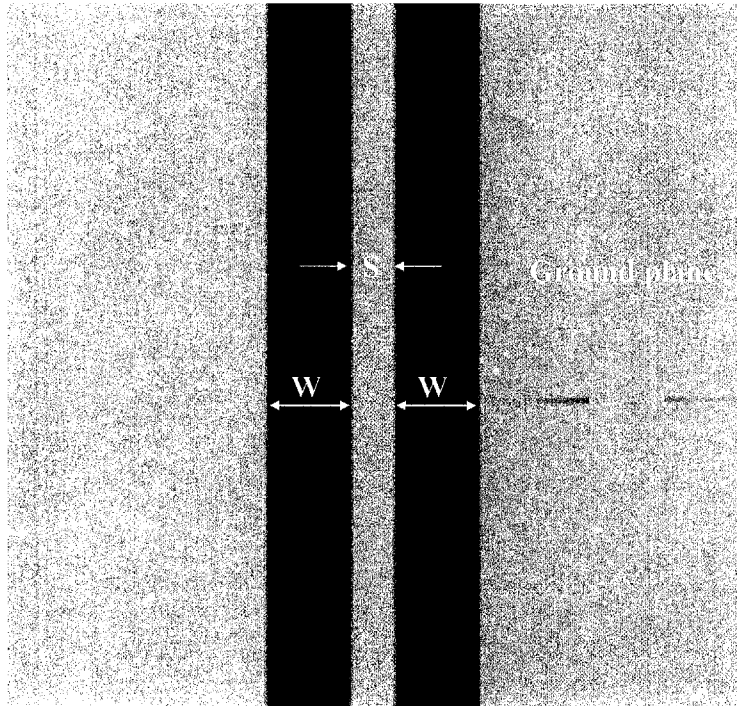
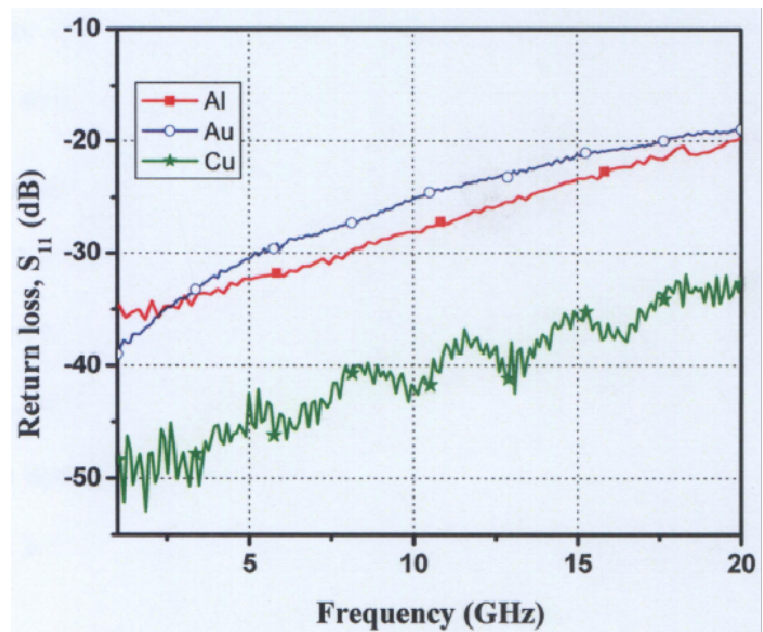


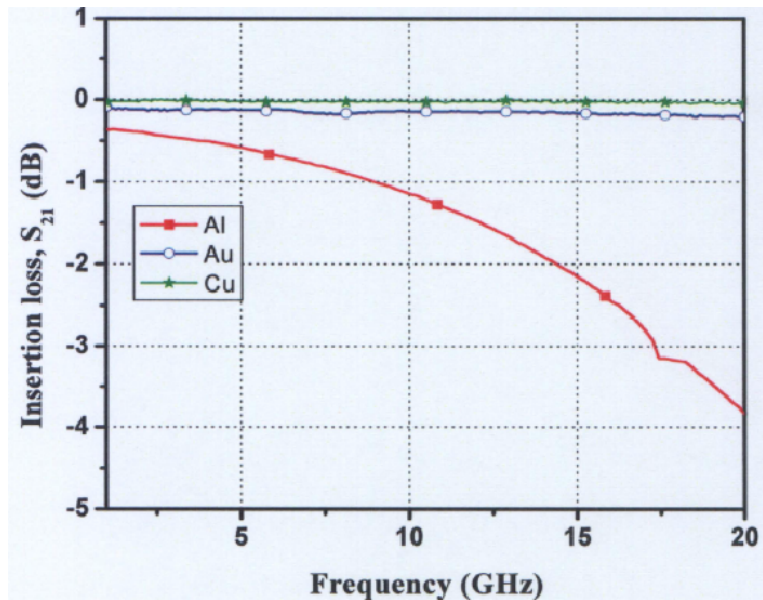
Fig. 3-10 Top view of SEM micrograph of the CPW structure.

The dimensions of the CPW structure are  $S = 70 \mu\text{m}$  and  $W = 115 \mu\text{m}$ . The CPW structure length is 10 mm. It is fabricated using high resistivity silicon substrate. The conductor layers are deposited using three different types of metal materials. The measurement results are shown in Fig. 3-11. Aluminum (Al) has a high insertion loss of 0.5 dB at 5 GHz and 2.1 dB at 15 GHz. Gold (Au) and copper (Cu) material shows excellent result in terms of the insertion loss. Gold has an insertion loss of 0.17 dB at 5 GHz and 0.2 dB at 15 GHz, whereas, copper is slightly better with an insertion loss of 0.08 dB at 5 GHz and 0.13 dB at 15 GHz. However, the CPW transmission line and RF MEMS switch are fabricated using gold as the conductor layer. The reason for this is that, although copper shows a better RF performance, gold is more advantageous due to its resistance to oxidation, increased reliability and stability.

Chapter 3 Micromachined Transmission Line and Capacitive Switches



(a)



(b)

Fig. 3-11 Measurement results of RF properties of the CPW using different material for the conductor layer (a) Return loss,  $S_{11}$ , (b) Insertion loss,  $S_{21}$ .



3.2 RF MEMS capacitive switches

The design, modeling and fabrication of the MEMS shunt capacitive switch are studied in this section.

3.2.1 Electrical modeling of the RF MEMS capacitive switch

Figure 3-12 is the schematic view of the capacitive shunt switch which is constructed on the CPW transmission line. The air gap between the metal bridge and the CPW slot is denoted as  $g_{slot}$  and the air gap between the metal bridge and the CPW central conductor at zero bias is denoted as  $g_{con}$ , as shown in Fig 3-12 (b). All the design parameters are listed in Table 3-2.

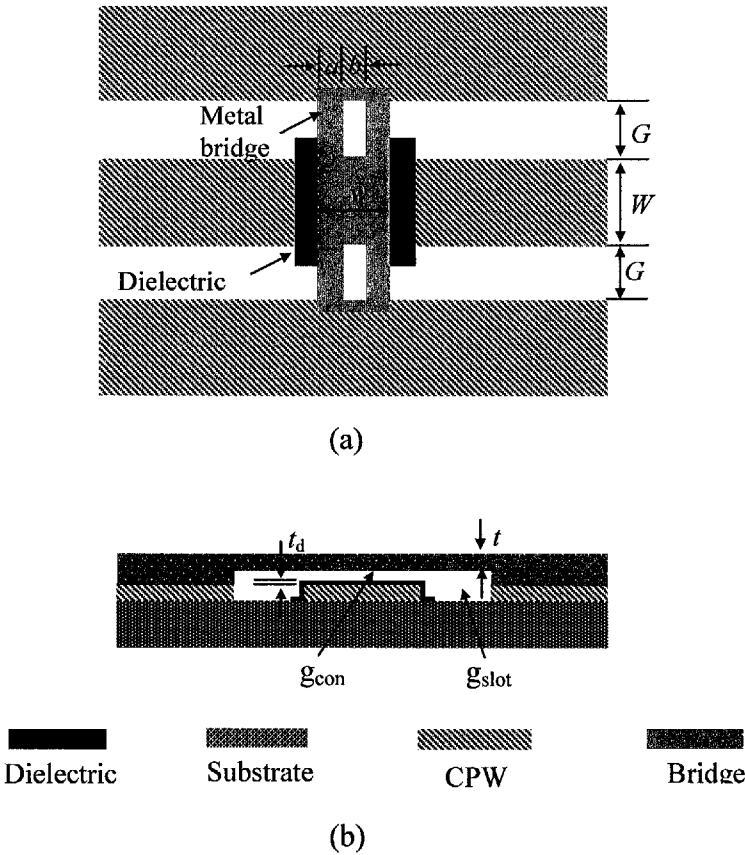


Fig. 3-12 Schematic of the RF capacitive switch; (a) Top view and (b) Cross sectional view.

Chapter 3 Micromachined Transmission Line and Capacitive Switches

Table 3-2 Designed parameters of the capacitive switch.

Design Parameters	Value
$a$ (μm)	20
$b$ (μm)	20
$w$ (μm)	50
$W$ (μm)	70
$G$ (μm)	40
$g_{con}$ (μm)	2.0
$t$ (μm)	1.50
$t_d$ (μm)	0.15
Al Young's modulus $E$ (GPa)	70
Al Poisson's ratio	0.35
$\sigma$ (MPa)	20

This switch is modeled using two short sections of transmission lines with characteristic impedance  $Z_0$ , and a lumped resistance-inductance-capacitance (RLC) model of the bridge representing an up-state or a down-state of the switch. The equivalent circuit of the switch is shown in Fig. 3-13. The switch behaves as a capacitor when the frequency is below the inductance-capacitance (LC) series resonant frequency and as an inductor when the frequency is above the LC series resonant frequency. At resonance, it reduces to pure resistance.

Based on the parallel-plate capacitance model, the capacitances of the up-state and the down-state of the switches can be expressed as,

$$C_u = \frac{\epsilon_0 A}{g_{con} + t_d / \epsilon_r} + C_f \tag{3-17}$$

## Chapter 3 Micromachined Transmission Line and Capacitive Switches

$$C_d = \frac{\epsilon_0 \epsilon_r A}{t_d} \quad (3-18)$$

where  $C_u$  and  $C_d$  are the designed up-state and down-state capacitances, respectively.  $C_f$  is the fringing field capacitance,  $t_d$  is the thickness of the dielectric layer,  $\epsilon_0$  is the permittivity of free space and  $\epsilon_r$  is the relative permittivity of the dielectric layer (7.6 for SiN),  $A$  is the total bridge area above the CPW center conductor and  $A = w \cdot W$  where  $w$  is the width of the bridge,  $W$  is the width of the CPW central conductor under the metal bridge.

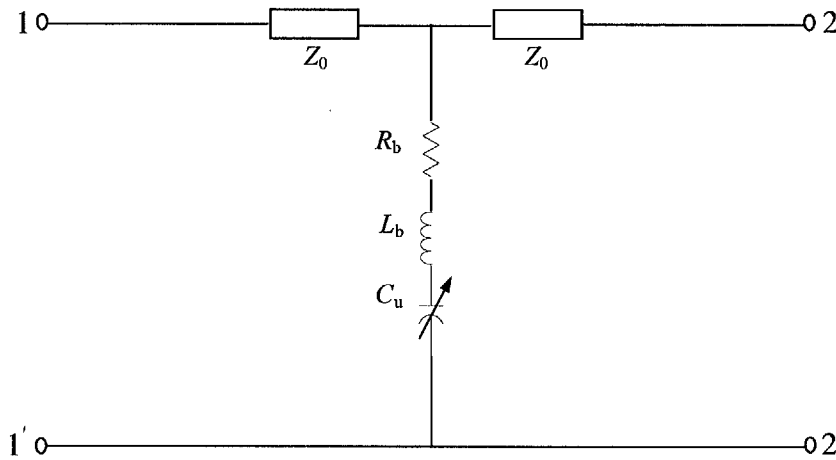


Fig. 3-13. Equivalent circuit of the capacitive shunt switch.

The relationship between the capacitances and the RF performance of the switch can be expressed as [3],

$$S_{11} = \frac{-j\omega C_u Z_0}{2 + j\omega C_u Z_0} \quad (3-19)$$

---

*Chapter 3 Micromachined Transmission Line and Capacitive Switches*

---

$$S_{21} = \frac{1}{1 + j\omega C_d Z_0 / 2} \quad (3-20)$$

where  $S_{11}$  and  $S_{21}$  are the up-state return loss and the down-state insertion loss, respectively,  $Z_0$  is the characteristic impedance of the CPW,  $j$  is square root of -1. The angular frequency  $\omega$  is selected to be lower than half of the LC resonant angular frequency to avoid the effects of the bridge resistance ( $R$ ) and inductance ( $L$ ).

### 3.2.2 Mechanical design

In this section, the mechanical design of the MEMS switch is discussed. When a DC bias voltage is applied on the MEMS bridges i.e. between the fixed electrode and the beam, it acts like a parallel plate capacitor and its capacitance can be expressed as [3],

$$C = \frac{Ww\epsilon_0}{g} \quad (3-21)$$

where  $w = 50 \mu\text{m}$  is the width of the bridge,  $W = 70 \mu\text{m}$  is the width of the CPW central conductor under the metal bridge,  $g$  is the gap distance between the conductor and dielectric layer, and  $\epsilon_0 = 8.854 \times 10^{-12} \text{ F/m}$  is the permittivity of the vacuum. The capacitance between the fixed electrode and the beam is larger than that calculated by Eq. (3-21) due to fringe effects capacitance, from the side walls and the back side. For a smaller distance between plates ( $g \ll w$ ), the capacitance due to fringe effect can be approximated as [3],

$$C_0 = C \left\{ 1 + \frac{g}{2\pi w} \ln \frac{2\pi w}{g} + \frac{g}{2\pi w} \ln \left[ 1 + \frac{2h}{g} + 2\sqrt{\frac{h}{g} + \frac{h^2}{g^2}} \right] \right\} \quad (3-22)$$

Chapter 3 Micromachined Transmission Line and Capacitive Switches

Eq. (3-22) can be written as  $C_0 \equiv \beta C$ , where  $\beta$  is a correction factor of capacitance for the fringe effect, which is dependent on the dimensions of the structure,

$$\beta = 1 + \frac{g}{2\pi w} \ln \frac{2\pi w}{g} + \frac{g}{2\pi w} \ln \left[ 1 + \frac{2h}{g} + 2\sqrt{\frac{h}{g} + \frac{h^2}{g^2}} \right] \tag{3-23}$$

where  $h$  is the thickness of the bridge.

Figure 3-14 shows the relationship between the capacitance and the fringe effects of the switch. It clearly shows that the capacitance due to the fringe effects is greater than 4% of the normal capacitance. When the gap height is  $2\mu\text{m}$ , the fringe capacitance is 16.1076 fF and the normal capacitance is 15.49 fF.

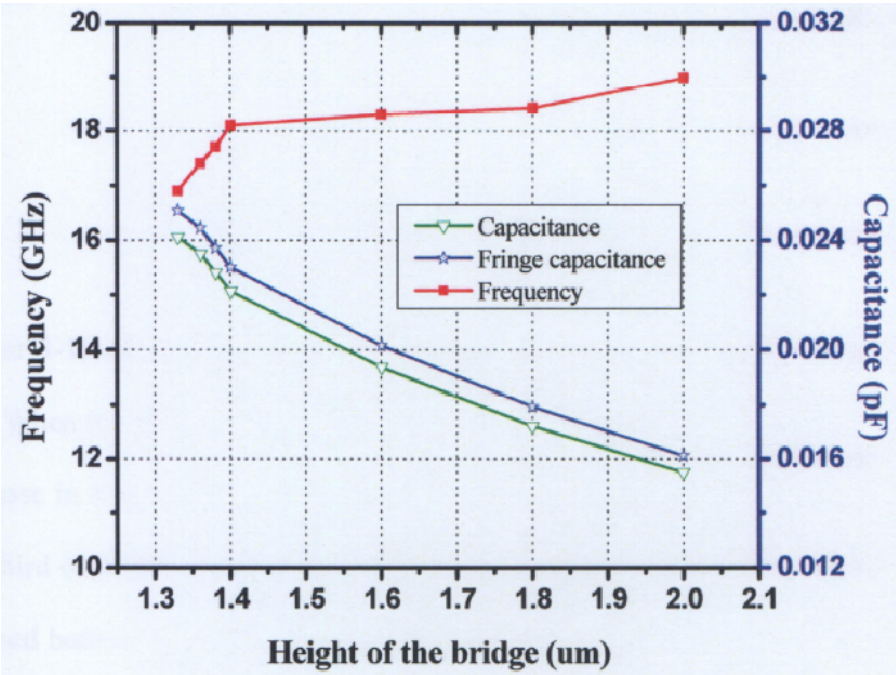


Fig. 3-14. Simulation results of frequency and capacitance versus different height of the bridge.

---

*Chapter 3 Micromachined Transmission Line and Capacitive Switches*

---

The relationship between the gap height of the bridge and the applied voltage are discussed here as follows. The electrostatic force is induced when a DC bias voltage is applied on the MEMS bridges. This electrostatic force is evenly distributed across the entire area of the beam above the electrode. Therefore, the appropriate spring constant value can determine the distance that the beam moves under the applied force. Equating the applied electrostatic force and the mechanical restoring force due to the stiffness,  $k$  of the beam and it can be expressed as,

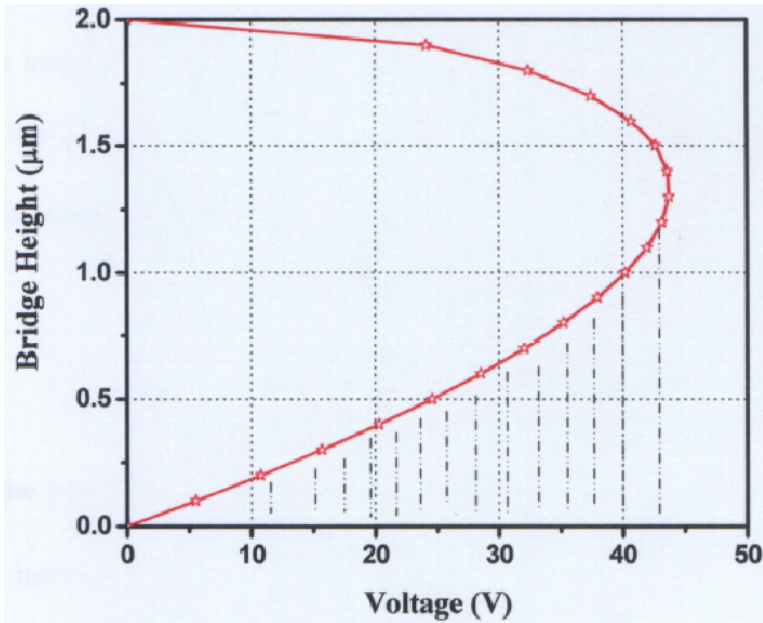
$$\frac{\epsilon_0 W W V^2}{2g^2} = k(g_{con} - g) \quad (3-24)$$

where  $k = 25$  N/m,  $g_{con}$  is the zero bias bridge height.  $V$  is the drive voltage that can be derived as,

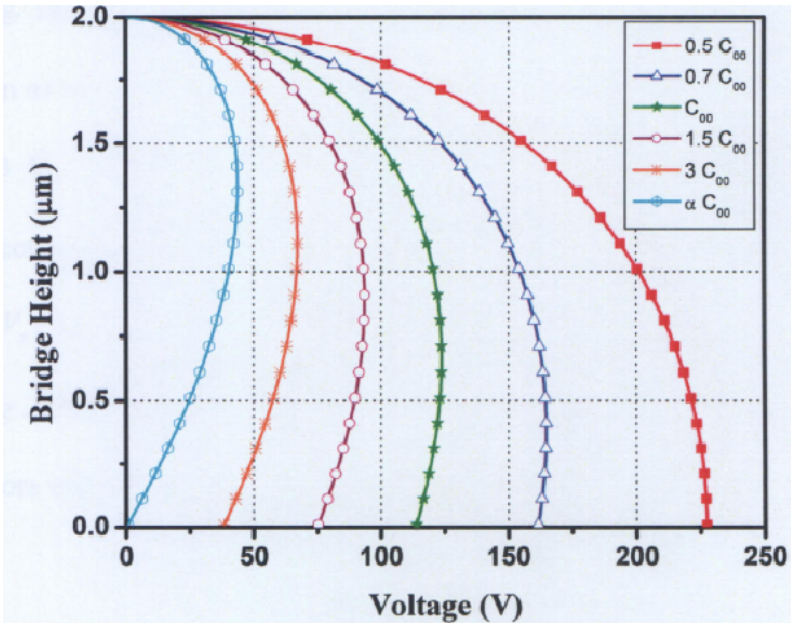
$$V = \sqrt{\frac{2k}{\epsilon_0 W W} g^2 (g_{con} - g)} \quad (3-25)$$

Figure 3-15 shows the relationship plot between the bridge height and the applied voltage. When the derived voltage is increased, the beam starts to move downward due to the increase in the electric field. When its distance from the bottom electrode is reduced to one-third of the initial gap height ( $1/3 g_{con}$ ), the beam becomes unstable and collapses to the fixed bottom electrode. This is known as *pull-in voltage*. From Fig. 3-15, it can be seen that the switch operates at a stable state before the height of the bridge reaches  $1.3 \mu\text{m}$  height. When the voltage is raised above  $43.68$  V, the switch collapses to the fixed electrode.

Chapter 3 Micromachined Transmission Line and Capacitive Switches



(a)



(b)

Fig. 3-15. Relationship between the applied voltage and the bridge height; (a) Pull in voltage effect, and (b) Elimination of the pull-in effect for different values of the series feedback capacitor.



### Chapter 3 Micromachined Transmission Line and Capacitive Switches

---

When the series feedback capacitor is connected with the micromachined bridge capacitor, the instability in the electrostatic actuation can be reduced and the pull down distance can be controlled. When the applied voltage  $V_s$  is divided between the two capacitors, the voltage across the micromachined bridge capacitor is given by,

$$V = \frac{V_s}{1 + C/C_s} \quad (3-26)$$

where  $C$  is the micromachined bridge capacitor and  $C_s$  is the fixed series capacitor. When  $V_s$  is increased, the applied voltage of the micromachined bridge increases, causing the bridge to pull down and  $C$  to increase. This results in positive feedback and the resulting instability at  $2g_{con}/3$  as discussed above. In the series stabilization configuration as shown in 3-15 (b), the increase in  $C$  results in less voltage across  $C$  and more across  $C_s$ , thereby achieving negative feedback. The position at which the instability occurs is determined by first finding the force on the micromachined capacitor in terms of  $V_s$ , solving for  $V_s$ , and taking the derivative of  $V_s$  with respect to the bridge gap height  $g$ . The force on the bridge is found by considering the change in energy of both capacitors with respect to the bridge gap height  $g$  [3],

$$F_e = \frac{dU}{dg} = \frac{V_s}{2} \frac{d}{dg} \left( \frac{CC_s}{C + C_s} \right) = -\frac{\epsilon_0 W w V_s^2}{2(g + Kg_{con})^2} \quad (3-27)$$

where  $K = C_{00}/C_s$ ,  $C_{00} = \epsilon_0 wW/g_{con}$  is the zero bias bridge capacitance and  $d/d_g$  is the derivative with respect to bridge height  $g$ . Equating this force with the force due to stiffness of the bridge, the applied voltage is solved in terms of the bridge gap height  $g$ .



---

**Chapter 3 Micromachined Transmission Line and Capacitive Switches**

---

$$V_s = \sqrt{\frac{2kg_{con}^3}{\epsilon_0 Ww} \left( \frac{g}{g_{con}} + K \right)^2 \left( 1 - \frac{g}{g_{con}} \right)} \quad (3-28)$$

Taking the derivative of Eq. (3-28) with respect to  $g$  and setting it to zero, the position of the instability can be found as,

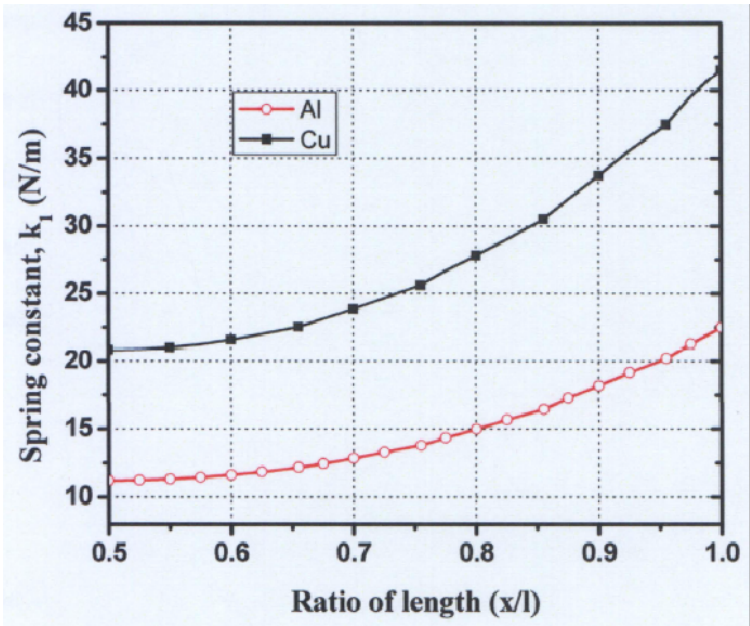
$$g_p = \frac{g_{con}}{3} (2 - K) \quad (3-29)$$

when  $K = 0$  ( with no series feedback capacitor), the instability occurs at the expected height of  $2g_{con}/3$ . From Eq. (3-29), it results that if  $K = 2$  the instability is completely eliminated ( $g_p = 0$ ). However, the drawback of this method is that the increase in the stable region of an electrostatically actuated bridge increases the voltage required to pull the bridge completely down. Substituting Eq. (3-29) into Eq. (3-28), the pull down voltage is given as,

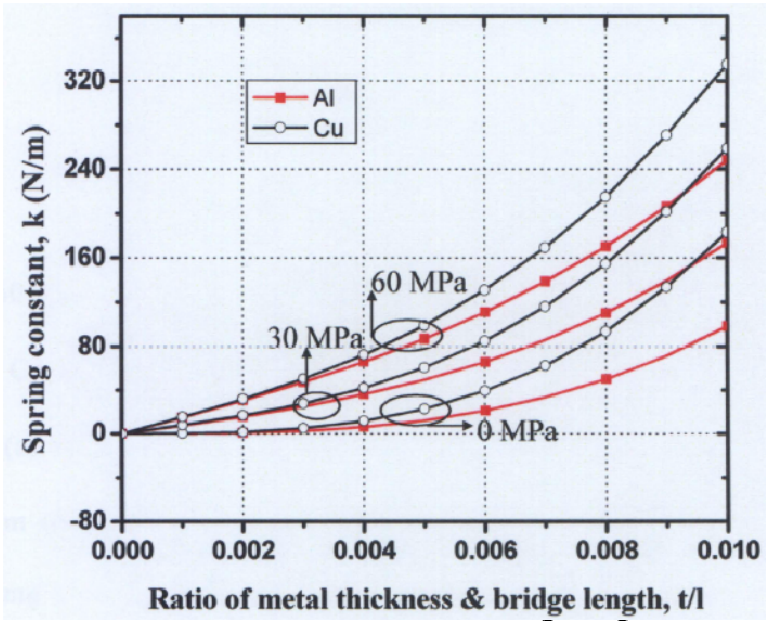
$$V_{sp} = \frac{8kg_{con}^3}{27\epsilon_0 Ww} (1 + K)^3 \quad (3-30)$$

Compared with the standard pull-down voltage given by Eq. (3-25), the voltage is increased by a factor of  $(1 + K)^{3/2}$ . This implies that when  $K = 2$ , the instability is eliminated but the pull-down voltage is increased by a factor of 5.2. Fig. 3-15 (b) shows the change of the bridge gap height as a function of applied voltage. The series capacitance varies from  $0.5 C_{00}$  to  $\infty$ . At  $0.5 C_{00}$  the instability can be eliminated when the applied voltage is increased to 225 volts as derived in Eq. (3-30). Therefore, for optimum design there is a trade-off between the applied voltage and the high stability of the micromachined bridge.

Chapter 3 Micromachined Transmission Line and Capacitive Switches



(a)



(b)

Fig. 3-16. (a) Spring constant of the beam with  $t/l = 0.005$ ; (b) Spring constant versus residual stress.

### Chapter 3 Micromachined Transmission Line and Capacitive Switches

It is assumed the bridge of the switch is a fixed-fixed beam. The stiffness of the bridge  $k_1$  depends on the bridge's material Young's modulus  $E$  and the moment of inertia  $I$ . The other part of the spring constant  $k_2$ , is due to the biaxial residual stress  $\sigma$  exist within the beam and strongly depends on the fabrication process. The force is distributed over the central portion of the fixed-fixed bridge due to the applied voltage on the central conductor. The equation for the deflection of the fixed-fixed beam can be expressed as,

$$y = \frac{2}{EI} \int_{l/2}^x \frac{\xi}{48} (l^3 - 6l^2x + 9lx^2 - 4x^3) dx \quad (3-31)$$

where  $\xi$  is the load per unit lengths so that the total load is  $P = \xi l$ . The expression for the spring constant is defined as,

$$k_1 = 32Ew \left( \frac{t}{l} \right)^3 \frac{1}{\left( \frac{x}{l} \right) \left( 1 - \frac{x}{l} \right)^2} \quad (3-32)$$

where  $w = 50\mu\text{m}$  is the width of the bridge, Young's modulus of Al is  $E = 70\text{ GPa}$  and  $130\text{ GPa}$  for Cu, the metal thickness is  $t = 1.5\mu\text{m}$ , the length of the bridge is  $l = 300\mu\text{m}$ . In Fig. 3-16 (a), the spring constant  $k_1$  is plotted against  $x/l$  ratio for two different metals i.e. aluminum and copper. The spring constant of copper is higher than aluminum because Young's modulus for copper is higher. The biaxial residual stress is developed when the beam that is deflected and stretched. The spring constant due to the residual stress is given by,

---

**Chapter 3 Micromachined Transmission Line and Capacitive Switches**

---

$$k_2 = 8\sigma(1-\nu)w\left(\frac{t}{l}\right)\left(\frac{1}{3-2(x/l)}\right) \quad (3-33)$$

where  $\sigma$  is the residual stress and  $\nu$  is the Poisson's ratio.

The distributed force is above the centre conductor. Based on Eqs. (3-32) and (3-33), when  $x = 2l/3$ , the total spring constant  $k$  is given as,

$$k = 32Ew\left(\frac{t}{l}\right)^3\left(\frac{27}{49}\right) + 8\sigma(1-\nu)w\left(\frac{t}{l}\right)\left(\frac{3}{5}\right) \quad (3-34)$$

Figure 3-16 (b) shows the total spring constant using Eqs. (3-34) for the aluminum and copper beams for residual stress values of 0 MPa, 30 MPa, and 60 MPa. For  $l = 300\ \mu\text{m}$  and  $t = 0.5 - 1.5\ \mu\text{m}$  ( $t/l = 0.0015 - 0.0045$ ), the spring constant is dominated by the residual stress component  $k_2$  for  $\sigma > 10\ \text{MPa} - 20\ \text{MPa}$ .

A simple one-dimensional (1-D) nonlinear model treats the MEMS switch as a single lumped mass and applies classical Newton mechanics to predict the dynamic behavior under the applied electrostatic force [128]. The differential motion of equation for the bridge can be expressed as [128],

$$mz'' + bz' + K_z z = F_e + F_c \quad (3-35)$$

where

$$F_e = \frac{\epsilon_0 W w V^2}{2\left(g_{con} + \frac{t_d}{\epsilon_r} - z\right)^2} \quad (3-35\ a)$$

$$b = \frac{K_z}{\omega_0 \times Q} \quad (3-35\ b)$$

---

**Chapter 3 Micromachined Transmission Line and Capacitive Switches**

---

$$\omega_0 = \sqrt{\frac{K_z}{m}} \quad (3-35 \text{ c})$$

$$Q = Q_0 \left( 1 - \left( \frac{z}{g_{con}} \right)^2 \right)^{3/2} \left( 1 + 9.638 \left( \frac{\lambda}{g_{con} - z} \right)^{1.159} \right) \quad (3-35 \text{ d})$$

$$F_c = \frac{m_1 W w}{(g_{con} - z)^3} - \frac{m_2 W w}{(g_{con} - z)^{10}} \quad (3-35 \text{ e})$$

where,  $m$  is the mass,  $b$  is the damping coefficient,  $K_z$  is the switch spring constant in the  $z$  direction,  $m_1$  is the mass of the switch and  $m_2$  is the mass of the dielectric layer,  $\epsilon_r$  and  $t_d$  are the dielectric layer constant and thickness, respectively,  $V$  is the applied voltage,  $F_e$  is the electrostatic force on the switch, and  $F_c$  is the contact force when the switch touches the dielectric,  $\omega_0$  is the resonant frequency and  $Q$  is the quality factor.

The viscous damping can be considered constant for small displacement, but it is not the case when the switch is moving completely towards the substrate. The model for the switching speed calculation is based on [40], where these effects are taken into account. Eq. (3-35d) calculates the switch quality factor and takes into account the damping dependence on the switch height. The variable  $\lambda$  is called the mean free path and is approximately  $0.1\mu\text{m}$  at standard temperature pressure (STP). The damping coefficient, which is related to  $Q_0$  by Eq. (3-35b), has been derived in [40] for a switch as,

Chapter 3 Micromachined Transmission Line and Capacitive Switches

$$b = \frac{3}{2\pi} \frac{\mu W w}{g_{con}^3} \tag{3-35 f}$$

Where  $\mu$  is the air viscosity. However, the holes included in the switch allow the air underneath to escape more easily, thus reducing the damping coefficient and increasing the  $Q$  of the switch structure. Finally, Eq. (3-35e) is used to provide a stable solution to the simulation when the switch contacts the dielectric layer.

Fig. 3-17 shows the pull down time of the MEMS switch. When the voltage is applied, the bridge starts to move down and takes  $8\ \mu\text{s}$  to  $9\ \mu\text{s}$  to reach the height of  $2/3\ g_{con}$ . When the voltage is further increased, the bridge will move down quickly until it touches the dielectric layer at pull-down voltage of  $43.68\ \text{V}$ . Therefore, the pull down voltage and pull down time of the switch is dependent on  $2/3\ g_{con}$  of the height between the bridge and the dielectric layer.

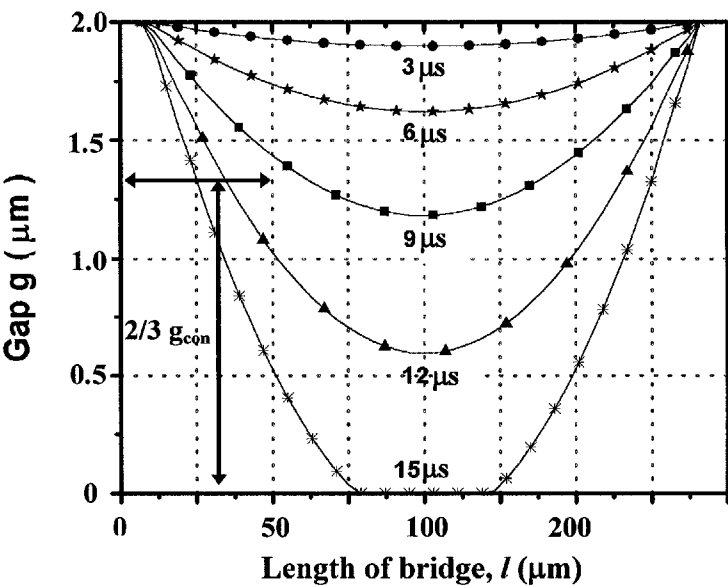


Fig. 3-17. Simulation results of the pull down time for different gap heights of the bridge.

### Chapter 3 Micromachined Transmission Line and Capacitive Switches

#### 3.2.3 Planarization and roughness effect

When the bridge is pulled down, considering that the bridge is not ideally flat, only the part of the bridge area which is above the CPW center conductor touches the dielectric layer. The down-state capacitance in Eq. (3-21) is written as,

$$C_d = C_d' + C_d'' \quad (3-36)$$

where  $C_d'$  is the down-state capacitance caused by the contact area when the bridge touches the dielectric layer, and  $C_d''$  is the down-state capacitance caused by the non-contact area due to the air gap between the bridge and the dielectric layer, as shown in Fig. 3-18.

From Fig. 3-18, the  $C_d'$  and the  $C_d''$  can be written as

$$C_d' = p \frac{\epsilon_0 A}{t_d / \epsilon_r} \quad (3-37)$$

where  $t_d$  is the thickness of the dielectric layer,  $\epsilon_r$  is the relative permittivity of the dielectric layer (7.6 for silicon nitride, SiN), and,

$$C_d'' = (1 - p) \frac{\epsilon_0 A}{d + t_d / \epsilon_r} \quad (3-38)$$

where  $p$  is the ratio of the contact area between the bridge and the dielectric layer to the total bridge area above the CPW center conductor  $A$ , and  $d$  is the average air gap height of the non-contact area when the bridge is pulled down as shown in Fig. 3-18. The air gap  $d$  varies between 0 and  $0.2 \mu\text{m}$ .

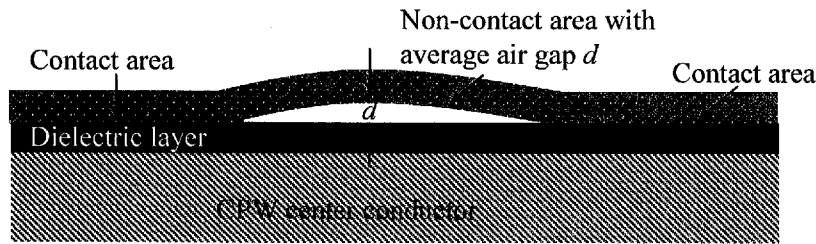


Fig. 3-18 Schematic view of contact condition after bridge pulled down.

Besides the planarization, the smaller roughness of the dielectric layer will increase the contact area between the bridge and the dielectric layer, and consequently will result in a higher down-state capacitance. Since the r.m.s value of the surface roughness of the dielectric layer is less than 50 nm [129], its effect is less significant compared to the planarization of the bridge.

#### 3.2.4 Fabrication process flow of MEMS switches

As discussed in the previous section, since the planarization of the bridge plays a significant role in reducing the contact area between the bridge and the dielectric layer, a new planarization process is proposed by filling the CPW slot with photoresist which can effectively improve the flatness of the bridge.

The switches are fabricated using a surface micromachining process with five masks [130]. High-resistivity ( $> 4000 \Omega\text{-cm}$ ) silicon wafers with thickness of  $675 \mu\text{m}$  are used as substrate. The fabrication process flow is shown in Fig. 3-19. (a) A layer of  $0.5 \mu\text{m}$  thick oxide is deposited on the substrate as a buffer layer; (b) a layer of  $2 \mu\text{m}$  thick gold is sputtered and patterned for the CPW transmission line; (c) a  $0.15 \mu\text{m}$  thick



Chapter 3 Micromachined Transmission Line and Capacitive Switches

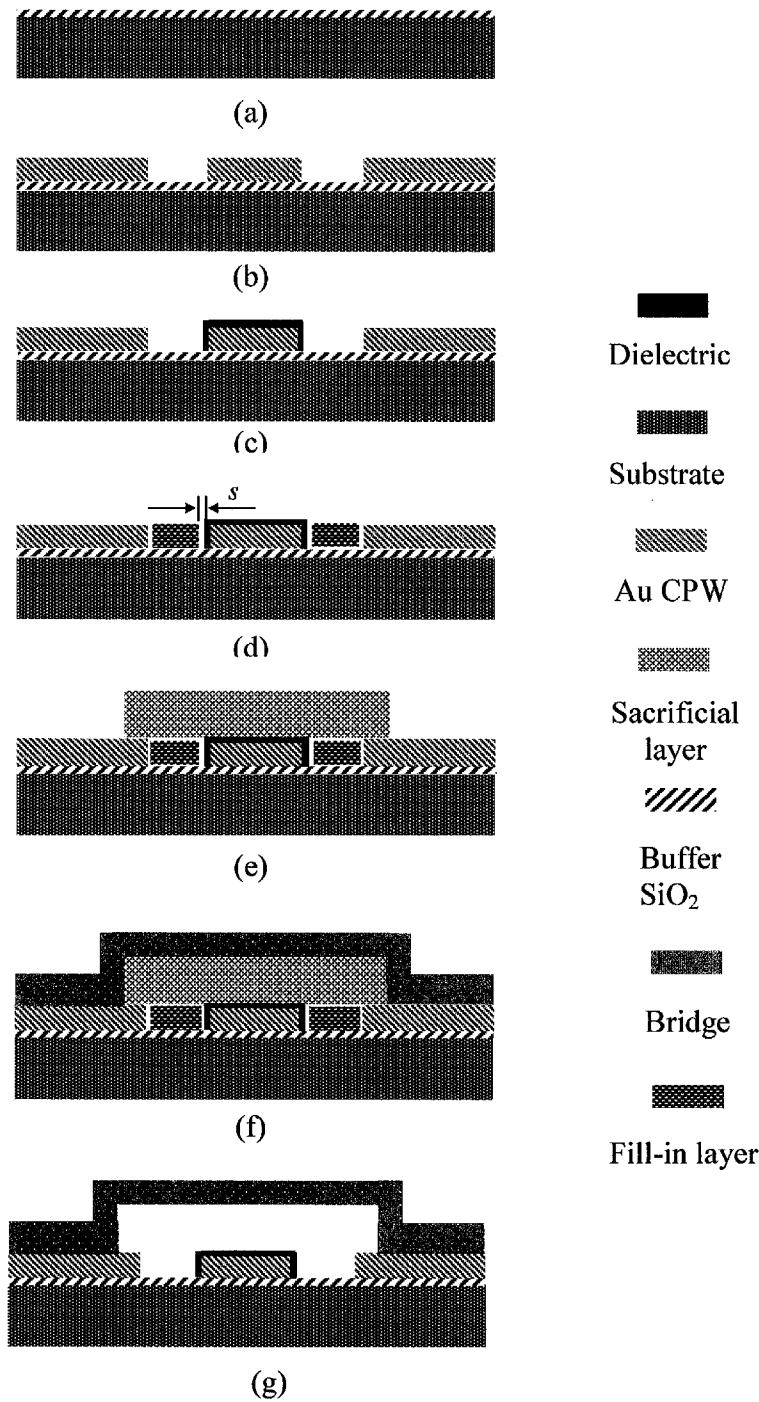


Fig. 3-19 Fabrication process flow.

### *Chapter 3 Micromachined Transmission Line and Capacitive Switches*

---

plasma enhanced chemical vapor deposition (PECVD) SiN is deposited and patterned as the insulating layer between the CPW transmission line and the bridge; (d) a 1.5  $\mu\text{m}$  thick of photo-resist is spun coated and patterned to fill in the CPW slot (henceforth referred to as fill-in photoresist and this process is known as the planarization step, which is a key step to obtain a flat metal bridge); (e) a 2  $\mu\text{m}$  thick of photoresist sacrificial layer is spun coated and patterned (refer to this layer of photoresist as sacrificial photoresist); (f) a 1.5  $\mu\text{m}$  thick layer of gold thin film is evaporated and wet etched to form the bridge; and (g) all the photoresist is etched away by oxygen plasma etching to free the metal bridge.

#### **3.2.4 Experimental results and discussions**

The RF performance of the switch is characterized using an HP8510C vector network analyzer and RF probe station. A full Thru-Reflect-Line (TRL) routine is used to calibrate with NIST software MULTICAL.

Two different types of switches are fabricated: Switch A and Switch B are fabricated without and with the proposed planarization process respectively. Figs. 3-20 (a) and (b) show the surface profiles of the Switch A and B, respectively. These profiles are obtained after the wet etching but before the release of the switching bridge. For Switch A, the portion of the bridge above the CPW slot is 1.2  $\mu\text{m}$  lower than the portion of the bridge above the CPW central conductor. For Switch B, the portion of the bridge above the CPW slot is 0.5  $\mu\text{m}$  higher than the portion of the bridge above the CPW central conductor.

Chapter 3 Micromachined Transmission Line and Capacitive Switches

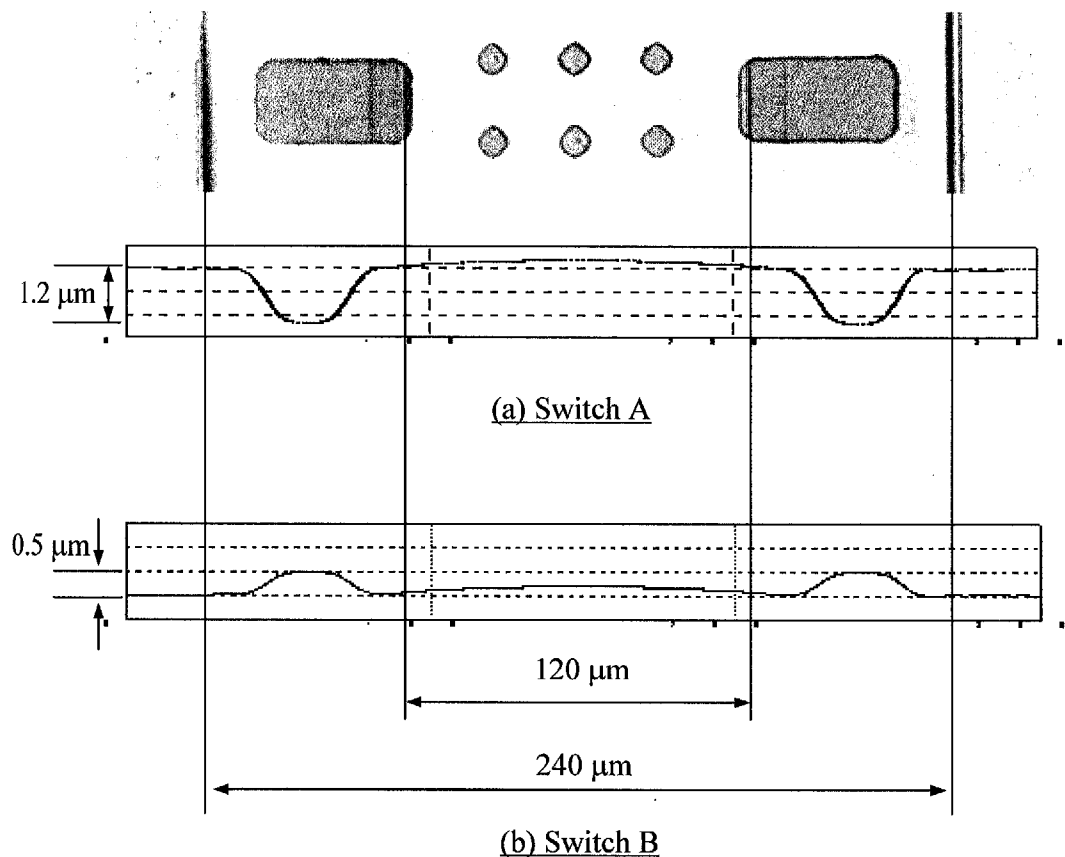
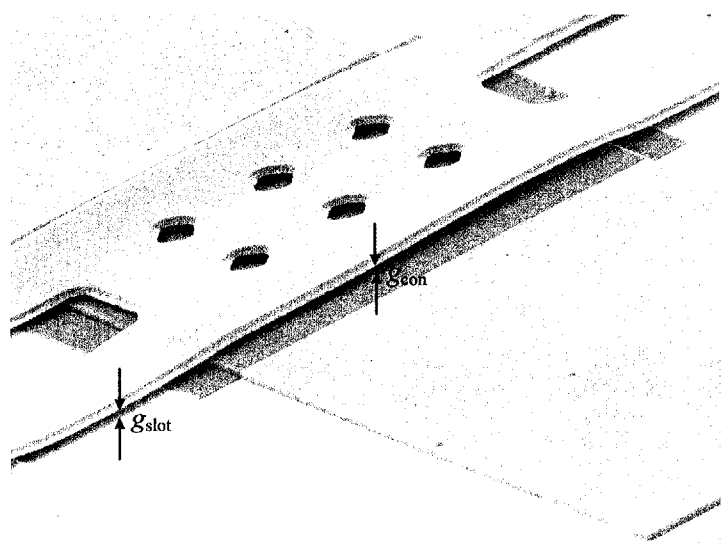


Fig. 3-20 Surface profiles of the capacitive shunt switch (a) Switch A: without fill-in photoresist and (b) Switch B: with fill-in photoresist.

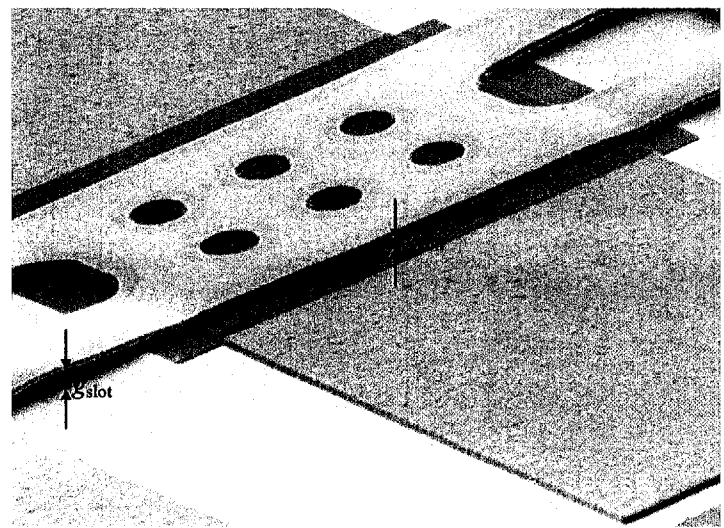
Fig. 3-21 shows the SEM photos of the two switches after releasing. The etching holes on the bridge provide easier release and reduce the damping effect. Fig. 3-21 (a) shows that the  $g_{\text{slot}}$  is smaller than the  $g_{\text{con}}$  in Switch A. When Switch A is driven down, it touches the CPW slot edges first. After that, any further pull down becomes difficult which makes closer contact between the metal bridge and the dielectric layer impossible. On the contrary, Fig. 3-21 (b) shows that the  $g_{\text{slot}}$  is larger than the  $g_{\text{con}}$  in Switch B. When Switch B is driven down the metal bridge touches the dielectric layer first, which

Chapter 3 Micromachined Transmission Line and Capacitive Switches

improves the contact between the bridge and the dielectric layer. Assume that all the bridge area above the CPW center conductor touches the dielectric layer when the bridge is pulled down.



(a)



(b)

Fig. 3-21. SEM micrographs of the capacitive shunt switches; (a) Switch A: without fill-in photoresist and (b) Switch B: with fill-in photoresist.

Chapter 3 Micromachined Transmission Line and Capacitive Switches

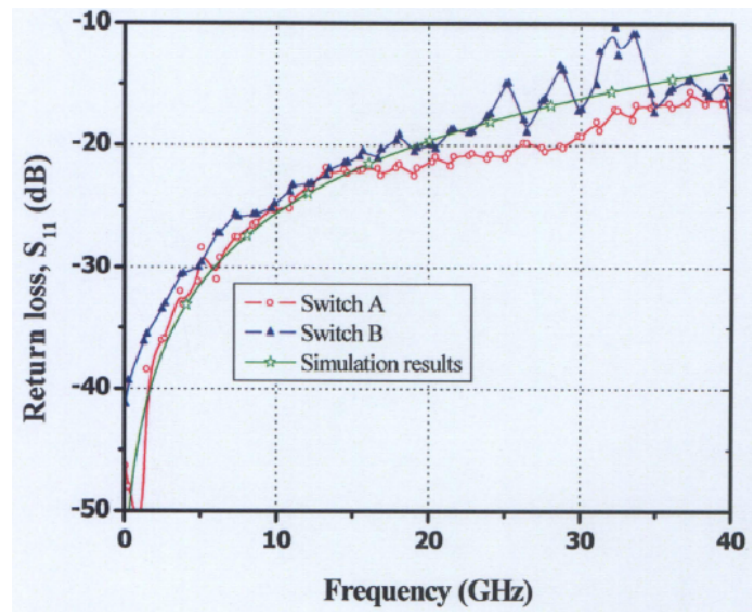
Figure 3-22 (a) and 3-22 (b) show the comparison of the simulated and measured S-parameters for Switch A and Switch B at up-state. At the up-state, the measurement results of Switch A and Switch B are comparable to the simulation results. The extracted up-state capacitance ( $C_u$ ) is 17.4 fF. At the down-state, the measured isolation of Switch A is inferior compared to the simulation results as shown in Table 3-3. The simulations are conducted using Ansoft’s high frequency simulation software (HFSS) based on finite element method [131].

Table 3-3 Comparison of down-state isolations and capacitances.

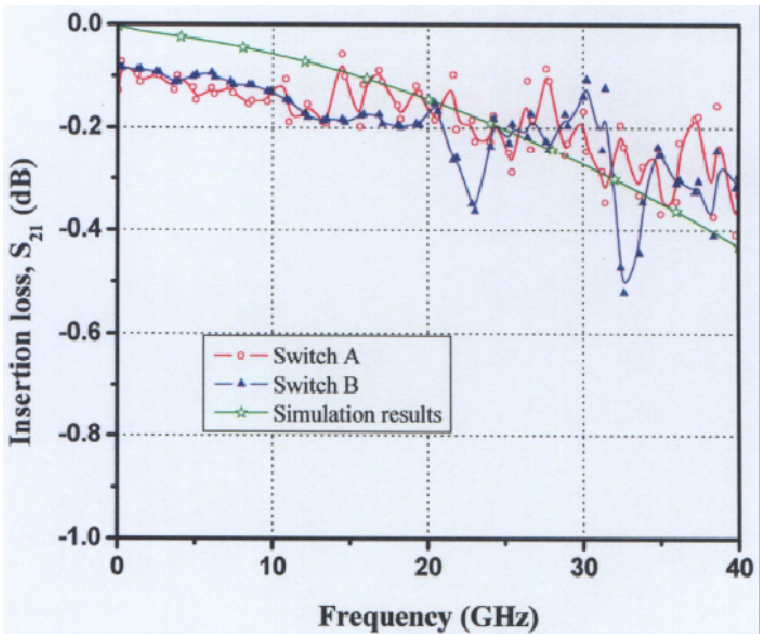
	Switch A	Switch B	Simulation
Isolation at 15 GHz	7.5 dB	9.7 dB	18.0 dB
Isolation at 40 GHz	17.0 dB	27.0 dB	28.0 dB
Down-state capacitance (pF)	$C_{dA} = 1.0$	$C_{dB} = 1.3$	$C_d = 3.0$

It is noted from Fig. 3-22 (a) and (b) that Switch A and Switch B have comparable up-state RF performance. However, the measured down-state isolation of Switch B is improved by 2.2 dB at 15 GHz and 10 dB at 40 GHz compared to that of Switch A. Additionally, the measured down-state capacitance of Switch B is 0.3 pF (30%) larger than Switch A. This is shown in Table 3-3 and Fig. 3-23 (a) and (b). This implies that the contact between the bridge and the dielectric layer for Switch B is 63% better compared to Switch A. The insertion loss of the switch is 0.1 dB at 15 GHz. The total length of CPW on which the MEMS switch is fabricated is 500  $\mu\text{m}$ .

Chapter 3 Micromachined Transmission Line and Capacitive Switches



(a)

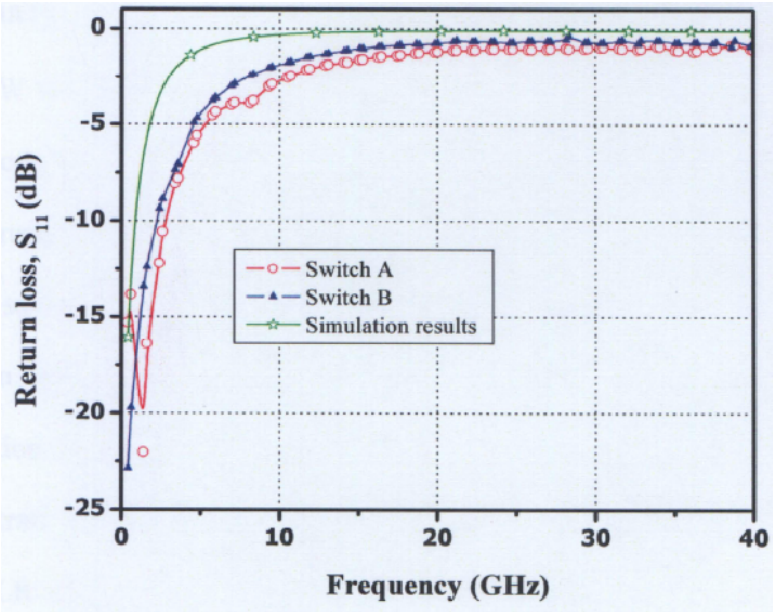


(b)

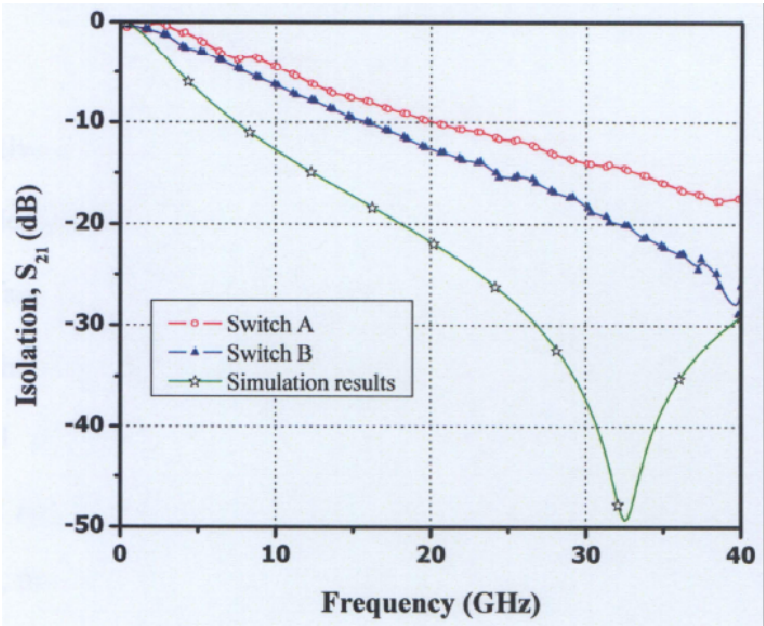
Fig. 3-22 Comparison of simulated and measured S-parameters for up state capacitance; (a) Return loss,  $S_{11}$  and (b) Insertion loss,  $S_{21}$ .



Chapter 3 Micromachined Transmission Line and Capacitive Switches



(a)



(b)

Fig. 3-23 Comparison of simulated and measured S-parameters of down state capacitance; (a) Return loss,  $S_{11}$  and (b) Insertion loss,  $S_{21}$ .

### 3.4 Summary

The CPW transmission line is designed, fabricated and experimented using a high resistive silicon substrate. The study shows that material properties play an important role in the performance of the CPW transmission line. Different metal thickness is analyzed for better insertion loss performance. Even though copper is found to be slightly better than gold in terms of performance, gold is still preferred and used in the practical implementation because of its low oxidation and high reliability. High resistivity (HR) silicon substrate is used for better RF performance. The insertion loss at 5 GHz for HR silicon and LR silicon is 0.3 dB and 8.5 dB, respectively. Similarly, the insertion loss at 15 GHz for HR silicon and LR silicon is 0.7 dB and 10 dB, respectively. The measurement results for gold shows an insertion loss of 0.17 dB at 5 GHz and 0.2 dB at 15 GHz.

A capacitive shunt switch is designed and fabricated. The electrical modeling and the mechanical design of a MEMS switch are studied extensively. The switch was fabricated using a surface micromachining process. A planarization method that improves the isolation of the capacitive shunt switch is reported. The planarization of uneven surfaces of sacrificial layer is obtained by filling the CPW slots with photoresist. The measurement results show that when the proposed planarization fabrication process is implemented, the contact area between the bridge and the dielectric layer is increased by 63%, and the isolation of the switch is improved by 2.2 dB at 15 GHz ( approximately 29.3% ) and 10 dB at 40 GHz ( approximately 58.8% ). The insertion loss of the switch is 0.1 dB at 15 GHz.



## **CHAPTER 4**

### **MICROMACHINED TUNABLE BANDSTOP FILTERS**

The design and fabrication of the CPW transmission line and the capacitive shunt switch are discussed in Chapter 3. The design and experiments of the CPW based EBG bandstop filter and the micromachined tunable filters are discussed in this chapter.

A new CPW EBG structure based on an unloaded and a loaded design are investigated. The frequency characteristics of the EBG are demonstrated using different circuit parameters. An equivalent circuit model for the unloaded and loaded unit structures is derived based on the circuit analysis theory. A dispersion diagram is obtained for both structures using commercial software and Floquet's theorem. The electromagnetic wave behavior within a unit cell is analyzed. A bandstop filter is designed by cascading the EBG structures.

A micromachined based tunable bandstop filter with low insertion loss is designed. An equivalent circuit model of the tunable bandstop filter is derived. For the first time, MEMS capacitive bridges are incorporated in the design of the tunable bandstop filter. A MEMS surface micromachining process is used for the fabrication of the tunable filter. Finally, the measurement results are discussed in terms of flat responses of the stopband, passband and the tunable range of the filter.

4.1 Electromagnetic Bandgap (EBG) bandstop filter

4.1.1 Unloaded EBG structure

An unloaded lattice shape unit EBG structure is shown in Fig. 4-1. The substrate is high resistivity silicon ( $\rho = 4000 \text{ } \Omega \times \text{cm}$ ) with dielectric permittivity of  $\epsilon_r = 11.9$  and thickness of  $H = 200 \text{ } \mu\text{m}$ . The EBG structure is designed for  $50 \text{ } \Omega$  in a CPW configuration using a signal line with width of  $W = 108 \text{ } \mu\text{m}$  and a gap width of  $G = 60 \text{ } \mu\text{m}$ .

In the unloaded unit EBG structure, a square slot is etched in the ground plane with a side length  $a$ . The square etched slot is connected to the gap by a narrow transverse slot with length of  $w_s$  and width of  $d_s$ . The center cut-off frequency, which is the resonant frequency, depends on the transverse slot and the square etched hole in the ground plane.

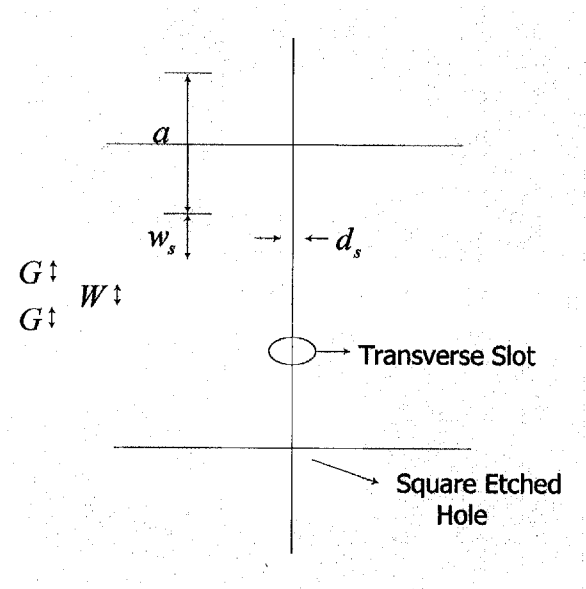


Fig. 4-1 Schematic of unloaded unit EBG structure.

---

## Chapter 4 Micromachined Tunable Bandstop Filters

---

To investigate the influences of these parameters on the frequency characteristics, two separate designs are constructed. The frequency characteristic for the proposed unit EBG structure is studied and analyzed using Agilent's Momentum (an EM simulation tool based on method of moment) and an equivalent circuit model.

### 4.1.1.1 Influence of the unloaded square aperture size

Three different sets of dimensions for the unloaded unit EBG structure are evaluated. The influence of the square aperture size  $a$  on its frequency characteristic is first investigated. The dimensions  $d_s = 60\mu\text{m}$  and  $w_s = 200\mu\text{m}$  are constant for all the three different square aperture size  $a = 350\mu\text{m}$ ,  $500\mu\text{m}$  and  $600\mu\text{m}$ . From the simulation results of Fig. 4-2, the resonant frequency of the EBG cell decreases when the etched area of the square aperture increases. This frequency characteristic can also be explained using the parallel resonant circuit. As the size of the square aperture increases, the inductance also increases, whereas,  $d_s$  and  $w_s$  are responsible for the capacitance. Since  $d_s$  and  $w_s$  are the same for all the three cases, the capacitance does not vary much compared to the inductance. Thus, as  $a$  increases, the inductance increases and in turn reduces the resonance frequency of the equivalent parallel circuit and vice versa.

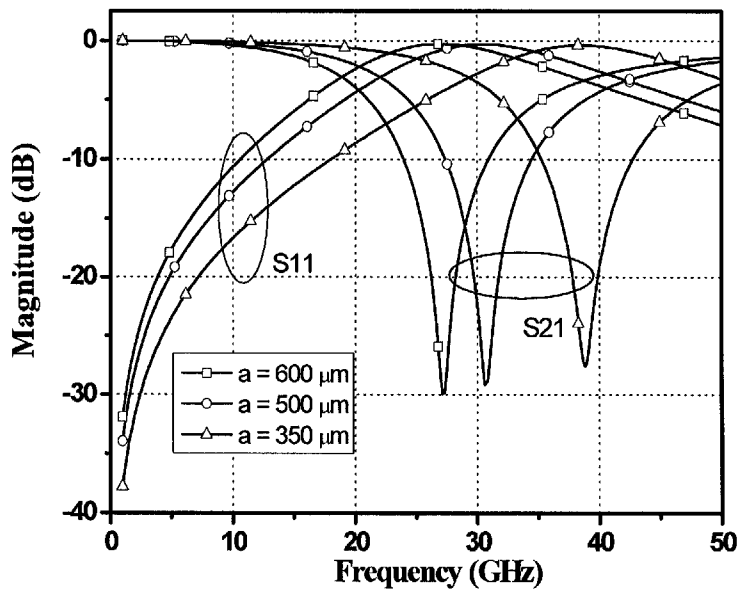


Fig. 4-2 Simulated S-parameters of the unloaded unit EBG structure versus variation of square aperture size  $a$ .

4.1.1.2 Influence of the transverse slot width

The influence of the transverse slot width  $d_s$  is investigated in this section. The square aperture size,  $a$  is kept constant at  $500\text{ }\mu\text{m} \times 500\text{ }\mu\text{m}$ , and the length of the transverse slot  $w_s$  is fixed at  $200\text{ }\mu\text{m}$ . The width of the transverse slot is allowed to vary and set at  $10\text{ }\mu\text{m}$ ,  $60\text{ }\mu\text{m}$  and  $200\text{ }\mu\text{m}$  respectively. From Fig. 4-3, it can be observed that the resonant frequency shifts from  $25.48\text{ GHz}$  to  $37.98\text{ GHz}$  when  $d_s$  changes from  $10\text{ }\mu\text{m}$  to  $200\text{ }\mu\text{m}$ . Since the size of the unloaded square aperture is fixed for all the three cases, the inductance variation is smaller. Thus, as  $d_s$  increases, the parallel capacitance decreases and the resonance frequency of the equivalent parallel circuit increases and vice versa.

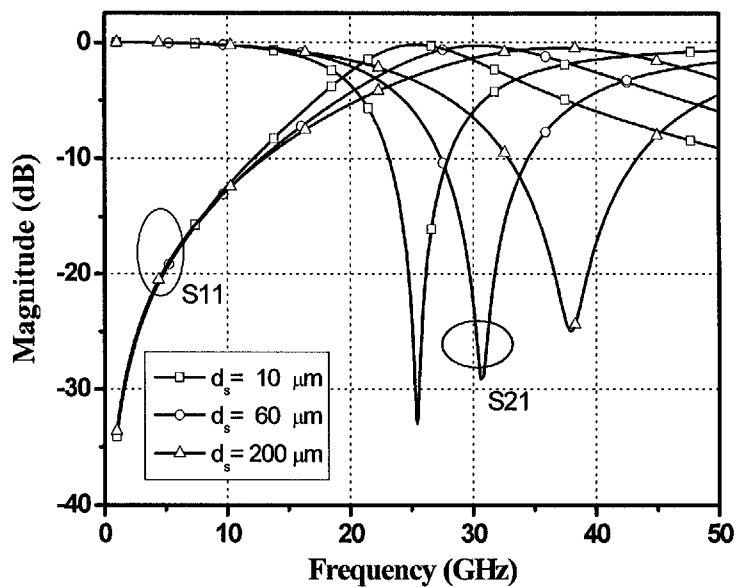


Fig. 4-3 Simulated S-parameter of the unloaded unit EBG structure versus variation of the transverse slot width  $d_s$ .

4.1.1.3 Influence of the transverse slot length

The effect of the transverse slot length  $w_s$  on the frequency characteristic is discussed. The parameters  $d_s = 60\mu m$  and  $w_s = 200\mu m$  are kept constant, but the transverse slot length  $w_s$  is allowed to change from 200, 400 and 600  $\mu m$ . The simulation results show that the frequency shifts from 30 GHz to 20 GHz, as shown in Fig. 4-4. By increasing the length of the transverse slot, the frequency response is shifted to a lower frequency.

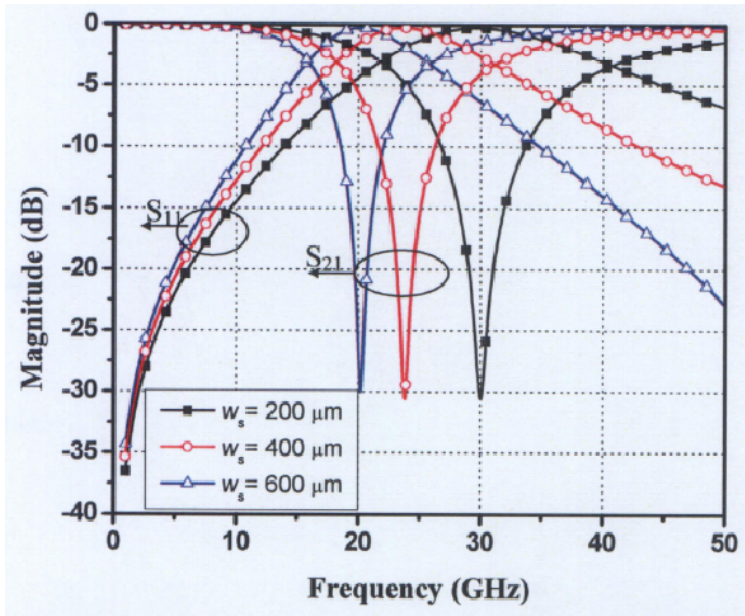


Fig. 4-4 Simulated S-parameter of the unloaded unit EBG structure versus variation of the transverse slot length  $w_s$ .

4.1.1.4 Modeling of the unloaded EBG

An equivalent parallel  $LC$  circuit is used to model the unloaded unit EBG structure as shown in Fig. 4-5. It consists of a series inductor and a parallel capacitor. From RF design point of view, the unloaded unit EBG structure can replace the parallel  $LC$  resonant circuits in many applications as it shows bandstop characteristic design [13]. To apply the unloaded EBG cell to the practical circuit, it is necessary to extract the equivalent circuit parameters, which can be obtained from the simulation results of the unloaded unit EBG structure. The lumped capacitance  $C$  is mainly contributed by the transverse slot of the ground, while the inductance  $L$  is related to the magnetic flux passing through the apertures of the ground.

Chapter 4 Micromachined Tunable Bandstop Filters

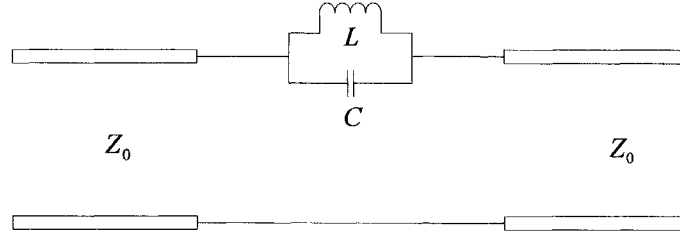


Fig. 4-5 Equivalent parallel resonant circuit for the unloaded unit EBG structure.

The equivalent impedance equation of the single resonant model can be expressed as,

$$Z = \left( j\omega C + \frac{1}{j\omega L} \right)^{-1} \quad (4-1)$$

The resonant frequency of the parallel circuit is defined as,

$$\omega_0 = \frac{1}{\sqrt{LC}} \quad (4-2)$$

The 3 dB cut-off angular frequency,  $\omega_c$  can be determined by,

$$|S_{21}|_{\omega=\omega_c} = \left| \frac{2Z_0}{2Z_0 + Z} \right| = \frac{1}{\sqrt{2}} \quad (4-3a)$$

Substituting Eq.(4-1) into Eq.(4-3a), it can be further expressed as,

$$|S_{21}|_{\omega=\omega_c} = \frac{2Z_0}{\sqrt{4Z_0^2 + \left( \frac{1}{\omega_c C - 1/\omega_c L} \right)^2}} = \frac{1}{\sqrt{2}} \quad (4-3b)$$

Substituting Eq.(4-2) into Eq.(4-3b), the capacitance can be obtained as,

$$C = \frac{\omega_c}{2Z_0(\omega_0^2 - \omega_c^2)} \quad (4-4)$$

Chapter 4 Micromachined Tunable Bandstop Filters

The inductance can be determined by,

$$L = \frac{1}{\omega_0^2 C} \tag{4-5}$$

where  $a$ ,  $w_s$  and  $d_s$  (see Fig. 4-1) are chosen so that  $a = 350 \mu\text{m}$ ,  $w_s = 200 \mu\text{m}$  and  $d_s = 60 \mu\text{m}$  to provide an example to the parameter extraction procedure.

Table 4-1 Extracted equivalent circuit parameters for the unloaded unit EBG structure, with different square aperture size  $a$ .

Square aperture size, $a$ ( $\mu\text{m}$ )	$d_s = 60 \mu\text{m}$ , $w_s = 200 \mu\text{m}$		
	350	500	600
Resonant Frequency (GHz)	38.79	30.6	27.13
3dB Cut-off Frequency (GHz)	29.12	21.92	18.78
Inductance (nH)	0.229	0.342	0.434
Capacitance (pF)	0.073	0.079	0.079

The parameters of the equivalent circuit are extracted and presented in Table 4-1. The circuit simulation results are obtained using the equivalent circuit parameters as shown in Fig. 4-6. These are compared with the EM simulation results. The equivalent circuit simulation results are in good agreement with the EM simulation results. Thus, the derived equivalent circuit and the extracted parameters for the unloaded EBG structure can be accurately adapted to design the practical circuits as well as to analyze the dimensions of any proposed structures.



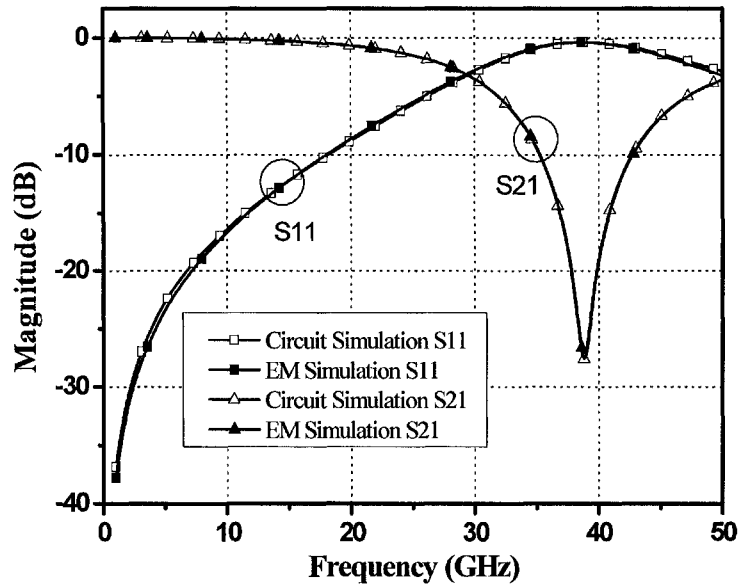


Fig. 4-6 Comparison on parameter extraction and EM simulation results of the unloaded unit EBG structure.

The resonant frequency of the proposed unit EBG is affected by the variation of the unloaded square aperture dimensions. Based on the tabulated results (see Table 4-1) and the simulated results (see Fig. 4-2), it can be deduced that by varying from  $a = 350\mu\text{m}$  to  $600\mu\text{m}$ , the change in capacitances is merely 15%. This is different from the case of inductance variation, where a variation as large as 178% is observed. The inductance variation rate is nearly 10 times greater than that of the capacitance. These observations prove that the dimension of the transverse slot is responsible for the parallel capacitor and the size of the square aperture relates directly to the series inductor. The series inductance is significantly affected by the size of the square aperture.

For the second design, only the width of the transverse slot  $d_s$  is allowed to vary.

Table 4-2 presents the extracted equivalent circuit parameters.

Chapter 4 Micromachined Tunable Bandstop Filters

Table 4-2 Extracted equivalent circuit parameters of the unloaded EBG unit structure with variation of the transverse slot width  $d_s$ .

$w_s = 200 \text{ } \mu\text{m} , a = 500 \text{ } \mu\text{m}$			
Transverse slot width, $d_s \text{ (} \mu\text{m) }$	10	60	200
Resonant Frequency (GHz)	25.48	30.6	37.98
3 dB cut-off Frequency (GHz)	19.38	21.92	24.56
Inductance (nH)	0.339	0.342	0.357
Capacitance (pF)	0.115	0.079	0.049

The simulation result is shown in Fig. 4-3. From the case of  $d_s = 10 \text{ } \mu\text{m}$  to the case of  $d_s = 200 \text{ } \mu\text{m}$ , the inductance varies by 5%, whereas the capacitance changes by almost 57%. The capacitance variation rate is nearly 10 times greater than that of the inductance. This again verifies that the dimension of the transverse slot controls the capacitance and the size of the square aperture affects the inductance of the equivalent circuit. Since the width of the transverse slot  $d_s$  is varied, the parallel capacitance also changes accordingly.

4.1.1.5 Propagation characteristics of the unloaded unit EBG

The unloaded EBG cells are cascaded to form a bandstop filter as shown in Fig. 4-8. The propagation characteristic on the unloaded EBG is analyzed using Floquet’s theorem [132]. By simply considering the unit structure, the EM simulation can be used to obtain the dispersion diagram of the proposed unloaded EBG structure. The

Chapter 4 Micromachined Tunable Bandstop Filters

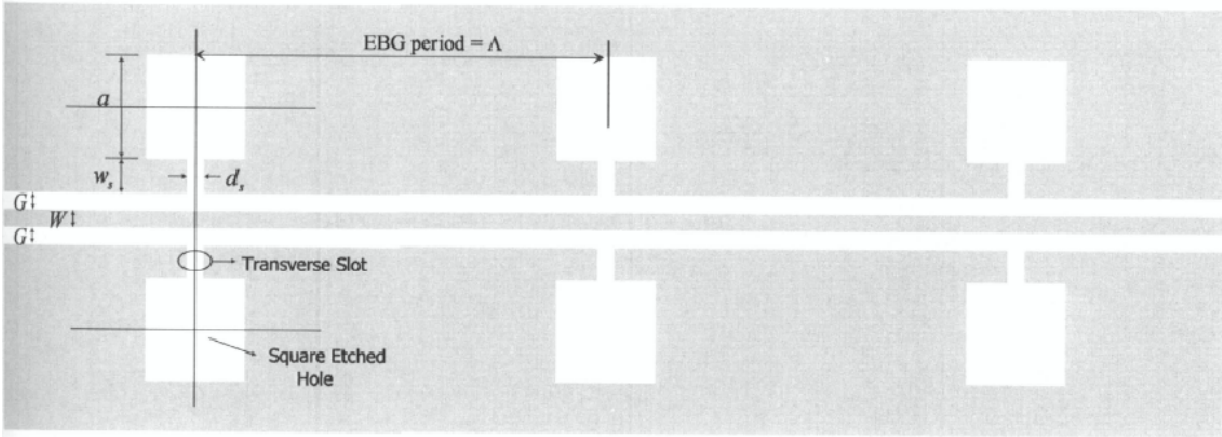


Fig. 4-7 Schematic of unloaded EBG bandstop filter.

propagation factor in this case is  $e^{-\gamma\Lambda}$ , where  $\Lambda = 2020\mu\text{m}$  is the period of the EBG structure, and  $\gamma = \alpha + j\beta$  is the complex propagation constant in the direction of propagation that can be expressed as,

$$\gamma = \frac{1}{\Lambda} \cosh^{-1} \left( \frac{\left[ (1 + S_{11})(1 - S_{22}) + S_{12}S_{21} + \left( \frac{Z_{01}}{Z_{02}} \right) (1 - S_{11})(1 + S_{22}) + S_{12}S_{21} \right]}{4S_{21}} \right) \quad (4-6)$$

where  $Z_{01}$  and  $Z_{02}$  are the impedance of port 1 and port 2 which is  $50\Omega$  in the design.

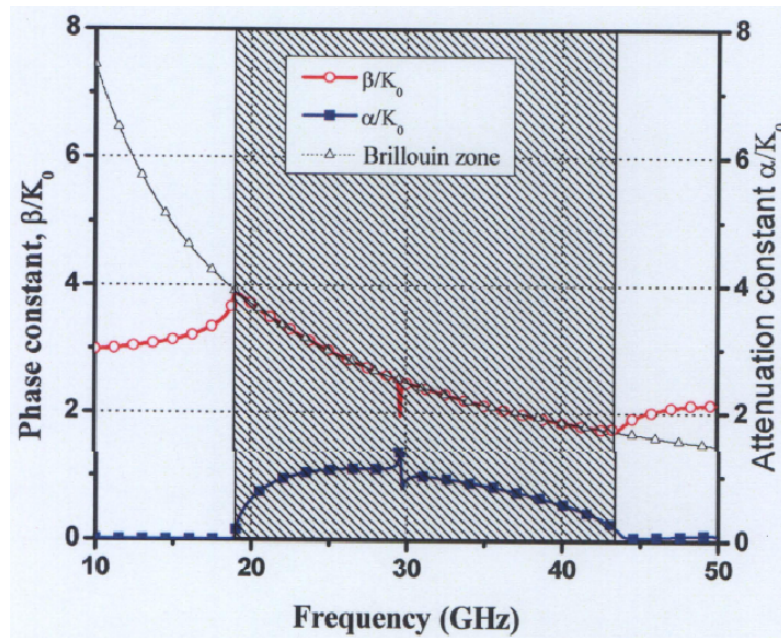


Fig. 4-8 Simulated dispersion diagram of unloaded EBG structure with  $d_s = 60 \mu\text{m}$  and  $a = 500 \mu\text{m}$ .

The scattering matrix of the  $m^{\text{th}}$  mode propagating in the  $z$  direction is calculated using full wave simulator Zeland IE-3D [132]. The normalized phase constant  $\beta/k_0$  and the attenuation constant  $\alpha/k_0$  of a single EBG cell are illustrated in Fig. 4-8. When  $\beta/k_0$  is close to the Bragg condition ( $\beta \Lambda = \pi$ ), the signal is strongly attenuated. The stopband is very wide and the propagation of any signal with frequency inside it is prohibited. It can also be seen from Fig. 4-8 that considerable rejection is expected in the stop band, when the number of cells are increased. There is a significant rise in the loss factor in the stopband due to radiation. Simulation results of a higher frequency range (i.e. larger than 43 GHz) are unfavorable compared to those of a lower frequency range (i.e. less than 18 GHz).

#### Chapter 4 Micromachined Tunable Bandstop Filters

---

The complex characteristics impedance,  $Z_c = \text{Re}(Z_c) + j \text{Im}(Z_c)$  can be explicitly calculated in terms of the ABCD-matrix with the elements A, B, C, and D are,

$$Z_c = \sqrt{\frac{B}{C}} \quad (4-7)$$

when the ABCD matrix are converted to S-parameters, the complex characteristic impedance can be expressed as,

$$Z_c = Z_0 \sqrt{\frac{(1 + S_{11})(1 + S_{22}) - S_{12}S_{21}}{(1 - S_{11})(1 - S_{22}) - S_{12}S_{21}}} \quad (4-8)$$

where  $Z_0$  is the characteristic impedance which is 50 ohms. At the low frequency range,  $\text{Re}(Z_c)$  starts to rise slowly from 72 ohms in an exponential way, while  $\text{Im}(Z_c)$  is kept to zero. When the frequency increases, the bandstop occurs,  $\text{Re}(Z_c)$  and  $\text{Im}(Z_c)$  become infinite as shown in Fig. 4-9. For the uniform CPW characteristic, the impedance is 48 ohms throughout the frequency range.

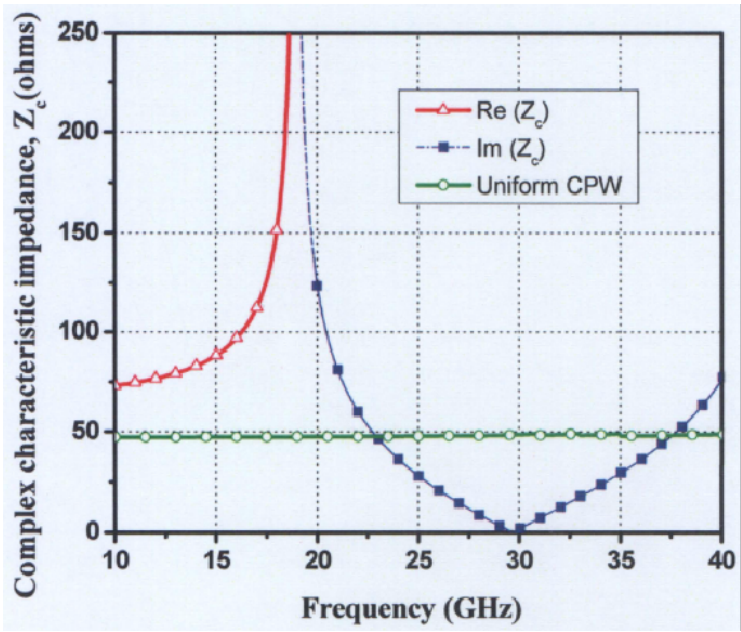


Fig. 4-9 Simulation results of complex characteristics impedance of the unloaded unit EBG structure.

4.1.2 Loaded EBG structure

In this section, the loaded unit EBG structure is shown in Fig. 4-10. A ring slot is etched in the ground plane with side length  $a$  and ring width  $r_s$ . The ring slot is connected to the gap by a narrow transverse slot with length  $w_s$  and width  $d_s$ . In addition, a square etched hole with side length  $b$  is etched in the center of the ring slot. Compared to the EBG structure without a center etched hole (i.e. unloaded), the proposed EBG structure includes a ring slot and a square etched hole and hence, is named as loaded EBG structure.

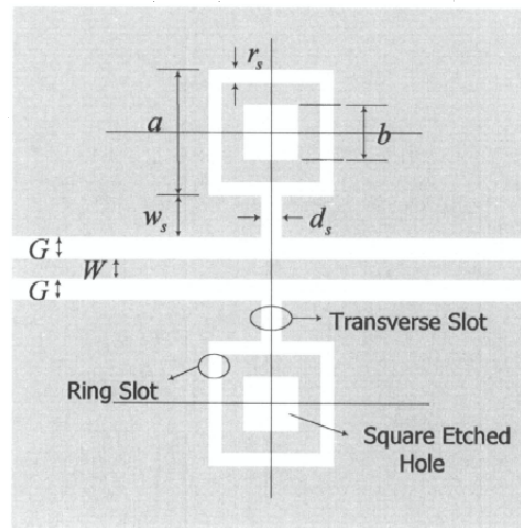


Fig. 4-10 Schematic of loaded unit EBG structure.

When the side length of the square etched hole and the ring slot side length are equal (i.e. at  $b = a$ ), the square etched hole and the ring slot merge to form a square aperture and then the unit cell becomes the unloaded EBG structure as mentioned in the previous section. In the next section, the effect of the dimensions of the square etched hole (i.e. side length  $b$ ) on the frequency characteristic, the equivalent circuit model and the dispersion diagram of the loaded EBG are discussed.

#### 4.1.2.1 Effect of the square etched hole – Loaded EBG structure

In this section, four different sets of dimensions are designed. The square aperture size  $a$  is  $500\mu\text{m} \times 500\mu\text{m}$  and the dimension of transverse slot is maintained at  $d_s = 60\mu\text{m}$  and  $w = 220\mu\text{m}$  for all the four different designs. A center etched square hole is added in the area of the unloaded square aperture (see Fig. 4-10). While the width of the ring slot  $r_s$  is chosen at  $30\mu\text{m}$  for all the four cases, the length of the square etched hole,



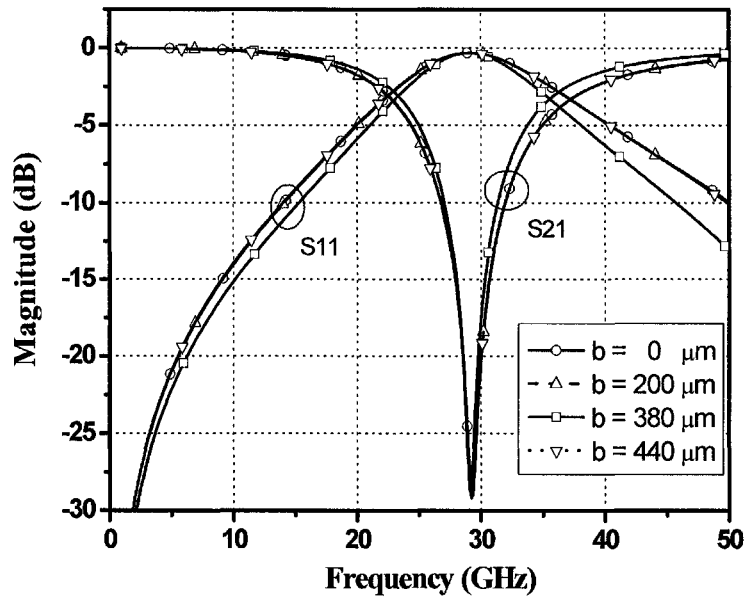


Fig. 4-11 Simulated S-parameters of the loaded unit EBG structure, versus different center slot within the ring  $b$ .

$b$  is set at  $0\text{ }\mu\text{m}$ ,  $200\text{ }\mu\text{m}$ ,  $380\text{ }\mu\text{m}$  and  $440\text{ }\mu\text{m}$  respectively. Based on the simulation results as shown in Fig. 4-10, all the three cases with  $b = 0\text{ }\mu\text{m}$ ,  $200\text{ }\mu\text{m}$  and  $440\text{ }\mu\text{m}$  exhibit similar behavior except for the case of  $b = 380\text{ }\mu\text{m}$ . The resonant frequencies for all the four cases are almost identical, but the frequency response begins to drift after the resonant frequency. The loaded structures in the square aperture area are the main contributor to such a variation. It is widely known that low insertion loss and high return loss are expected in the passband of the bandstop filter. An optimum width of the square etched hole (i.e. at  $b = 380\text{ }\mu\text{m}$ ) can clearly be deduced from Fig. 4-11 where the return loss is the highest and the insertion loss is the lowest among all the four different designs.

The existence of the loaded structure in the square aperture perturbs the whole circuit, which implies that the transverse slot is no longer the only factor contributing to



---

## Chapter 4 Micromachined Tunable Bandstop Filters

---

the equivalent capacitor. Likewise, the square aperture can no longer act as the main determining factor to the equivalent inductor. Therefore, the additional structure in the square aperture area can significantly improve the passband insertion loss as well as the return loss. Single resonant equivalent circuit is no longer effective to model such a loaded structure.

### 4.1.2.2 Modeling of the loaded EBG structure

In the previous section, the single resonant parallel  $LC$  circuit model is employed to model the unloaded unit EBG structure. In the case of the loaded EBG cell, such a model would not be accurate. When the single resonant circuit model is used as shown in Fig. 4-12, the simulation results for the insertion and return losses cannot match with the EM simulation results especially, when the frequency becomes greater than the resonant frequency.

As a result, the loaded EBG cell has to be modeled using a different circuit. By cascading two parallel resonant circuits, the loaded unit EBG structure can be represented in Fig. 4-13.

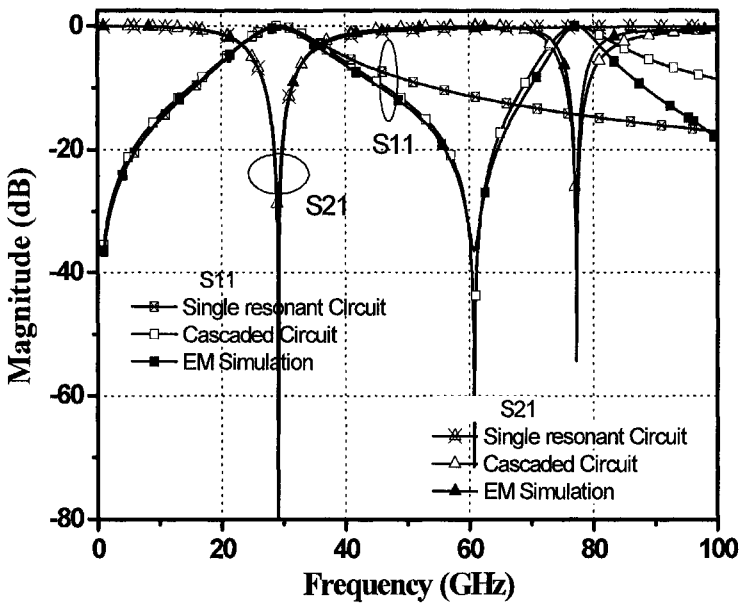


Fig. 4-12 Comparison on parameter extraction and EM simulation results of the loaded unit EBG structure.

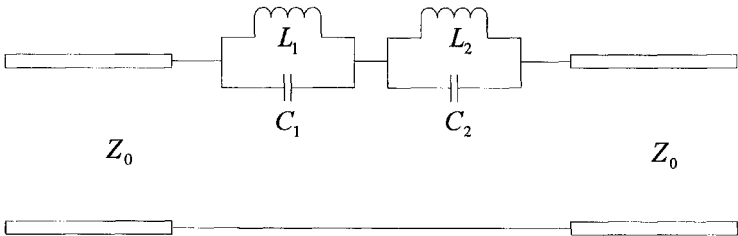


Fig. 4-13 Equivalent circuit for a unit cell of the cascaded parallel resonant EBG structure.

The equivalent impedance of the cascaded parallel resonant circuits can be expressed as,

$$Z = \left( j\omega C_1 + \frac{1}{j\omega L_1} \right)^{-1} + \left( j\omega C_2 + \frac{1}{j\omega L_2} \right)^{-1} \tag{4-9}$$

where the sub-script “1” and “2” denote the two different resonant circuits.

## Chapter 4 Micromachined Tunable Bandstop Filters

The reflection coefficient,  $S_{11}$  is defined as,

$$|S_{11}| = \left| \frac{Z}{2Z_0 + Z} \right| = \frac{\left| \frac{1}{\omega C_1 - 1/\omega L_1} + \frac{1}{\omega C_2 - 1/\omega L_2} \right|}{\sqrt{4Z_0^2 + \left( \frac{1}{\omega C_1 - 1/\omega L_1} + \frac{1}{\omega C_2 - 1/\omega L_2} \right)^2}} \quad (4-10)$$

The maximum value of  $|S_{11}|$  can be obtained by differentiating it with respect to the angular frequency,  $\omega$  and the two roots obtained are,

$$\omega_1 = (L_1 C_1)^{-\frac{1}{2}}, \quad \omega_2 = (L_2 C_2)^{-\frac{1}{2}} \quad (4-11)$$

The insertion loss is given by,

$$|S_{21}| = \left| \frac{2Z_0}{2Z_0 + Z} \right| = \frac{2Z_0}{\sqrt{4Z_0^2 + \left( \frac{1}{\omega C_1 - 1/\omega L_1} + \frac{1}{\omega C_2 - 1/\omega L_2} \right)^2}} \quad (4-12)$$

By differentiating  $S_{21}$ , the first notch angular frequency,  $\omega_n$  can be obtained as,

$$\omega_n = \frac{\sqrt{L_1 + L_2}}{\sqrt{L_1/\omega_2^2 + L_2/\omega_1^2}} \quad (4-13)$$

The 3 dB cut-off angular frequency,  $\omega_c$  can be determined as,

$$|S_{21}|_{\omega=\omega_c} = \frac{2Z_0}{\sqrt{4Z_0^2 + \left( \frac{1}{\omega_c C_1 - 1/\omega_c L_1} + \frac{1}{\omega_c C_2 - 1/\omega_c L_2} \right)^2}} = \frac{1}{\sqrt{2}} \quad (4-14)$$

From Eqs. (4-11), (4-13) and Eq. (4-14), the equivalent circuit parameters can be extracted, whereby,

$$L_1 = \frac{2Z_0 (\omega_n^2 - \omega_1^2)(\omega_1^2 - \omega_c^2)(\omega_2^2 - \omega_c^2)}{\omega_c \omega_1^2 (\omega_2^2 - \omega_1^2)(\omega_n^2 - \omega_c^2)} \quad (4-15)$$

and

## Chapter 4 Micromachined Tunable Bandstop Filters

$$L_2 = \frac{2Z_0(\omega_2^2 - \omega_n^2)(\omega_1^2 - \omega_c^2)(\omega_2^2 - \omega_c^2)}{\omega_c \omega_2^2(\omega_2^2 - \omega_1^2)(\omega_n^2 - \omega_c^2)} \quad (4-16)$$

The capacitance values can be obtained as,

$$C_1 = 1/\omega_1^2 L_1, \quad C_2 = 1/\omega_2^2 L_2 \quad (4-17)$$

All the four parameters  $L_1$ ,  $L_2$ ,  $C_1$  and  $C_2$  can be calculated using Eqs. (4-15), (4-16) and (4-17), respectively.

To illustrate the parameter extraction procedure, the values of  $a$ ,  $r_s$ ,  $w_s$ ,  $d_s$  and  $b$  are selected as 500, 30, 220, 60 and 380  $\mu\text{m}$  respectively. The parameters for both the single resonant circuit model and the cascaded circuit model are extracted and summarized in Table 4-3.

Table 4-3 Extracted equivalent circuit parameters for the loaded EBG unit structure.

		$d_s = 60 \mu\text{m}$ , $w_s = 220 \mu\text{m}$ , $a = 500$ $\mu\text{m}$ , $r_s = 30 \mu\text{m}$			
Square etched hole, $b$ ( $\mu\text{m}$ )		0	200	380	440
First resonant frequency (GHz)		29.24	29.24	29.24	29.19
First 3dB cut-off frequency (GHz)		22.42	22.42	23.20	22.34
Second resonant frequency (GHz)		81.77	81.42	77.26	77.77
First notch frequency (GHz)		66.67	66.67	60.76	65.13
Single resonant model	$L$ (nH)	0.285	0.285	0.243	0.286
	$C$ (pF)	0.104	0.104	0.123	0.103
Cascaded model	$L_1$ (nH)	0.282	0.282	0.243	0.285
	$C_1$ (pF)	0.105	0.105	0.122	0.104
	$L_2$ (nH)	0.023	0.022	0.028	0.021
	$C_2$ (pF)	0.168	0.172	0.152	0.195

#### Chapter 4 Micromachined Tunable Bandstop Filters

---

In order to determine the suitability of the two models for the loaded EBG structure, simulation results of the single resonant and cascaded models are shown in Fig. 4-12. The cascaded circuit simulation results are in good agreement with the EM simulation results at frequency which is below the notch frequency (i.e. at 60.76 GHz). However, the simulation results for the single resonant circuit model drifts always from the EM simulation results after 40 GHz. Therefore, for the loaded EBG structure, the cascaded circuit model is more appropriate than the single resonant circuit model, and is valid up to the first notch frequency. The extracted equivalent circuit parameters are simulated in Fig. 4-12 and the parameters for the single and the cascaded resonant model are listed in Table 4-3. For frequencies below the first notch frequency, the resonant circuit of Fig. 4-13 with the parameters  $L_1$  and  $C_1$  are dominated and compared with the parameters  $L_2$  and  $C_2$ .

For the design of parameters  $L_1$  and  $C_1$ , the resonant frequency of the proposed circuit does not vary with the change in size of the loaded square etched hole varies. The extracted parameters for the three cases of  $b$  variations, i.e.  $b = 0\mu\text{m}$ ,  $200\mu\text{m}$  and  $440\mu\text{m}$  are almost the same. However, a significant difference is noted for the case when  $b = 380\mu\text{m}$ . The capacitance  $C_1$  is increased by 18 % while the inductance  $L_1$  is decreased by 15% with the same resonant frequency. The increase in capacitance and the decrease in inductance imply that the greater the amount of signals pass through the circuit for both higher and lower frequencies, the lesser the amount of signals get reflected.

This characteristic is desirable in the passband design for the bandstop filters. From both the EM simulation results and the equivalent circuit extraction parameters, the

Chapter 4 Micromachined Tunable Bandstop Filters

optimum value of the square etched hole width is that value among all the valid width values for the unit EBG at which the passband performance is the optimum and, for this case, this optimum value is  $b = 380 \mu\text{m}$ .

4.1.2.3 Propagation characteristics of the loaded unit EBG

The loaded badnstop filter is designed by cascading the loaded EBG cells as shown in Fig. 4-14. The dispersion diagram for the loaded EBG periodic structures, which is also known as Brillouin diagram, is useful in analyzing the guided and leaky wave characteristics of the structures. The period of the loaded structure is the same as that of the unloaded EBG. The shaded region from 18 GHz to 42 GHz shows that the electromagnetic wave is prohibited in the periodic structures as shown in Fig. 4-15. There exists a spurious peak in the phase constant curve obtained through the EM simulation and can be overcome by increasing the mesh resolution. The bandgap region of the loaded EBG is smaller compared to that obtained for the unloaded EBG. The complex characteristics impedance of the loaded structure is shown in Fig. 4-16.

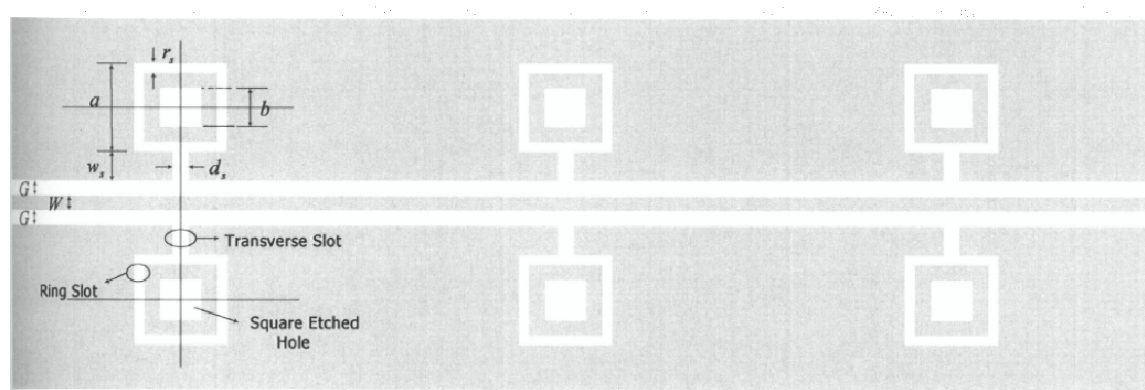


Fig. 4-14 Schematic of loaded EBG bandstop filter.

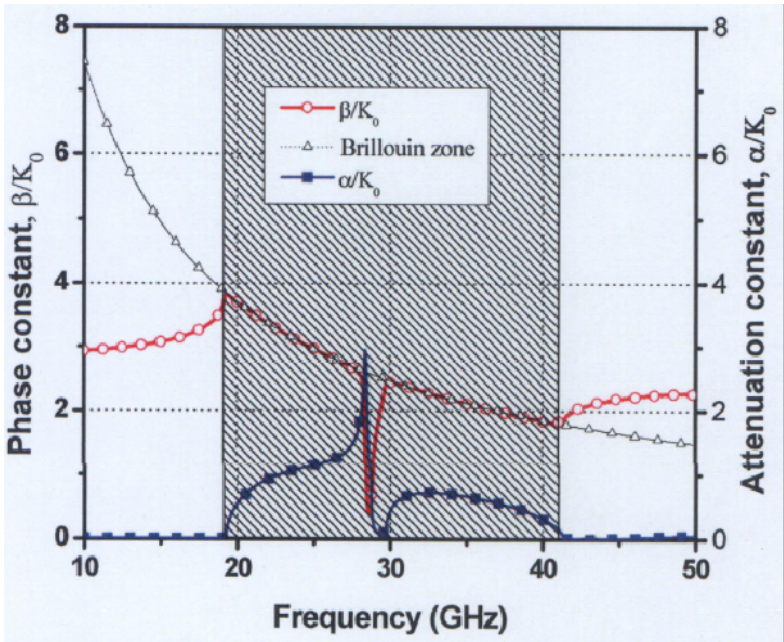


Fig. 4-15 Simulated dispersion diagram of the loaded unit EBG structure.

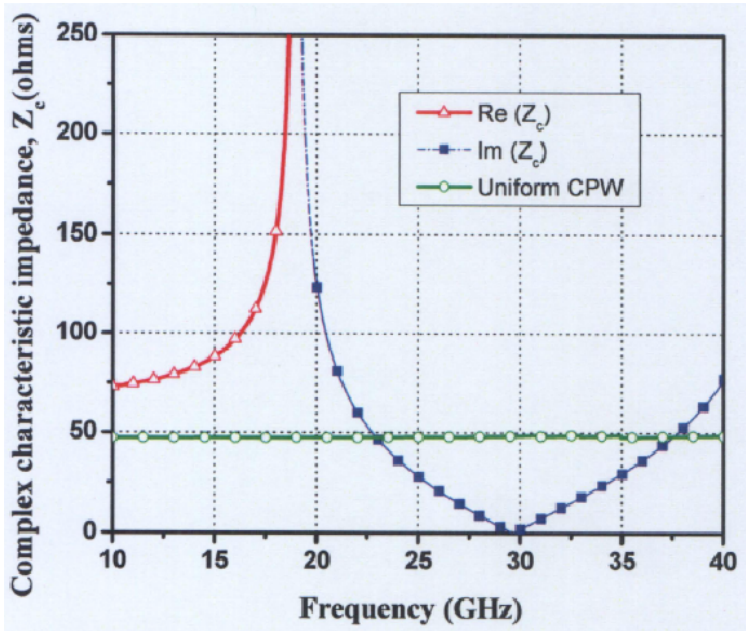


Fig. 4-16 Complex characteristics impedance of the unloaded unit EBG structure.

## Chapter 4 Micromachined Tunable Bandstop Filters

---

The response of the  $\text{Re}(Z_c)$  and  $\text{Im}(Z_c)$  impedance are almost identical with that of the unloaded structure, because it is also a periodic structure but with some geometrical differences.

### 4.1.3 Experimental results and discussions

Based on the equivalent circuit and the extracted parameters for the unit EBG structures (both unloaded and loaded), bandstop filters are designed and fabricated using the proposed EBG cell structure. The bandstop filters are fabricated using surface micromachining fabrication process. The process begins by growing a  $0.5\text{ }\mu\text{m}$  thick  $\text{SiO}_2$  layer on a  $200\text{ }\mu\text{m}$  thick high resistivity silicon substrate that serves as a buffer layer. A  $1.5\text{ }\mu\text{m}$  aluminum layer is evaporated on the buffer layer to define the structure. Photoresist coating and device patterning are performed. Finally, aluminum wet etching is performed to remove the aluminum thin film and to form the EBG structures. Only one mask is needed for the filters fabrication.

#### 4.1.3.1 Unloaded EBG bandstop filter

Figure 4-17 shows the SEM graph of the unloaded EBG filter which consists of three EBG cells structure and a CPW transmission line. The three cascaded cells structures are periodically placed apart at a distance of  $2020\text{ }\mu\text{m}$ , which is half of the guided wavelength of the CPW at 30 GHz. The design parameters of the filter  $a$ ,  $w_s$ , and  $d_s$  are presented in Table 4-2 and the measurement results is shown in 4-18.



Chapter 4 Micromachined Tunable Bandstop Filters

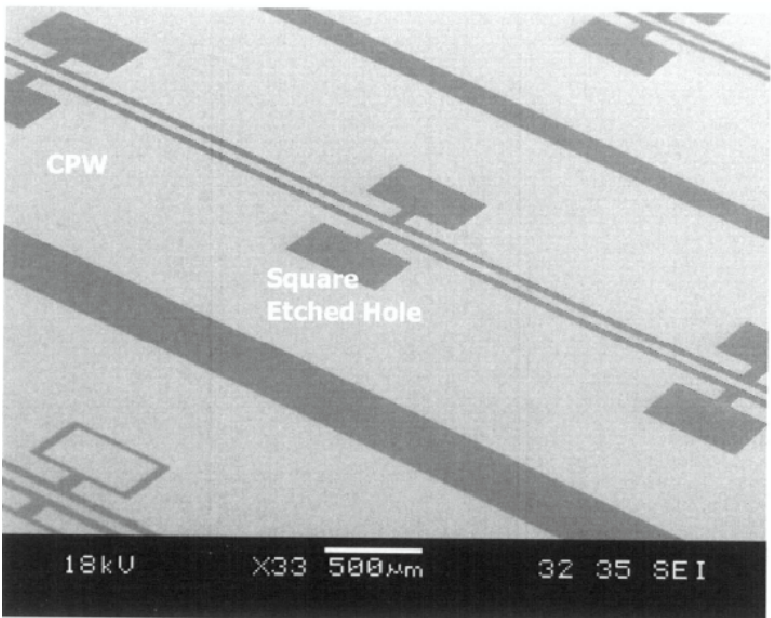


Fig. 4-17 SEM graph of the unloaded EBG bandstop filter.

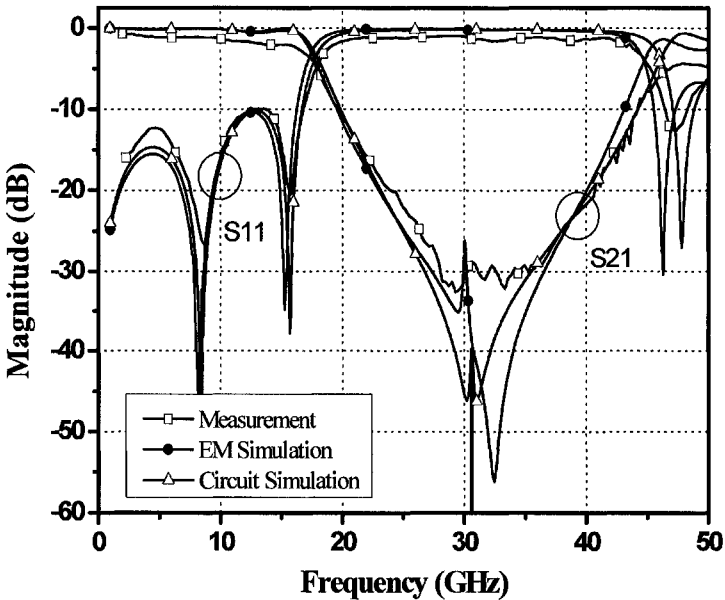


Fig. 4-18 Comparison of measurement and the simulation results (EM and circuit simulations) of the unloaded EBG bandstop filter.

Chapter 4 Micromachined Tunable Bandstop Filters

The measurement result shows that the 20 dB stopband range is from 24.4 GHz to 40.6 GHz. The stopband return loss is less than 2 dB. For the lower passband, the return loss is greater than 10 dB, for the higher passband, the return loss is 6 dB. The lower passband insertion loss is less than 2 dB and the higher passband insertion loss is below 5 dB.

4.1.3.2 Loaded EBG bandstop filter

Fig. 4-19 shows the SEM micrograph of the loaded EBG filter which consists of three loaded EBG cells structure and a CPW transmission line. The design parameters of the loaded EBG  $a$ ,  $r_s$ ,  $w_s$ ,  $d_s$  and  $b$ , are presented in Table 4-3. The measurement and simulation results of the EBG bandstop filter are compared as shown in Fig. 4-20. The simulation results and the equivalent circuit are in good agreement with the measured results, which show the validity of the proposed equivalent circuit.

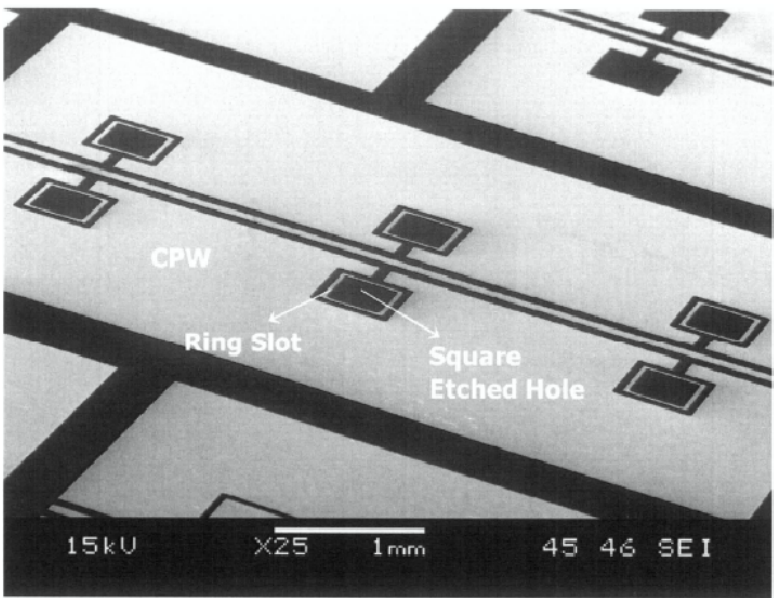


Fig. 4-19 SEM graph of the loaded EBG bandstop filter.

The measured results show a relatively wide 20 dB stopband from 24.8 GHz to 38 GHz with the return loss of less than 2 dB. For the passband, the return loss is higher than 10 dB except for those at the higher frequencies. The lower passband insertion loss is less than 2 dB and the higher passband insertion loss is less than 4.5 dB. The measurement results of the loaded and the unloaded EBG bandstop filters are compared as shown in Fig. 4-21. Except for the 20 dB stopband width, it is noted that the performances of the unloaded EBG bandstop filter are more inferior compared to the loaded EBG bandstop filter in all aspects. In particular, the higher passband performances of the loaded EBG filter are better than the unloaded EBG filter.

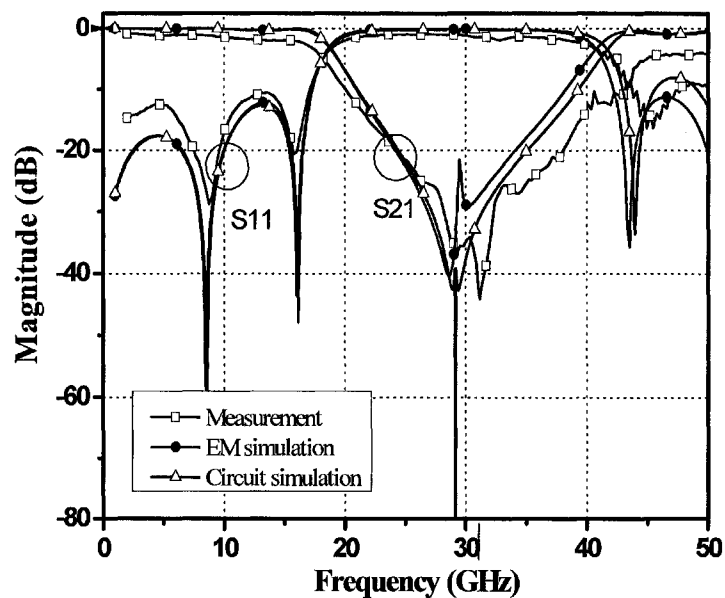


Fig. 4-20 Comparison of the measurement and simulation results of the loaded EBG bandstop filter.

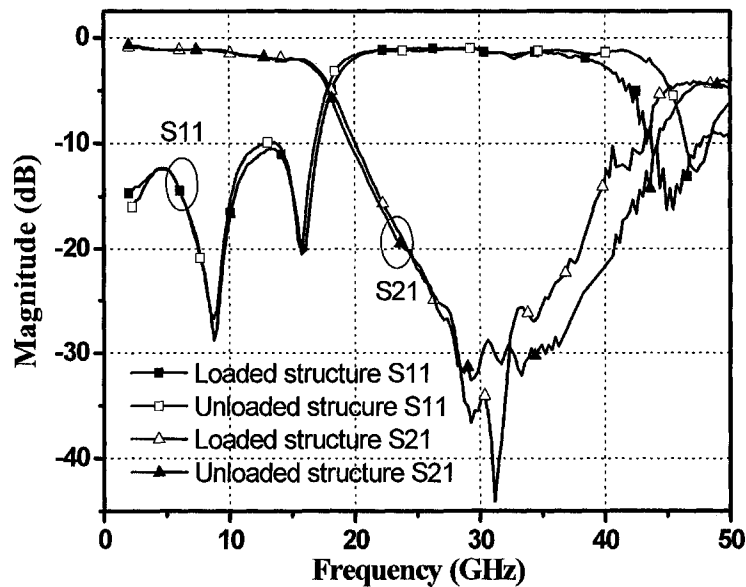


Fig. 4-21 Comparison of the measurement results of the loaded and unloaded EBG bandstop filters.

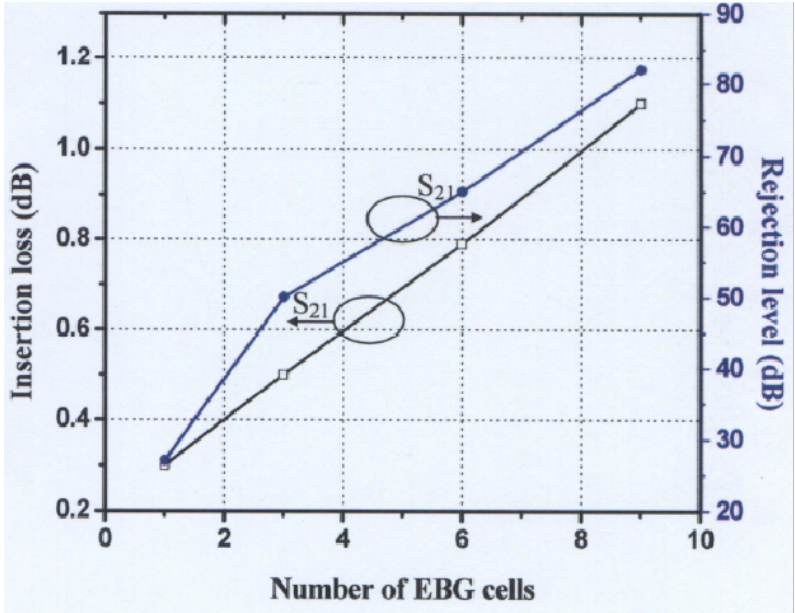
The reason for this improvement lies in the equivalent inductance of the loaded unit EBG structure, which is much lower, compared to the unloaded unit EBG structure. As for the equivalent capacitance, the loaded cell yields a higher capacitance than the unloaded cell. It is noted that both the passband insertion loss and the stopband return loss characteristics are very flat and contain less than 0.2 ripples for both filters.

## **4.2 Design of the micromachined tunable bandstop filter**

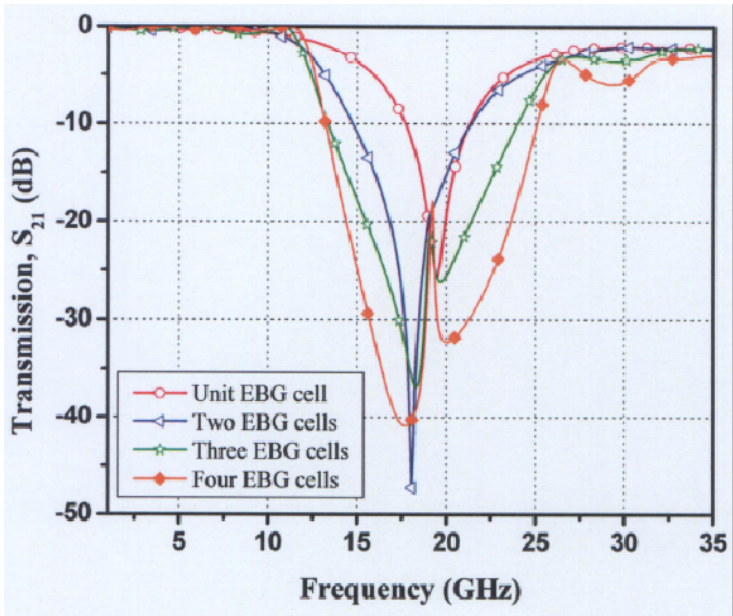
The bandstop filter consists of the cascaded unit EBG cells. The number of the cascaded EBG cells depends on three different factors such as insertion loss, rejection level and bandwidth. Figs. 4-22 (a) and (b) shows that the rejection level and the bandwidth increase with the number of the unit EBG cells, which also leads to an increase of the insertion loss because of higher conductor loss. Based on the optimum design, a bandstop filter with three unit EBG cells provides a high rejection level of 40 dB with insertion loss of 0.45 dB.

In the tunable EBG bandstop filter, the CPW transmission line has a signal strip with width of  $70\text{ }\mu\text{m}$  and a gap width of  $115\text{ }\mu\text{m}$  as shown in Fig. 4-23. The transmission line has high impedance of  $65\text{ }\Omega$ . This is because the dimension of the CPW has been designed by taking into account of the periodical loading effects of MEMS capacitive bridges. There are a total 8 micromachined bridges in each transmission line between the two EBG structures. The width and length of the bridges are  $50\text{ }\mu\text{m}$  and  $300\text{ }\mu\text{m}$  respectively [130]. The periodic spacing between the two bridges is  $s = 200\text{ }\mu\text{m}$ .

Chapter 4 Micromachined Tunable Bandstop Filters



(a)



(b)

Fig. 4-22 Simulation results of number of the unit EBG cells; (a) Insertion loss and rejection level; (b) Bandwidth variation.



Chapter 4 Micromachined Tunable Bandstop Filters

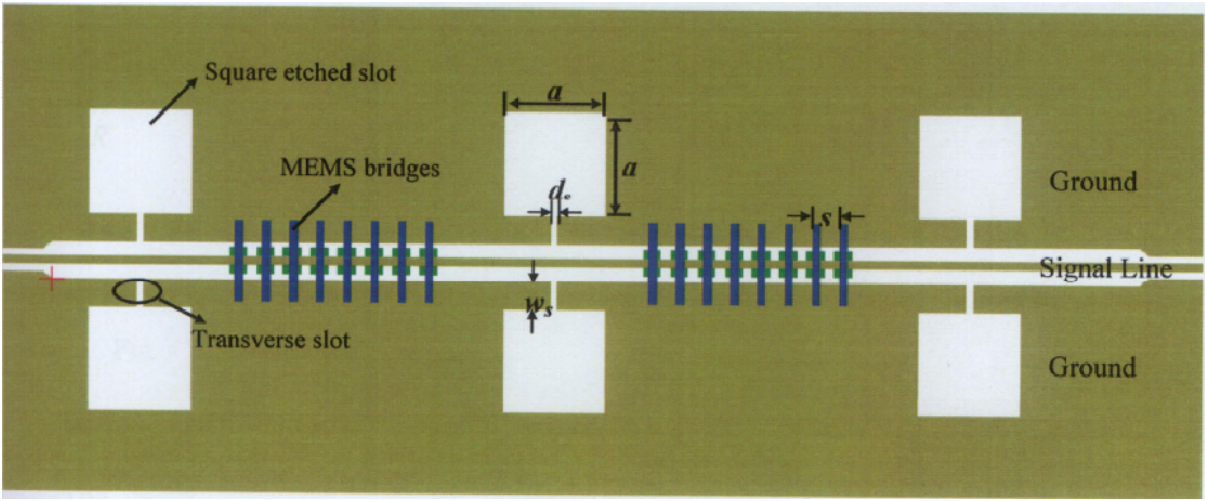


Fig. 4-23 Schematic of the tunable bandstop filter using MEMS bridges.

Each micromachined bridge acts as a tuning element because of the changing bridge height, i.e. varying the capacitance, when the DC bias voltage is applied between the signal line and the ground plane. Hence, the frequency of the band rejection can be tuned with different bias levels. An equivalent  $LC$  circuit is used to describe the tunable EBG structure as shown in Fig. 4-24. The lumped capacitance  $C_1$  is basically due to the transverse slot on the ground, while the inductance  $L_1$  is related to the magnetic flux passing through the aperture on the ground, i.e.  $a$ . Since the micromachined bridges are shunt capacitive, they can be modeled as an equivalent parallel capacitor  $C_2$  and in series with an inductor  $L_2$  in each resonator section, as shown in Fig. 4-24.

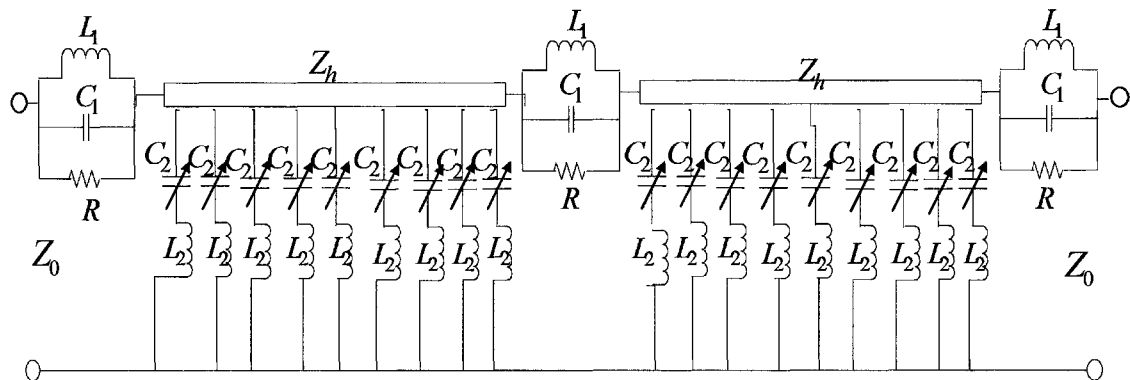


Fig. 4- 24 Equivalent parallel resonant circuit for the tunable bandstop filter.

The high impedance transmission line  $Z_h$  compensates for the decrease in impedance due to the increase in shunt capacitance, when the bridges are slowly moved down by the driven voltage. The equivalent circuit parameters are summarized in Table 4-4. These parameters are numerically extracted from the circuit simulation results of the EBG structure using Agilents ADS software.

Table 4-4 Extracted equivalent circuit parameters of the tunable EBG structure

Variable capacitance $C_2$ (pF)	0.015	0.017	0.022	0.025
Resonant Frequency (GHz)	19.10	18.70	17.6	17.4
Inductance $L_1$ (nH)	0.49	0.49	0.49	0.49
Fixed Capacitance $C_1$ (pF)	0.13	0.13	0.13	0.13
Resistance ( $K \Omega$ )	1.80	1.82	1.85	1.86

Current distribution for this structure is obtained using IE-3D software. It is noted that the transmission power cannot pass through the circuit and maximally attenuated at the bandstop frequency of 19 GHz as shown in Fig. 4-25. The current distribution on the



Chapter 4 Micromachined Tunable Bandstop Filters

micromachined bridges also shows the same phenomena of negligible current flowing on the micromachined bridges.

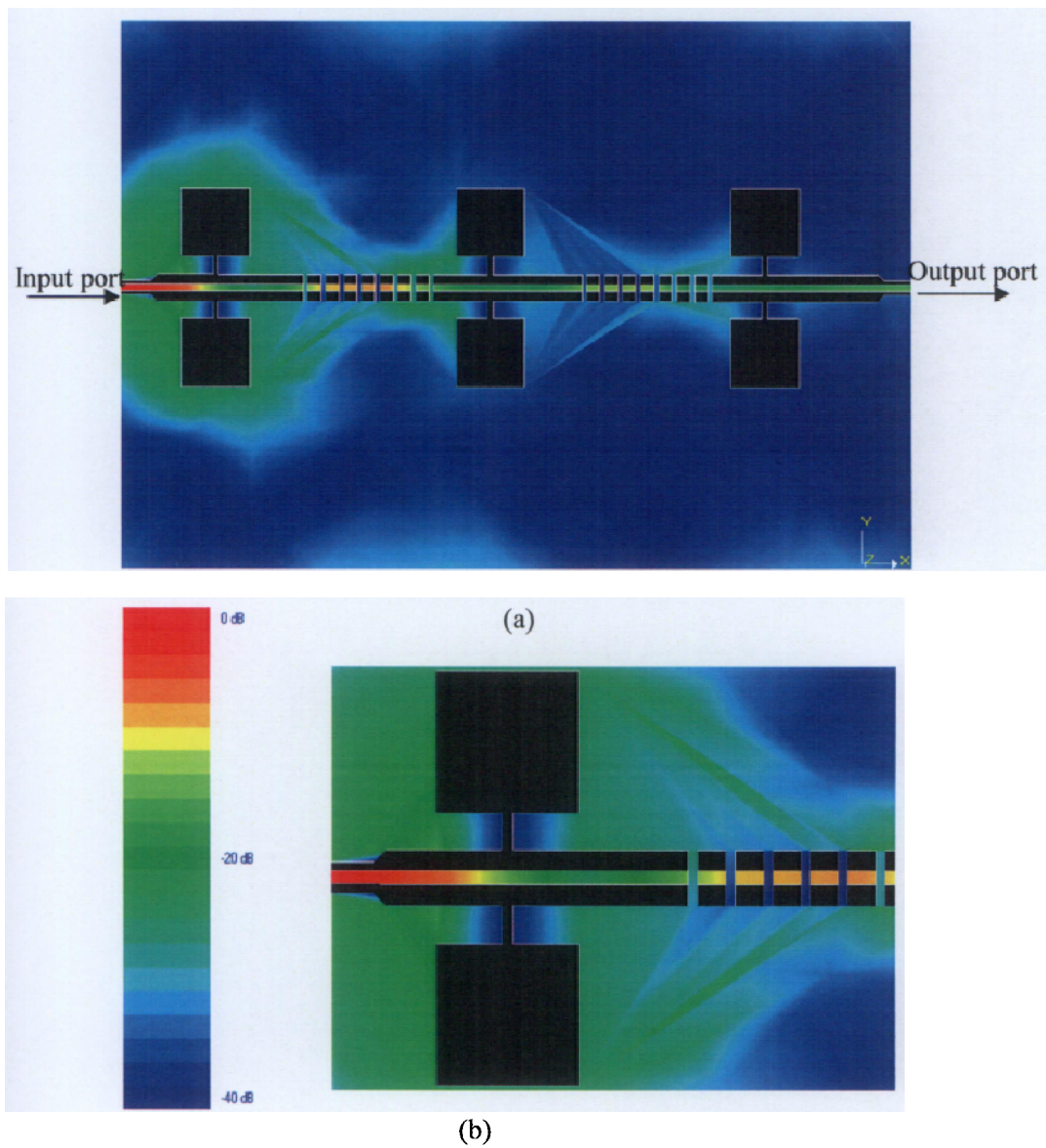
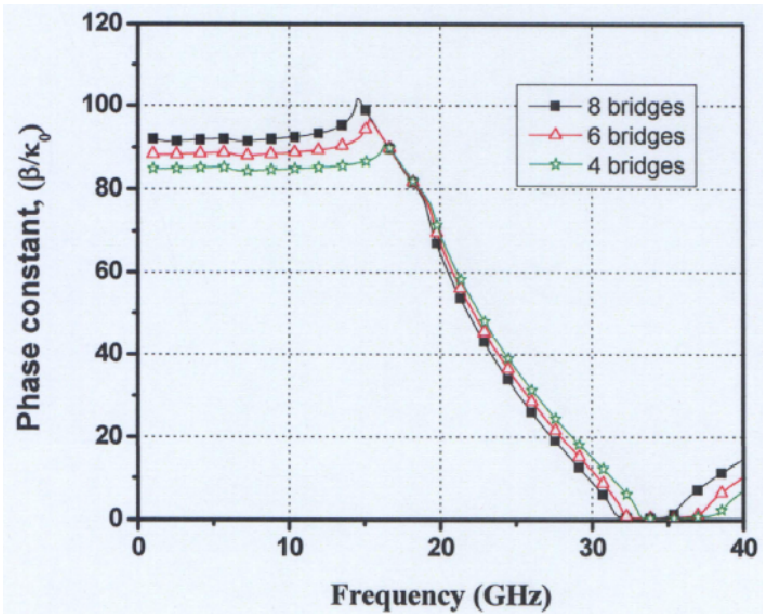
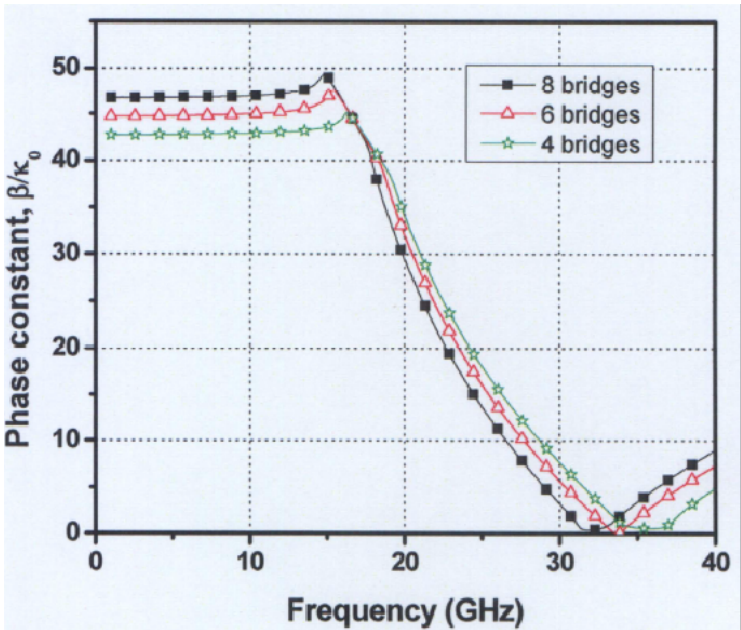


Fig. 4- 25 Simulation result of the current distribution in the micromachined tunable filter; (a) Overview and (b) Zoom view.

Chapter 4 Micromachined Tunable Bandstop Filters



(a)



(b)

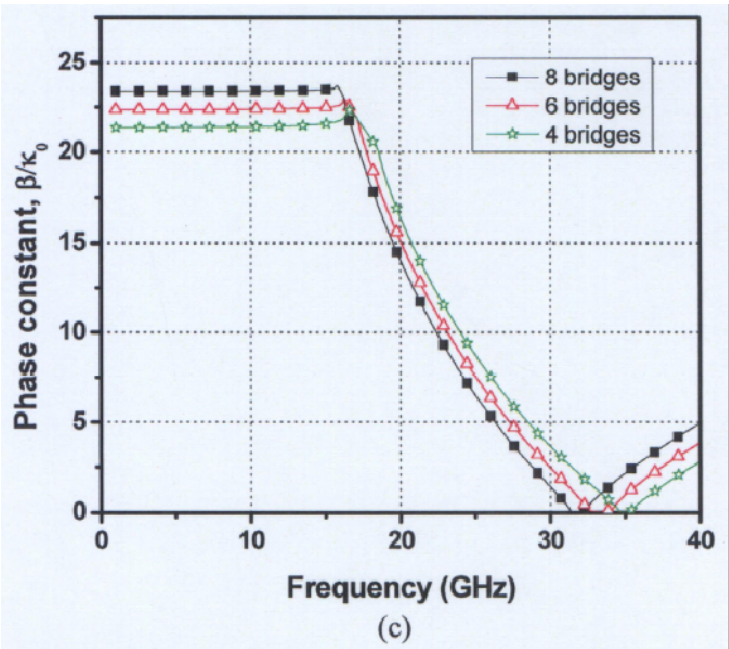


Fig. 4-26 Dispersion diagram of the micromachined bridges loaded on CPW transmission line (a) at a period of 200  $\mu\text{m}$  (b) at a period of 400  $\mu\text{m}$  (c) at a period of 600  $\mu\text{m}$ .

An important phenomenon, which is analyzed here for the first time is the propagation characteristic of the micromachined bridges. Micromachined bridges are periodically placed so the slow wave factor that varies with the number of bridges and the distance between the bridges are investigated. A high impedance CPW transmission line without any perturbation is loaded with the micromachined bridges. Fig. 4-26 (a) shows the dispersion diagram of the periodically loaded micromachined bridges. The distance between the bridges is fixed at 200  $\mu\text{m}$  while the number of bridges is varied. The bandgap for the 8 bridges starts around 15 GHz while for the 6 and 4 bridges at 16 GHz and 16.5 GHz respectively. Although for the 8 bridges the bandstop behavior starts early, but there is little variation in the dispersion at higher frequencies. The results for the

---

#### Chapter 4 Micromachined Tunable Bandstop Filters

---

bridges with a periodic distance of  $400\text{ }\mu\text{m}$  and  $600\text{ }\mu\text{m}$  are also shown in Fig. 4-26 (b) and (c) respectively. The bridges with a periodic distance of  $200\text{ }\mu\text{m}$ , has a phase constant of 100 compared to 50 and 25 for the  $400\text{ }\mu\text{m}$  and  $600\text{ }\mu\text{m}$  distance bridges respectively. Therefore, 8 bridges with a periodic distance of  $200\text{ }\mu\text{m}$  are used on each section of the tunable EBG bandstop filter.

##### 4.2.1 Experimental results and discussions

The SEM photo graph of the MEMS tunable bandstop is shown in Fig. 4-27. Fig. 4-28 shows the measurement results of the S-parameters when the bias voltage between the signal strip and the ground plane is zero [133]. It is found that the measurement and simulation results are in good agreement. The 20-dB rejection bandwidth varies from 17 GHz to 22.5 GHz. In the passband, the return loss is larger than 10 dB except in the higher frequencies. The lower passband insertion loss is around 0.7-1.1 dB.



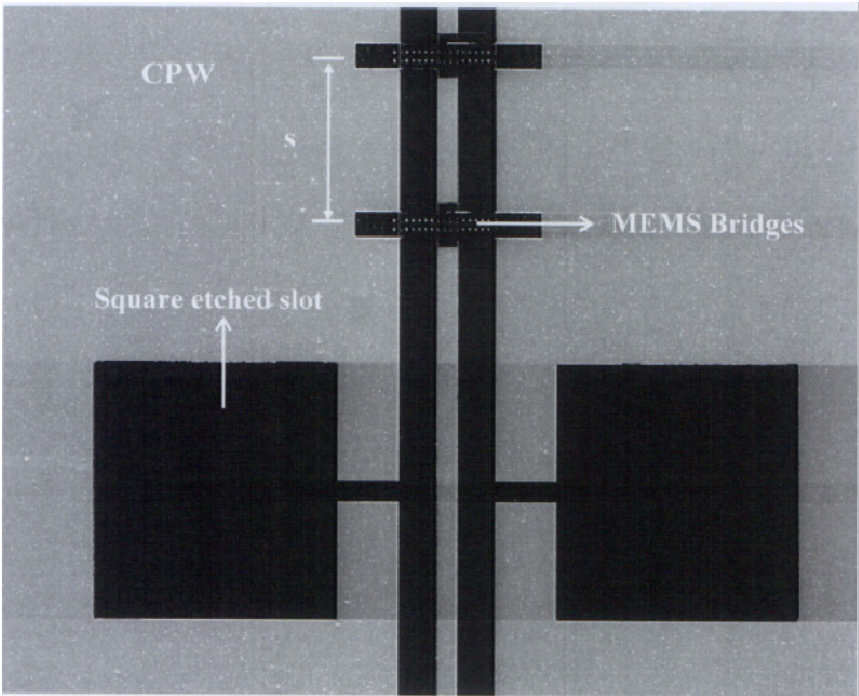


Fig. 4-27 SEM micrograph of the fabricated MEMS tunable EBG bandstop.

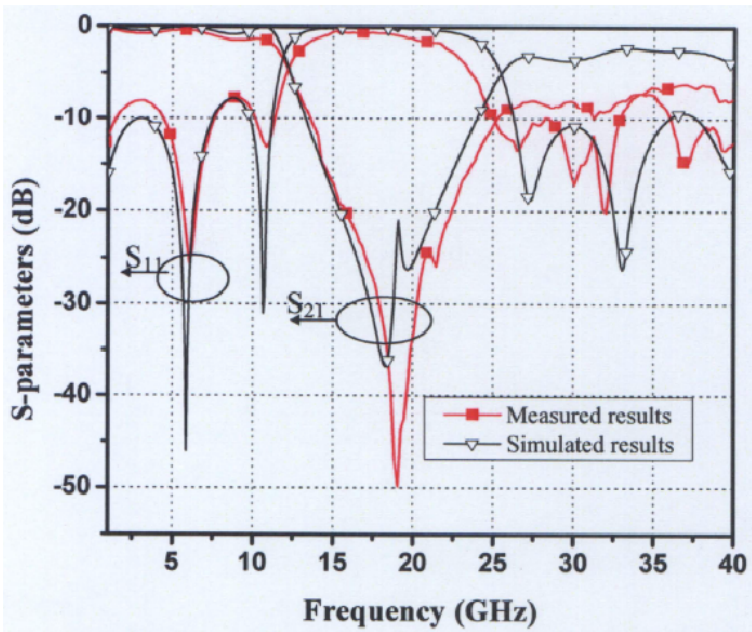
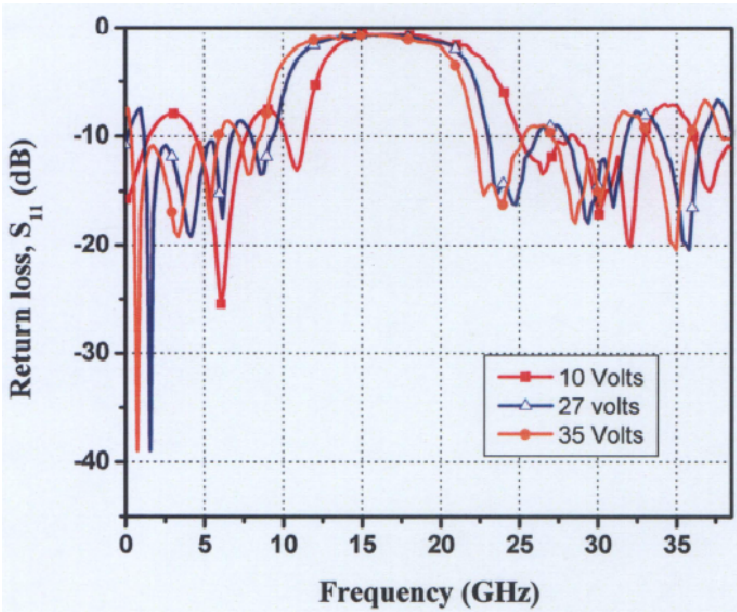
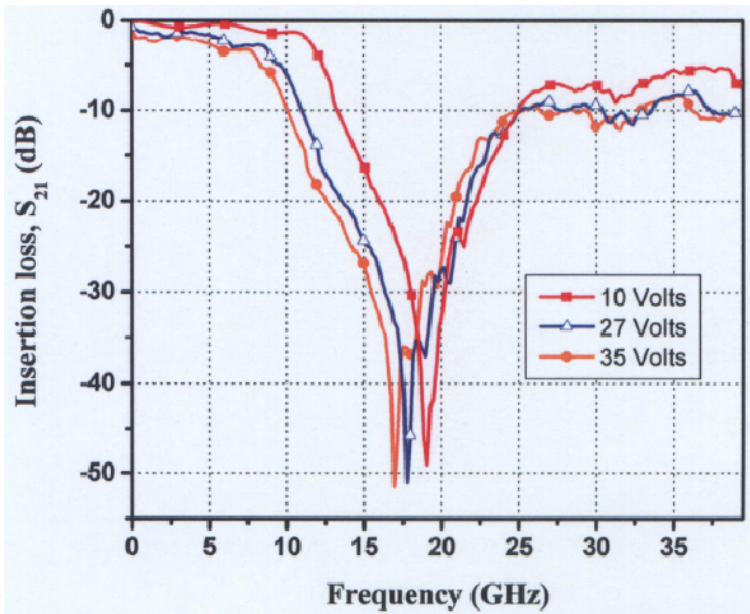


Fig. 4-28 Comparison of the simulation and measurement results of the S-parameters of tunable EBG bandstop filter (zero bias voltage).

Chapter 4 Micromachined Tunable Bandstop Filters



(a)



(b)

Fig. 4-29 Measurement results of the tunable bandstop filter (a) Return loss,  $S_{11}$ , and (b) Insertion loss,  $S_{21}$ .

---

*Chapter 4 Micromachined Tunable Bandstop Filters*

---

The measurement results of the fabricated tunable EBG bandstop filter are shown in Fig. 4-29. There are eight bridges in each section. The initial gap height of the bridges is 2  $\mu\text{m}$ . The 20 dB optimum bandwidth of the EBG bandstop filter is 5.5 GHz as discussed in section 2.4. When a bias voltage of 0~35 V is applied and the frequency is tuned from 19 GHz to 17.3 GHz. Basically this is an analog tuning in which the resonant frequency is varied continuously by changing the capacitance of the MEMS bridges. Overlaps between the tuning frequencies are observed because of continuous tuning, as shown in Fig. 4-29. Most often, continuous tuning is desirable in MEMS applications so that desired frequency bands can be rejected or selected. The lower passband insertion loss varies from 0.7 dB to 2.2 dB due to the change in the gap height of the bridges.

### **4.3 Summary**

In this chapter, the bandstop filter using unloaded and loaded structure has been investigated. The frequency characteristics of the EBG unit cell are studied using the equivalent circuit model. The extracted parameters show that the bandgap effect of the EBG cells can be accurately interpreted based on the circuit analysis theory. The complex characteristic impedance is estimated which is helpful for analyzing the effect of impedance change in the EBG structure. The bandstop filter is also designed by cascading the unloaded and loaded EBG cells. The measured results of the loaded structures shows enhanced passband performance compared to the unloaded structure. Due to higher equivalent capacitance and lower equivalent inductance, it helps in decreasing the insertion loss and increasing the return loss at higher frequencies. The 20 dB stopband is as wide as 13.2 GHz. The lower passband insertion loss is less than 2 dB with 0.2 dB ripple, and the higher passband insertion loss is less than 4.5 dB.

Based on capacitive change of micromachined bridges, a tunable EBG bandstop filter is designed, simulated and fabricated. The micromachined bridges are used as high contrast capacitive elements between the coplanar waveguide ground plane and the signal line to tune the frequency of the band rejection with different bias levels. For the first time, the slow wave factor is calculated for the micromachined bridges, which is helpful in determining the tuning range and periodic behaviour in the tunable filter. The EBG filter and the micromachined bridges are fabricated by surface micromachining process. The measurement results of the tunable bandstop filter show the tuning range from 19 GHz to 17.3 GHz. The insertion loss varies from 0.7 dB to 2.2 dB. The advantages of



#### ***Chapter 4 Micromachined Tunable Bandstop Filters***

---

micromachined tunable bandstop filters are low cost, compactness and has an immense potential to be integrated with the CMOS devices for wireless front end systems.

## CHAPTER 5

### MICROMACHINED TUNABLE BANDPASS FILTERS

The design and fabrication of the CPW EBG bandstop filter and the micromachined tunable bandstop filter are discussed in Chapter 4. In this chapter, a tunable Fabry-Perot (F-P) bandpass filter and a reconfigurable micromachined switching filter are designed and experimented.

In the first section, the F-P bandpass filter is designed by cascading the unit EBG structures. The theoretical aspects of the F-P cavity and the EBG structures are discussed for the filter design. A defect or F-P cavity is created in the periodic structures to generate a bandpass phenomena. Parametric analysis on the defect length and slot dimensions is studied and the design of F-P filter is optimized. Micromachined switches are employed in the defect cavity as tuning elements for bandpass frequency tuning.

The reconfigurable filter based on DC contact micromachined switches is designed and fabricated. An equivalent circuit model is derived for the reconfigurable cell structure. Extracted parameters show the characteristics of both bandpass and bandstop filters which can be accurately analyzed using circuit analysis. The bandpass filter is formed by cascading the unit cell structures. This bandpass filter can be reconfigured as a bandstop filter using the DC contact micromachined switches. Dispersion characteristics are obtained to analyze the electromagnetic wave behavior within the unit cell for the bandpass and bandstop filter based on Floquet's theorem. The rest of the chapter presents

the experimental results and discussions.

## 5.1 Fabry -Perot tunable filter

### 5.1.1 Theory of the Fabry-Perot tunable filter

The Fabry-Perot interferometer is traditionally associated with optical resonators or etalons consisting of two parallel, partially reflecting plates separated by a dielectric of thickness  $d$ , known as cavity gap with a cavity. When collimated light is coupled through the plates a resonance occurs whenever they are separated by an integral number of the half wavelength of the light [134-135]. This concept transfers virtually intact into the microwave region; the difference in implementation arises from the fact that the dimension of microwave instrumentation are typically comparable with the wavelength of the electromagnetic radiation [136]. For microwave transmission line filters,  $Q$  decreases by  $1/\sqrt{f}$  due to high conductor losses. Therefore, at high frequencies the physical size of a cavity operating in low order mode is too small to be practical. Moreover, when a high order mode is used, the resonance of nearby modes is very close in frequency and there is no separation between them, making such resonators unusable.

A conceptual way of avoiding these difficulties is to remove the sidewalls of the cavity resonator, which has the effect of reducing conductor losses and the number of possible resonant modes, as shown in Fig. 5-1. This is also known as Fabry-Perot cavity. For the resonator, the plates must be parallel and the extent must be large enough so that no significant radiation leaves the region between the plates. These constraints can be reduced by using spherical or parabolic shaped reflecting mirrors to focus and confine the energy to a stable mode pattern. For example, a quasi-optical resonator is useful at millimeter wave and sub-millimeter wave frequencies applicable at infrared and visible

wavelengths.

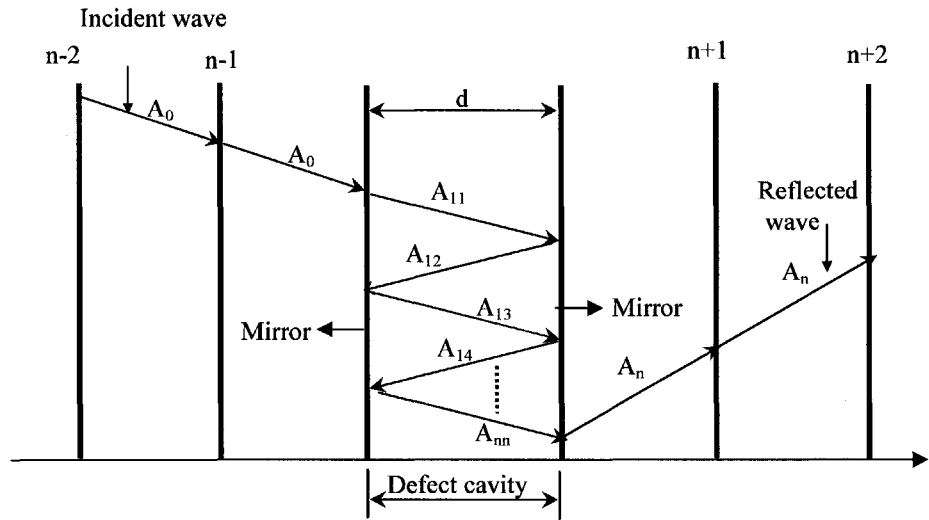


Fig. 5-1 Schematic representation of a Fabry-Perot filter with multilayer parallel plates.

For the multilayer parallel plate as shown in Fig. 5-1, the transverse electromagnetic (TEM) standing wave field between plates is expressed as,

$$E_x = E_0 \sin k_0 z \tag{5-1}$$

$$H_y = j \frac{E_0}{\eta_0} \cos k_0 z \tag{5-2}$$

where  $E_0$  is an arbitrary amplitude constant and  $\eta_0 = 377 \Omega$  is the intrinsic impedance of free space  $k_0$  is the wave number. These fields satisfy the boundary condition  $E_x = 0$  at  $z = 0$  and the boundary conditions of  $E_x = 0$  at  $z = d$ . The resonant frequency can be

---

*Chapter 5 Micromachined Tunable Bandpass Filters*

---

expressed as,

$$k_0 d = l\pi, \quad l = 1, 2, 3, \dots, n \quad (5-3)$$

$$f_0 = \frac{ck_0}{2\pi} = \frac{cl}{2d}, \quad l = 1, 2, 3, \dots, n \quad (5-4)$$

where  $l$  is only a single index for these modes, as opposed to three indices for rectangular or cylindrical cavities, which is a consequence without the conducting walls.

The stored electric energy per square meter of cross section is,

$$W_e = \frac{\epsilon_0}{4} \int_{-d}^d |E_x|^2 dz = \frac{\epsilon_0 |E_0|^2 d}{8} \quad (5-5)$$

and the stored magnetic energy per square meter of cross section is,

$$W_m = \frac{\mu_0}{4} \int_{-d}^d |H_y|^2 dz = \frac{\epsilon_0 |E_0|^2 d}{8} \quad (5-6)$$

which is equal to the stored electric energy. The power lost per square meter in both conducting plates is,

$$P_c = 2 \left( \frac{R_s}{2} \right) |H_y(z=0)|^2 = \frac{R_s |E_0|^2}{\eta_0^2} \quad (5-7)$$

Therefore, the conductor loss quality factor  $Q_c$  can be determined as,

---

*Chapter 5 Micromachined Tunable Bandpass Filters*

---

$$Q_c = \frac{\omega(W_e + W_m)}{P_c} = \frac{\pi l \eta_0}{4R_s} \quad (5-8)$$

Eq. (5-8), shows that the  $Q_c$  increases in proportion to the mode number,  $l$ ; which is often several thousand or more for such resonators. If the region between the plates is filled with a dielectric material with a loss factor,  $\tan \delta$ , the quality factor for the dielectric loss  $Q_d$  can be expressed as,

$$Q_d = \frac{1}{\tan \delta} \quad (5-9)$$

This equation is useful for finding the quality factor for the EBG F-P filter.

### 5.1.2 Design of the EBG circuit

Periodic structures or EBG structures are basically an infinite transmission line or waveguide periodically loaded with reactive elements. The loading elements are formed as discontinuities in the transmission line, the model of lumped reactance across the transmission line is shown in Fig. 5-2. The periodic structures support slow wave propagation (slower than the phase velocity of the unloaded line), which can provide the function of passband and stopband behaviour that can be used to design the bandpass and bandstop filter.

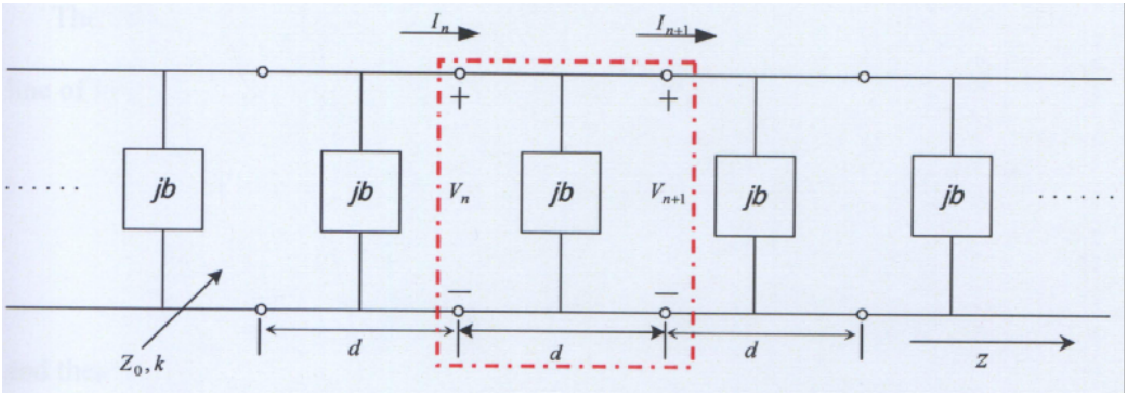


Fig. 5-2 Equivalent circuit of a periodically loaded transmission line.

5.1.2.1 Capacitively loaded transmission line circuit analysis

The wave propagation characteristic of the infinite loaded line is shown in Fig. 5-2. Each unit cell of this line consists of a length  $d$  of transmission line and a shunt susceptance across the midpoint of the line; the shunt susceptance  $b$  is normalized to the characteristic impedance  $Z_0$ . The capacitively loaded transmission line can be analyzed to conceive the idea on periodic structures. The infinite line can be considered as a cascade of identical two-port networks. The voltage and current on either side of the  $n^{\text{th}}$  unit cell matrix can be expressed in a matriceal form as,

$$\begin{bmatrix} V_n \\ I_n \end{bmatrix} = \begin{bmatrix} A & B \\ C & D \end{bmatrix} \begin{bmatrix} V_{n+1} \\ I_{n+1} \end{bmatrix} \quad n = 1, 2, 3, \dots, N \quad (5-10)$$

where  $A$ ,  $B$ ,  $C$  and  $D$  are the matrix parameters,  $V_n$  is the voltage at the  $n^{\text{th}}$  unit cell, and  $I_n$  is the current at the  $n^{\text{th}}$  unit cell.

## Chapter 5 Micromachined Tunable Bandpass Filters

The ABCD matrix for the shunt susceptance  $b$  sandwiched between two transmission line of length  $d/2$  as shown in dotted line of Fig. 5-2 can be expressed as [13],

$$\begin{bmatrix} A & B \\ C & D \end{bmatrix} = \begin{bmatrix} \cos \frac{\theta}{2} & j \sin \frac{\theta}{2} \\ j \sin \frac{\theta}{2} & \cos \frac{\theta}{2} \end{bmatrix} \begin{bmatrix} 1 & 0 \\ jb & 1 \end{bmatrix} \begin{bmatrix} \cos \frac{\theta}{2} & j \sin \frac{\theta}{2} \\ j \sin \frac{\theta}{2} & \cos \frac{\theta}{2} \end{bmatrix} \quad (5-11)$$

and then Eq. (5-11) can be simplified as,

$$\begin{bmatrix} A & B \\ C & D \end{bmatrix} = \begin{bmatrix} \left( \cos \theta - \frac{b}{2} \sin \theta \right) & j \left( \sin \theta + \frac{b}{2} \cos \theta - \frac{b}{2} \right) \\ j \left( \sin \theta + \frac{b}{2} \cos \theta + \frac{b}{2} \right) & \left( \cos \theta - \frac{b}{2} \sin \theta \right) \end{bmatrix} \quad (5-12)$$

where  $\theta = kd$ , and  $k$  is the propagation constant of the unloaded line. For any wave propagating in the  $+z$  direction, the voltage and current can be expressed as,

$$V(z) = V(0)e^{-\gamma z} \quad (5-13a)$$

$$I(z) = I(0)e^{-\gamma z} \quad (5-13b)$$

for a phase reference at  $z = 0$ . Since the structure has an infinite length, the voltage and current at the  $n^{\text{th}}$  terminals can differ from the voltage and current at the  $n+1$  terminals only by the propagation factor,  $e^{-\gamma d}$ . Thus, it can be expressed as,

$$V_{n+1} = V_n e^{-\gamma d} \quad (5-14a)$$

$$I_{n+1} = I_n e^{-\gamma d} \quad (5-14b)$$



---

*Chapter 5 Micromachined Tunable Bandpass Filters*

---

Substituting Eq. (5-14) into Eq. (5-10), it can be expressed as,

$$\begin{bmatrix} V_n \\ I_n \end{bmatrix} = \begin{bmatrix} A & B \\ C & D \end{bmatrix} \begin{bmatrix} V_{n+1} \\ I_{n+1} \end{bmatrix} = \begin{bmatrix} V_{n+1} e^{\gamma d} \\ I_{n+1} e^{\gamma d} \end{bmatrix} \quad (5-15a)$$

or

$$\begin{bmatrix} A - e^{-\gamma d} & B \\ C & D - e^{-\gamma d} \end{bmatrix} \begin{bmatrix} V_{n+1} \\ I_{n+1} \end{bmatrix} = 0 \quad (5-15b)$$

For a nontrivial solution, the determinant of the above matrix can be expressed as,

$$AD + e^{2\gamma d} - (A + D)e^{\gamma d} - BC = 0 \quad (5-16)$$

Using the property of ABCD matrix for the reciprocal network,  $AD - BC = 1$ , then Eq. (5-16) can be simplified as,

$$1 + e^{2\gamma d} - (A + D)e^{\gamma d} = 0 \quad (5-17)$$

$$e^{-\gamma d} + e^{\gamma d} = A + D \quad (5-18)$$

Therefore,

$$\cosh \gamma d = \frac{A + D}{2} = \cos \theta - \frac{b}{2} \sin \theta \quad (5-19)$$

If  $\gamma = \alpha + j\beta$ , Eq. (5-19) can be expressed as,

$$\cosh \gamma d = \cosh \alpha d \cos \beta d + j \sinh \alpha d \sin \beta d = \cos \theta - \frac{b}{2} \sin \theta \quad (5-20)$$

Since the right hand side of Eq. (5-20) is real, we have either  $\alpha = 0$  or  $\beta = 0$ .

---

*Chapter 5 Micromachined Tunable Bandpass Filters*

---

When  $\alpha = 0$  and  $\beta \neq 0$ , the structure has a non attenuating behavior, i.e. the waves propagate along the periodic structure and it generates a passband phenomena. Hence, Eq. (5-20) can be expressed as,

$$\cos \beta d = \cos \theta - \frac{b}{2} \sin \theta \quad (5-21)$$

When the magnitude of the right hand side is less than or equal to unity, there are an infinite number of values of  $\beta$  that satisfy Eq. (5-21).

When  $\alpha \neq 0$  and  $\beta = 0$ , there is no wave propagation i.e. the waves are reflected back to the input of the transmission line and this defines the stopband phenomena. Hence, Eq. (5-21) is simplified to,

$$\cos \alpha d = \left| \cos \theta - \frac{b}{2} \sin \theta \right| \geq 1 \quad (5-22)$$

Eq. (5-21) and Eq. (5-22) are very important for the understanding of the propagation of EM waves through periodic structures. Attenuation of waves generate the appearance of stopbands while the propagation of unattenuated waves exhibits passband regions. Thus, these equations help to explain the stopband and passband characteristics of EBG.

The EBG bandpass filter is designed based on the F-P mathematical model.

### 5.1.3 Design of Fabry-Perot tunable bandpass filter

A uniplanar one dimensional (1D) EBG structure is realized on a CPW structure. These unit EBG cells are placed at a period which is equal to half of the centre frequency wavelength. A defect cavity is realized when the periodicity is changed. This is shown in Fig. 5-3. The center resonant line (defect cavity) with periodic EBG reflectors on both sides is analogous to Fabry-Perot (F-P) resonators. The prohibition of wave propagation in the forbidden gap makes the periodic structures to act as reflectors. The waves are bounded back and forth within the defect cavity. The defect cavity  $L_R$  is defined as,

$$L_R = 1.5 d \quad (5-23)$$

where  $d$  is the period i.e. the distance between each EBG structures.

The arrangement of the EBG structures satisfies the Bragg conditions as proven earlier. The stopband generated is given by,

$$\beta = \frac{2\pi}{\lambda_g} \quad (5-24)$$

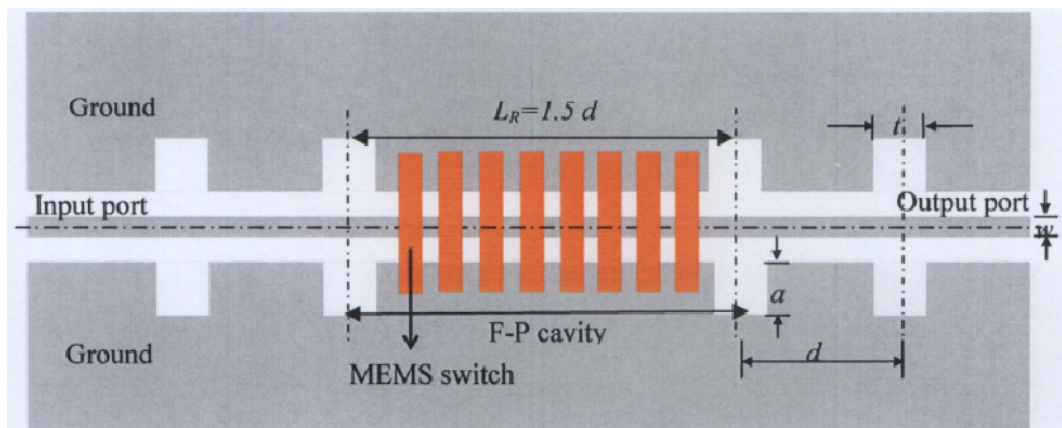


Fig. 5-3 Schematic of EBG Fabry-Perot filter.

where  $\beta$  is the propagation constant and the  $\lambda_g$  is the guided wavelength and,

$$d = \frac{\lambda_g}{2} \tag{5-25}$$

An equivalent circuit model of the EBG Fabry-Perot filter is shown in Fig. 5-4. Each EBG cells is modeled with a parallel  $LC$  resonant circuit.  $L_1$  and  $C_1$  are the inductance and the capacitance of the etched EBG on the left side and right hand side of the defect cavity, respectively. The defect cavity,  $L_R$ , is loaded with MEMS capacitive switches and modeled as  $C_2$  and  $L_2$ . The extracted parameters of the F-P EBG filter are listed in Table 5-1.

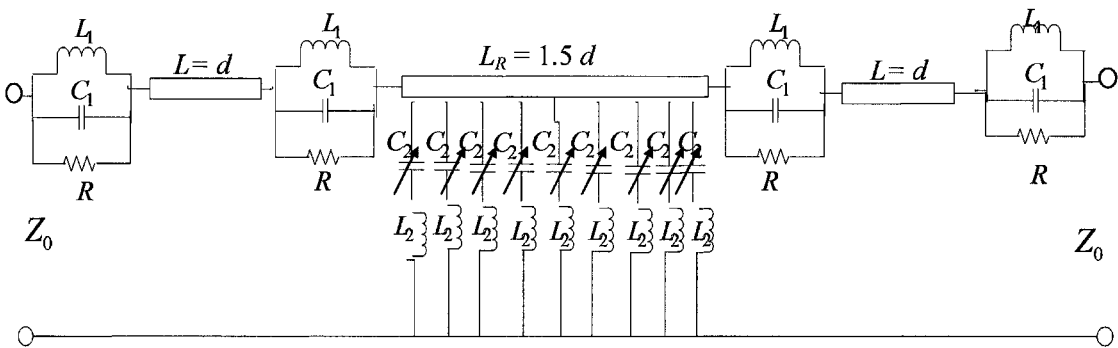


Fig. 5-4 Equivalent circuit model of the EBG Fabry-Perot tunable filter.

Table 5-1 Extracted circuit parameters for tunable F-P EBG filter.

Variable capacitance $C_2$ (pF)	0.015	0.017	0.022	0.025
Resonant Frequency (GHz)	11.10	10.70	9.6	9.4
Inductance $L_1$ (nH)	0.8	0.8	0.8	0.8
Fixed Capacitance $C_1$ (pF)	0.13	0.13	0.13	0.13

### 5.1.3.1 Effect of the number of EBG cells

The relationship between the number of EBG cells associated with the Q factor is shown in Fig. 5-5. For an optimum bandpass filter design, the Q-factor is greater than 40. When the number of EBG cells on both sides of the defect cavity is increased, the reflectivity of the Bragg mirrors also increases, but the coupling into the cavity is reduced. When four EBG cells are used, the Q factor is around 180. It increases approximately to 480, after which the energy accumulation in the cavity saturates as shown in Fig. 5-5.

The dielectric constant of the substrate plays an important role in providing a high Q factor. Specifically, Q is inversely proportional to the dielectric constant of the substrate. As a result, a high resistivity silicon substrate is preferred compared to low resistivity silicon substrate.

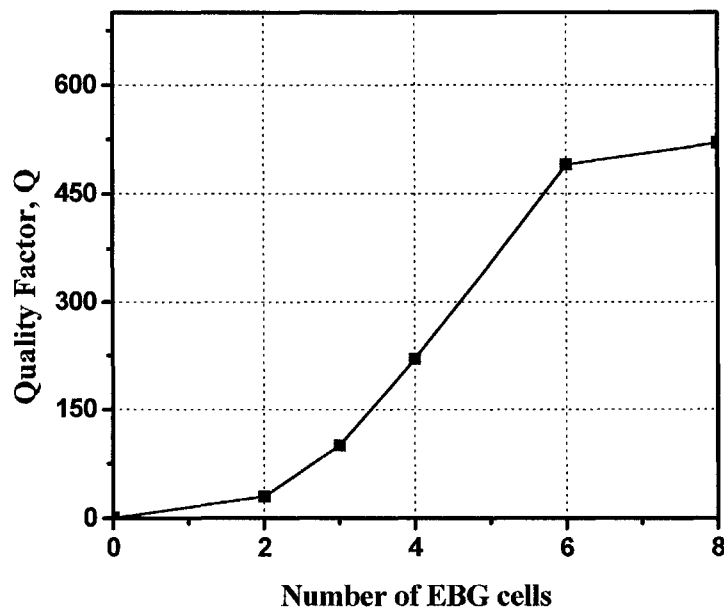


Fig. 5-5 Simulation results for the relationship between the Q factor versus the number of EBG cells.

Chapter 5 Micromachined Tunable Bandpass Filters

Figure 5-6 shows the influence of the numbers of EBG cells on the insertion loss and the attenuation. For an efficient bandpass filter design [14], the criteria is set such that the insertion loss is as low as possible and the attenuation is set as high as possible. For 4 EBG cells, the insertion loss and attenuation is 0.9 dB and 23 dB, respectively, while the insertion loss and attenuation for 8 EBG cells is 10.1 dB and 40 dB, respectively. It is noted that the attenuation increases at the expense of the insertion loss. This is because the conductor loss increases with the size of EBG filter. As a result, the insertion loss and the attenuation are optimum when the number of EBG cells is four.

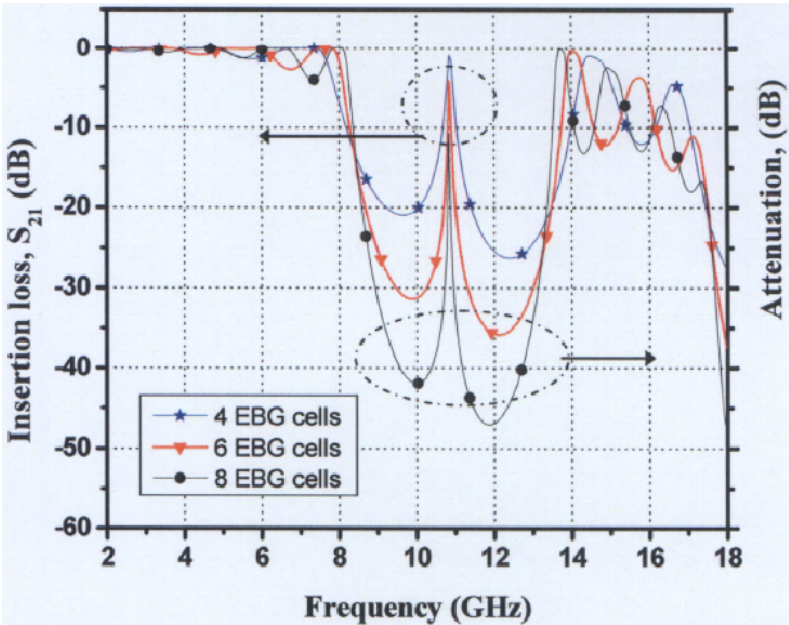
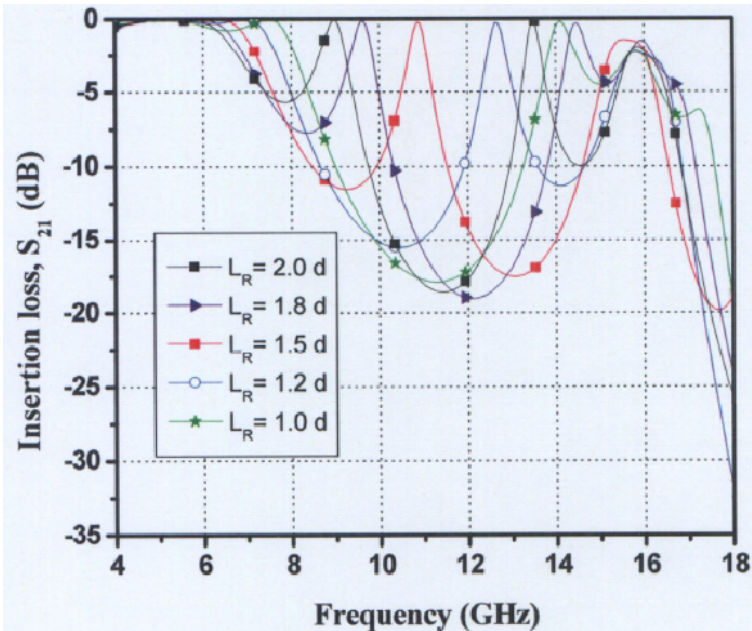
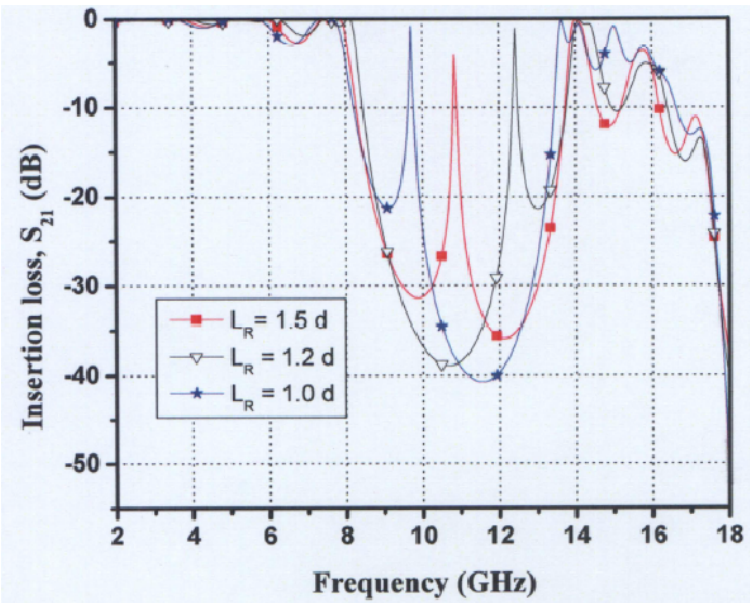


Fig. 5-6 Simulation for insertion loss and attenuation versus the number of EBG cells.



(a)



(b)

Fig. 5-7 Simulation results of the varying defect lengths (a) for  $n = 4$  EBG cells; and (b) for  $n = 6$  EBG cells.



### 5.1.3.2 Effect of the defect length

In this sub-section, the defect length,  $L_R$  is varied and its effect on the filter characteristics is analyzed. The defect length  $L_R$ , is to change from  $L_R = 1\ d$  to  $L_R = 2\ d$ , as shown in Fig. 5-7 (a). When  $L_R = d = \lambda_g / 2$ , according to Eqs. (5-24) and (5-25), no resonance peak in the transmission curve is observed, that means no defect cavity present to generate or accumulate the energy. However, a slight change of the defect length of  $L_R = 1.2\ d$ , a resonance peak appears at 12.6 GHz, but the upper rejection level is not symmetrical. When the defect cavity is further increased to  $L_R = 1.8\ d$  to  $L_R = 2\ d$ , the lower rejection level deteriorates and the resonance frequency shifted to lower frequency. The insertion loss does not change with the variation in the defect length, but the F-P resonant frequency is shifted from 9.71 GHz to 8.98 GHz. The optimum resonant length is  $L_R = 1.5\ d$ , when both the upper and lower rejection levels are approximately symmetrical. The results are quite similar in terms of the symmetry of the upper and lower rejection, when number of EBG cells i.e.  $n = 4$  and  $n = 6$  as shown in Figs. 5-7 (a) and 5-7 (b).

### 5.1.3.3 Effect of the slot dimension, $t$

The EBG cells designed on the ground plane of the CPW transmission line are square, with a length and width each equal to  $\lambda_g / 4$ . In this subsection, the width is changed to analyze its influence on the transmission curve. When the slot is perfectly square,  $t = 1220\ \mu\text{m}$ , the insertion loss is 2 dB and attenuation is greater than 25 dB. When the slot,  $t = 610\ \mu\text{m}$  but  $a$  remains as  $\lambda_g / 4$ , the insertion loss improves but with attenuation less than 20 dB as shown in Fig. 5-8.



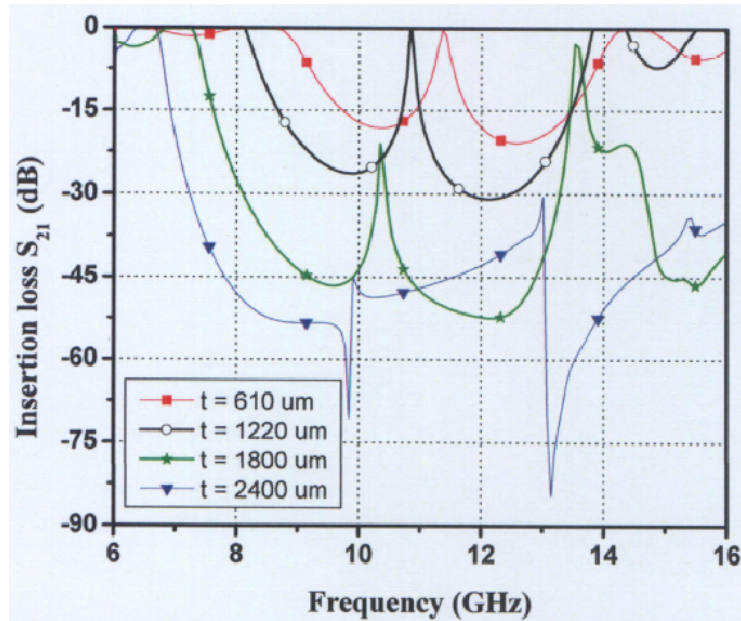


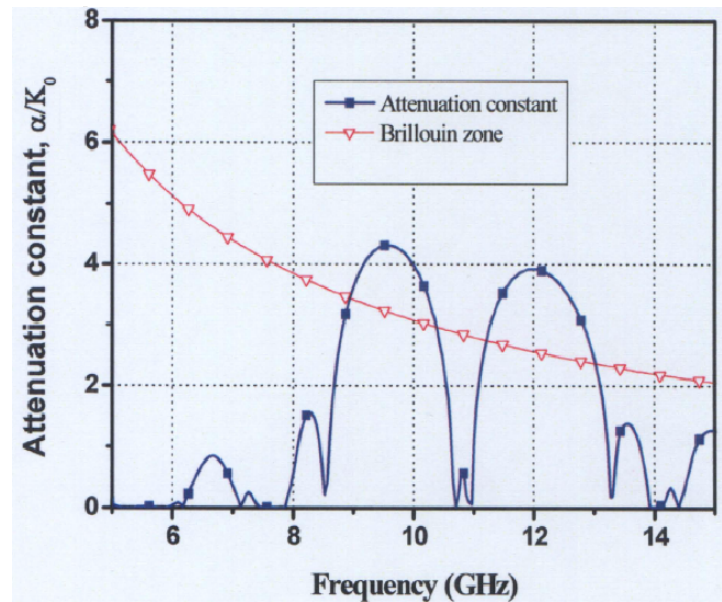
Fig. 5-8 Simulation result of the effect of varying slot length  $t$  on the insertion loss  $S_{21}$ .

On the other hand, when  $t = 2400 \mu\text{m}$ , the performance of the F-P filter deteriorates in terms of insertion loss of 45 dB but the attenuation improves to 50 dB. The optimum design selected for F-P filter with minimum insertion loss and high attenuation is,  $t = 1220 \mu\text{m}$ .

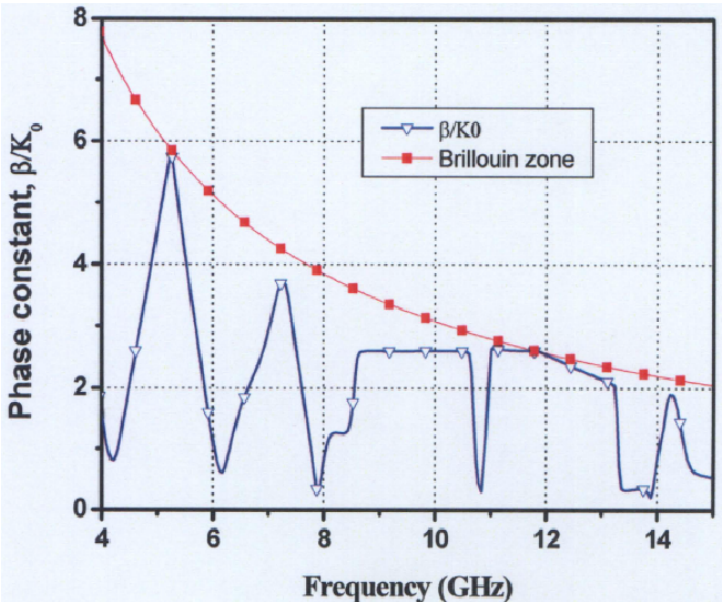
#### 5.1.3.4 Effect of propagation characteristics

The propagation characteristic of the F-P EBG is analyzed using the Floquet's theorem. The propagation factor is  $e^{-\gamma\Lambda}$ , where  $\Lambda = 4878 \mu\text{m}$  is the period of the EBG structure, and  $\gamma = \alpha + j\beta$  is the complex propagation constant in the direction of transmission.

Chapter 5 Micromachined Tunable Bandpass Filters



(a)



(b)

Fig. 5-9 Dispersion diagram of EBG F-P filter (a) Attenuation curve (b) Propagation curve.

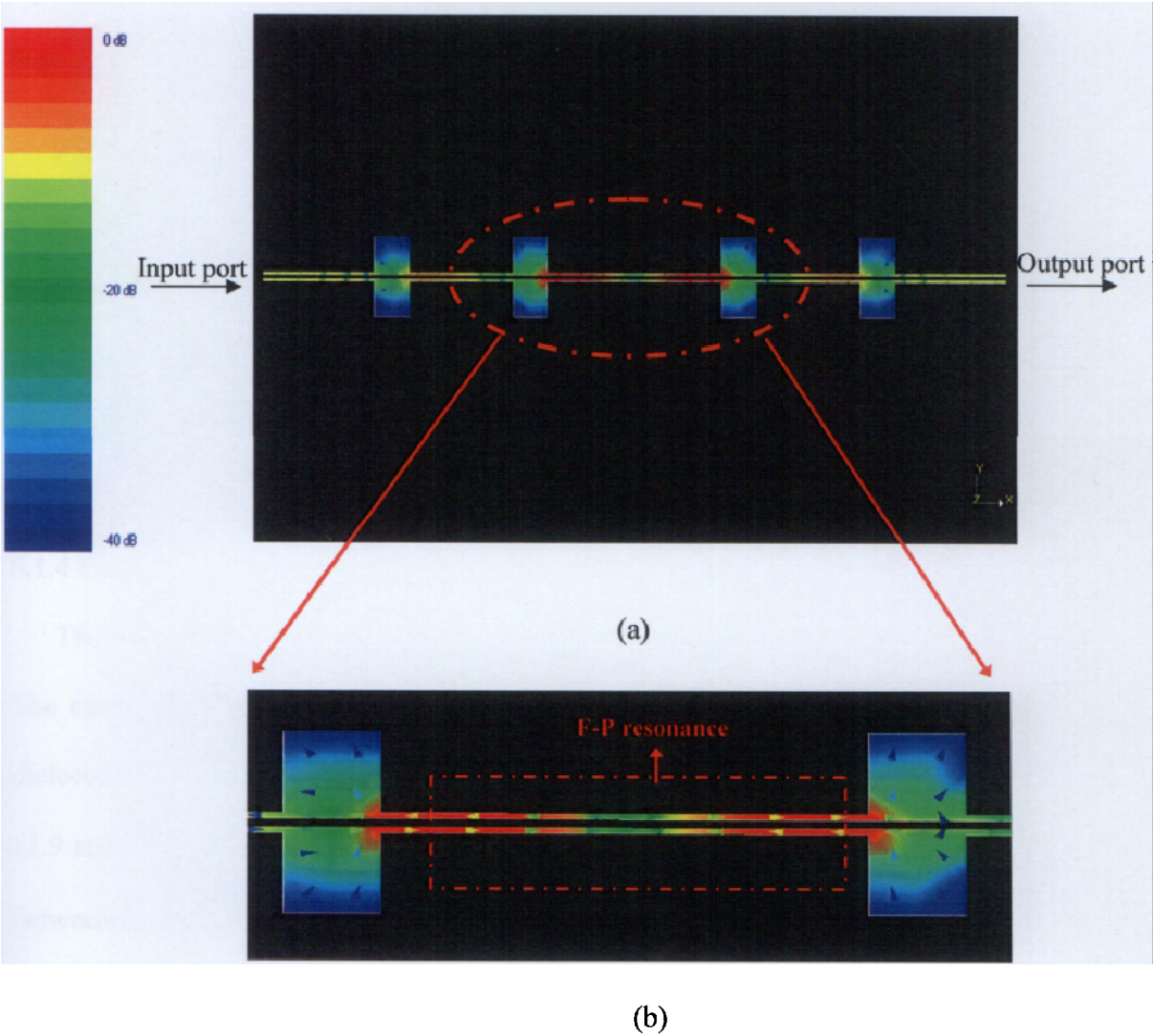


Fig. 5-10 Simulation results of current distribution of the tunable F-P filter at 11.4 GHz  
(a) Overview and (b) Magnified image of the region as highlighted in (a).

The normalized phase constant  $\beta/k_0$  and the attenuation constant  $\alpha/k_0$  are shown in Fig. 5-9. When  $\beta/k_0$  is close to the Bragg condition ( $\beta \Lambda = \pi$ ), the signal is highly attenuated. The stopband is very wide and the propagation is prohibited. At 11.4 GHz, the attenuation is almost zero which indicates the presence of the bandpass filter as shown in

Fig. 5-9 (a). When the frequency is higher than 17 GHz, the periodic structure supports fast-wave mode, i.e.,  $\beta/k_0 < 1$ , with small attenuation.

Figure 5-10 shows the current distribution of the F-P EBG filter. At 11.4 GHz, there is no attenuation in the EBG structure as the signal can pass through. At other frequencies, the bandgap phenomena occur where the signal is totally rejected. The current distribution has further validates the existence of the bandpass filter in the EBG structures.

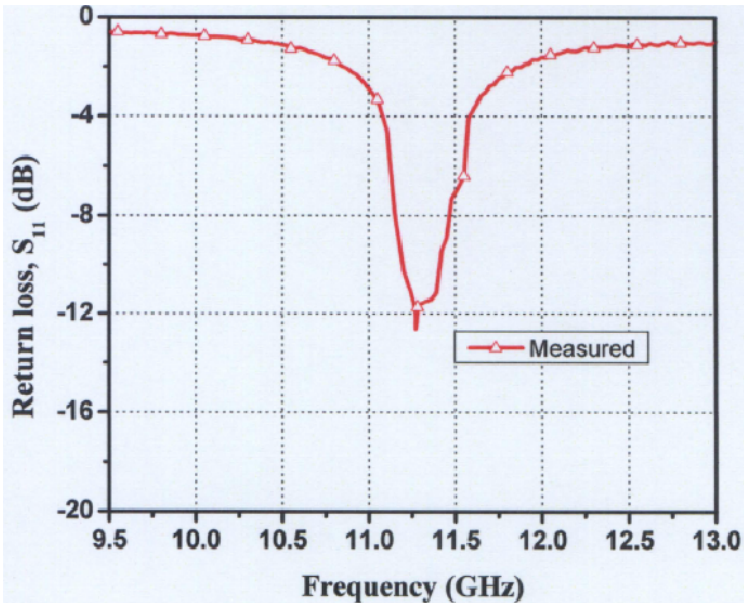
#### 5.1.4 Experimental results and discussions

The EBG F-P tunable filter is fabricated using the surface micromachining process. The circuit length is dependent on the number of cells, the central frequency and the dielectric constant. High resistivity silicon substrate is used with a dielectric constant of 11.9 and height of 725  $\mu\text{m}$ . The stopband center frequency is 12.5 GHz and the distance between the cells or the EBG cell period is 4878  $\mu\text{m}$ . The EBG structure is connected to input and output port using 50  $\Omega$  feed lines.

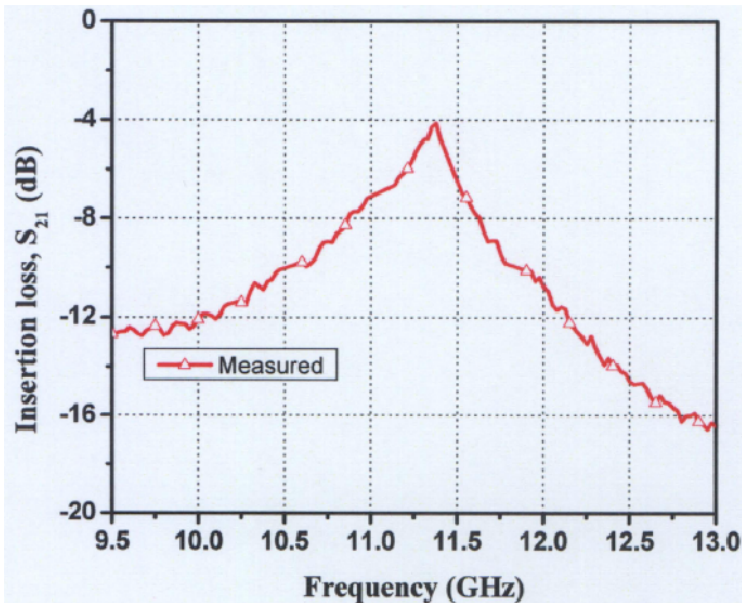
The fabricated EBG F-P filter consists of four EBG cells. The S-parameters of the F-P filter is shown in Fig. 5-11. The insertion loss is 4 dB at 11.4 GHz. The return loss is greater than 12 dB. The Q factor of the filter is 70.



Chapter 5 Micromachined Tunable Bandpass Filters



(a)



(b)

Fig. 5-11 Comparison between the simulation and measurement results; (a) Return loss,  $S_{11}$  (b) Insertion loss,  $S_{21}$ .

Chapter 5 Micromachined Tunable Bandpass Filters

The tunable F-P EBG bandpass filter consists of MEMS bridges is shown in Fig. 5-12. These bridges are capacitively loaded on the defect cavity. The width  $w$  and length  $l$  of the bridges are  $50\text{ }\mu\text{m}$  and  $300\text{ }\mu\text{m}$ , respectively. There are 8 bridges and the periodic spacing between the bridges,  $s$  is  $500\text{ }\mu\text{m}$ . The initial height of the bridges is  $2\text{ }\mu\text{m}$ . The filter is simulated using commercial software IE-3D.

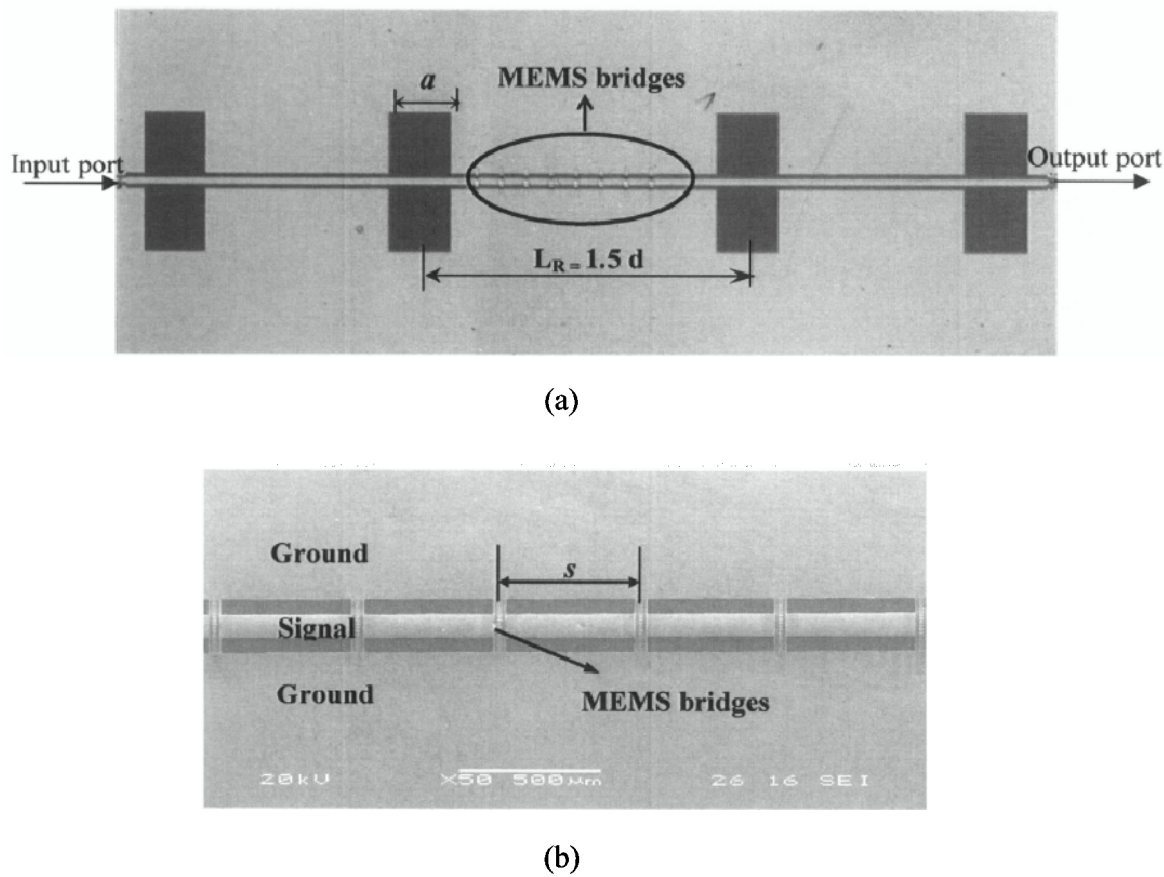
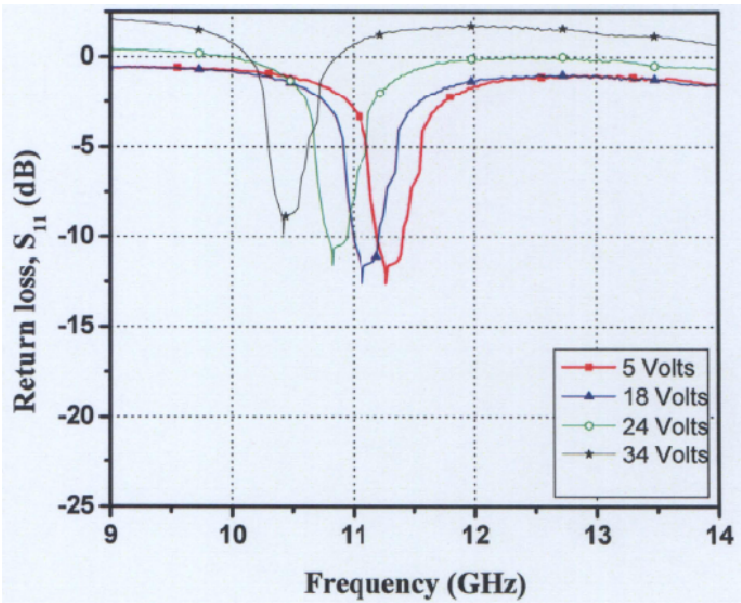
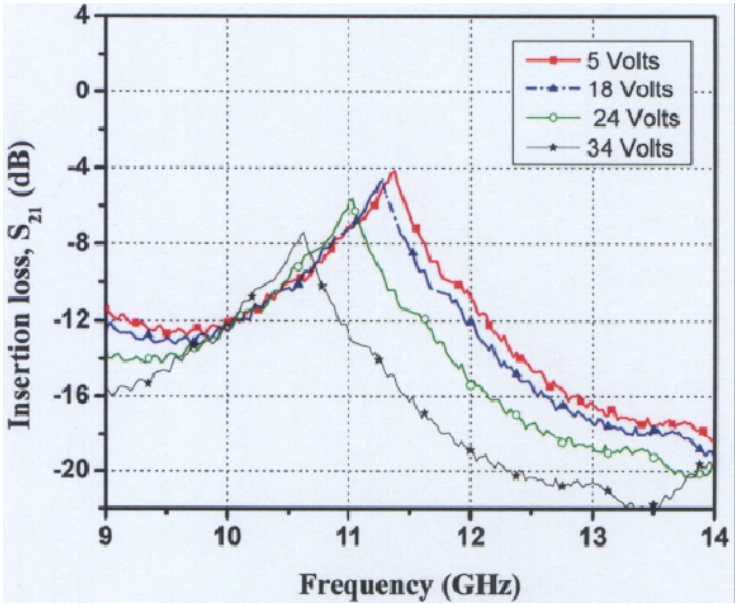


Fig. 5-12 Tunable Fabry-Perot EBG filter (a) Photograph of the F-P filter (b) Enlarged view of MEMS bridges.

Chapter 5 Micromachined Tunable Bandpass Filters



(a)



(b)

Fig. 5-13 Measurement result of the tunable F-P EBG filter (a) Return loss,  $S_{11}$  (b) Insertion loss,  $S_{21}$ .

Chapter 5 Micromachined Tunable Bandpass Filters

The measured results are shown in Fig. 5-13. When the drive voltage is 5 volts, the central frequency is 11.39 GHz, its insertion loss is 4.1 dB while Q of the filter is 70. When the voltage increases from 20 V to 24 V, the frequency is shifted from 11.39 GHz to 11.04 GHz with insertion loss ranges from 4.5 dB to 5.5 dB.

When the applied voltage increases from 24 V to 34 V, the insertion loss increases significantly. The reason is that some of the bridges are pulled down completely. The tuning range is around 7.5% in the X-band as shown in Fig. 5-13. The measurement results are summarized in Table 5-2. The central frequency, insertion loss and return loss are listed for different values of the bias voltage, V. The difference between the simulation and the measurement results is due to the fabrication tolerance and the substrate loss.

Table 5-2 Measurement results of the tunable F-P EBG filter

Bias voltage (V)	5	18	24	34
Frequency (GHz)	11.39	11.04	10.85	10.4
Insertion loss (dB)	4.1	4.6	5.6	7.35
Return loss (dB)	12.2	11.8	10.9	9.5



5.2 A Reconfigurable switching filter

5.2.1 Design of the reconfigurable filter

The reconfigurable filter structure consists of three unit EBG cells and DC contact MEMS switches, as shown in Fig. 5-14. These unit EBG cells are placed periodically at a distance equal to half of the wavelength of the central frequency. Before analyzing the reconfigurable filter, the unit EBG cell structure is investigated in detail. A lattice shaped unit EBG structure is shown in Fig. 5-15. In the unit cell structure, a small square slot is etched in the ground plane with a side length  $a$ . The smaller square etched slot is connected to the gap by a narrow transverse slot with length of  $w_s$  and width of  $d_s$  as shown in Fig. 5-15 with dotted lines.

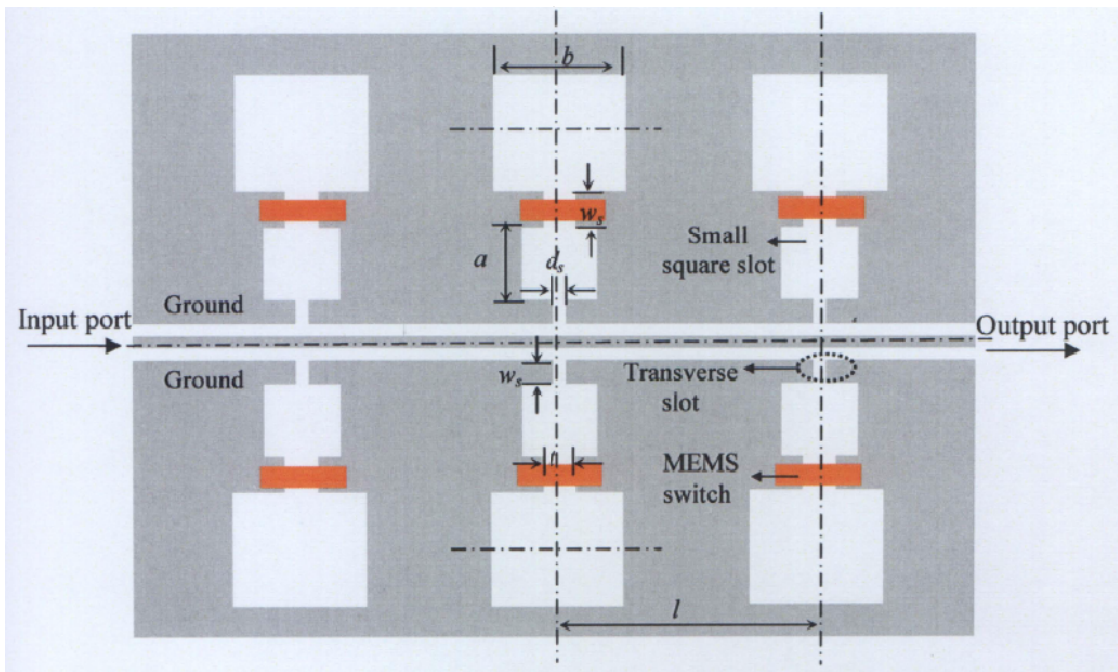


Fig. 5-14 Schematic of the MEMS reconfigurable filter.

Chapter 5 Micromachined Tunable Bandpass Filters

Another bigger square slot of size  $b$  and the transverse slot are etched on top of the smaller square slot. The resonance frequency depends on the size of the transverse slot and the square etched hole in the ground plane. The EM and circuit simulation is performed using commercial software Advanced Design System (ADS), Agilent technologies. The circuit modeling shows a bandpass appears in the characteristics when a bigger square slot of size  $b$  is used together with the transverse slot, otherwise the structure behaves like a bandstop filter.

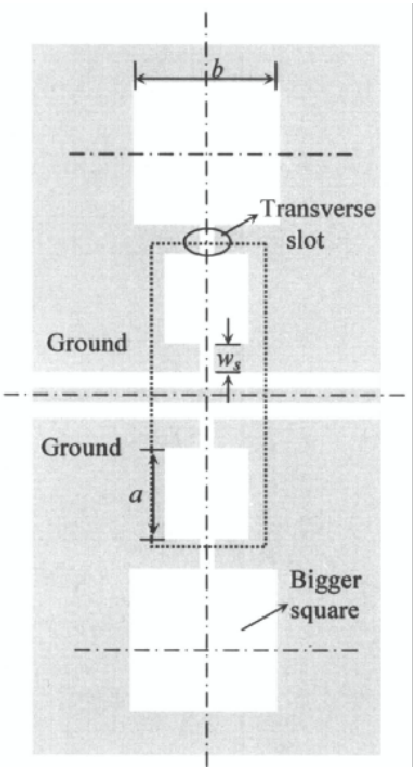


Fig. 5-15. Schematic of the unit reconfigurable cell structure.

5.2.1.1 Unit reconfigurable cell structure and its modeling

An equivalent parallel  $LC$  circuit shown with dotted lines in Fig. 5-16 is used to model the EBG structure. It consists of a series inductor, parallel capacitor and a resistor. From a practical point of view, the unit cell structure can serve as a replacement for the parallel  $LC$  resonant circuit in many applications. To apply the EBG cell to a practical circuit, it is necessary to extract the equivalent circuit parameters, which can be obtained from the simulation result of the unit cell structure. The lumped capacitance  $C_1$  is mainly contributed by the transverse slot on the ground, while the inductance  $L_1$  is related to the magnetic flux passing through the small square aperture of size  $a$  on the ground. The equivalent circuit parameters are extracted and presented in Table 5-3. The circuit simulation result is obtained using the equivalent circuit parameters as shown in Fig. 5-17. A comparison is made between the circuit simulation and the EM simulation. And they are in good agreement. The response exhibits a bandstop response at 19.6 GHz. Thus, the derived equivalent circuit for the EBG structure can be used accurately to design practical circuits.

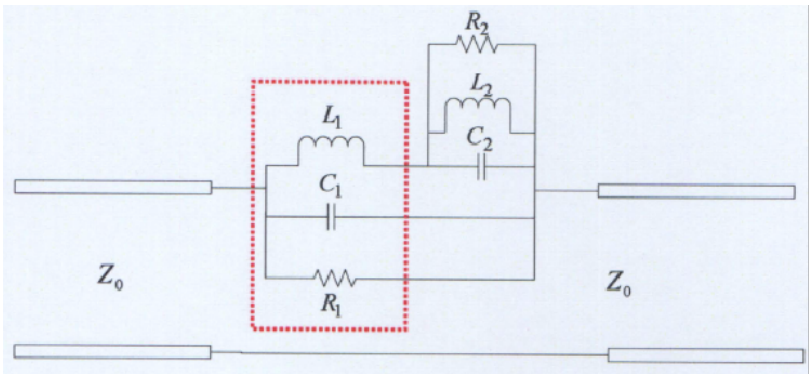


Fig. 5-16. Equivalent circuit model of the unit reconfigurable cell structure.

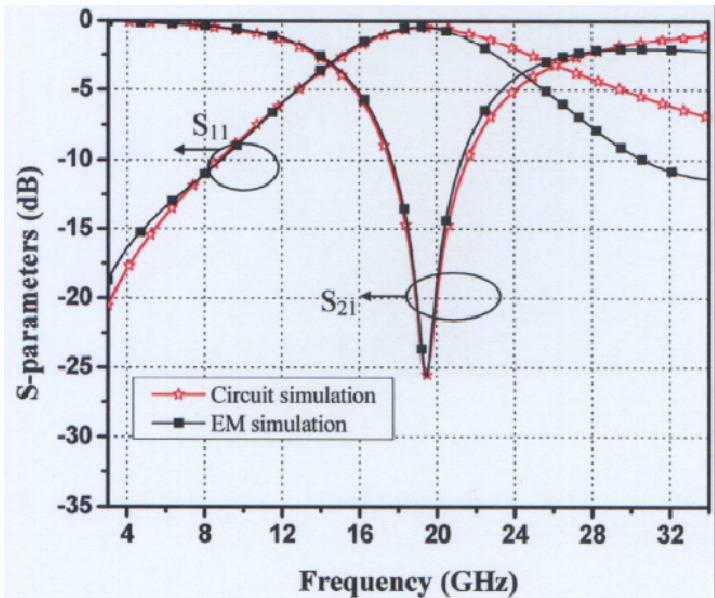


Fig. 5-17 Comparison of parameter extraction and EM simulation results of the unit reconfigurable cell (dotted line).

Table 5-3 Extracted circuit parameters of the reconfigurable filter

Parameters	$d_s = 60\ \mu\text{m}$ , $w_s = 200\ \mu\text{m}$
Smaller square size, $a\ (\mu\text{m})$	762
Bigger square size, $b\ (\mu\text{m})$	1200
Resonant frequency (GHz)	17.34
Inductance, $L_1\ (\text{nH})$	0.54
Inductance, $L_2\ (\text{nH})$	1.00
Capacitance, $C_1\ (\text{pF})$	0.13
Capacitance, $C_2\ (\text{pF})$	0.21
Resistance, $R_1\ (\text{K}\ \Omega)$	1.8
Resistance, $R_2\ (\text{K}\ \Omega)$	2.0

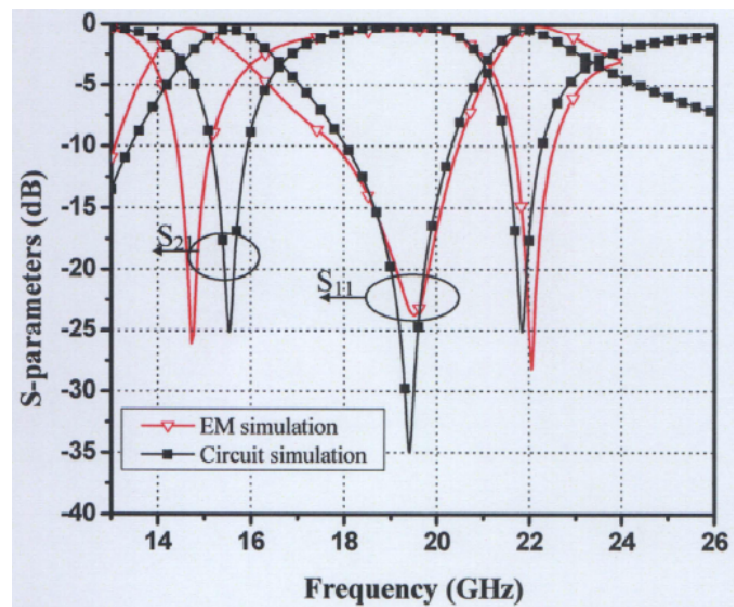
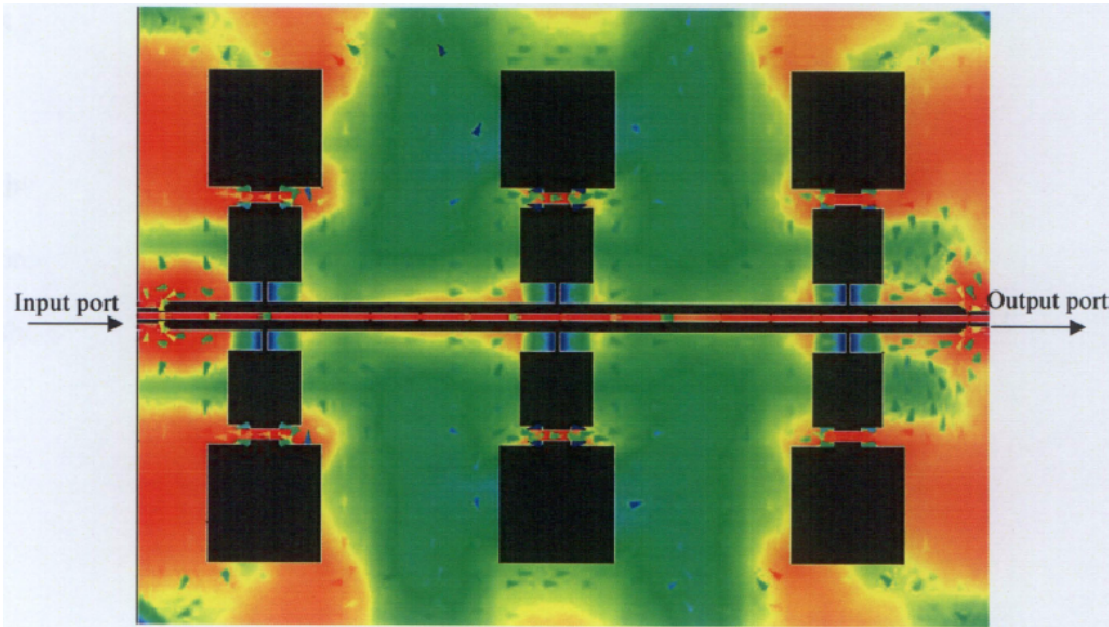


Fig. 5-18 Comparison of circuit and EM simulation results of the unit reconfigurable cell.

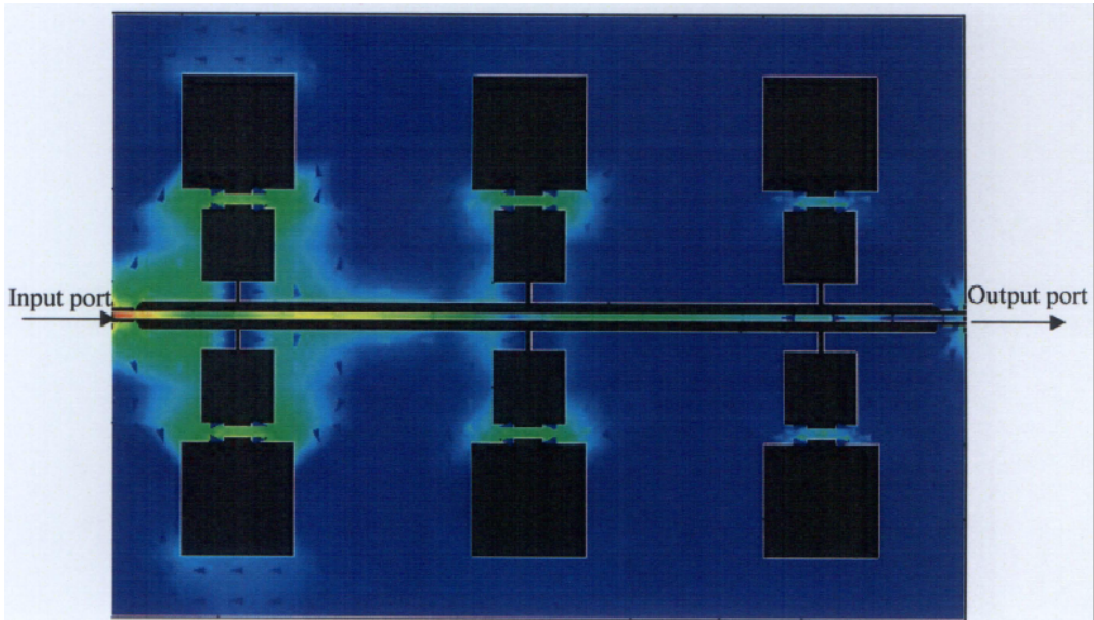
The whole unit cell structure which includes both the smaller and the bigger square slots is now discussed. Both the circuit and EM simulations shown in Fig. 5-18 demonstrate a bandpass characteristic at the same frequency of 19.6 GHz. From the circuit model it can deduced that, when another capacitor  $C_2$  is added in parallel with an inductor  $L_2$ , the bandpass response is obtained. The performance of the bandpass response improves when the relative size of the bigger square slot with respect to that of the smaller square slot is increased, in other words  $L_2$  increased and the transverse slot  $C_2$  changes slightly. Therefore, under these circumstances two transmission zeros would occur at 15.2 GHz and 22 GHz. Figure 5-19 shows the current distribution of the reconfigurable filter. For the bandpass state, all the signals are passing through the transmission line as shown in Fig 5-19 (a). For the bandstop state, the energy is totally attenuated at the resonant frequency as shown in Fig. 5-19 (b).



Chapter 5 Micromachined Tunable Bandpass Filters



(a)

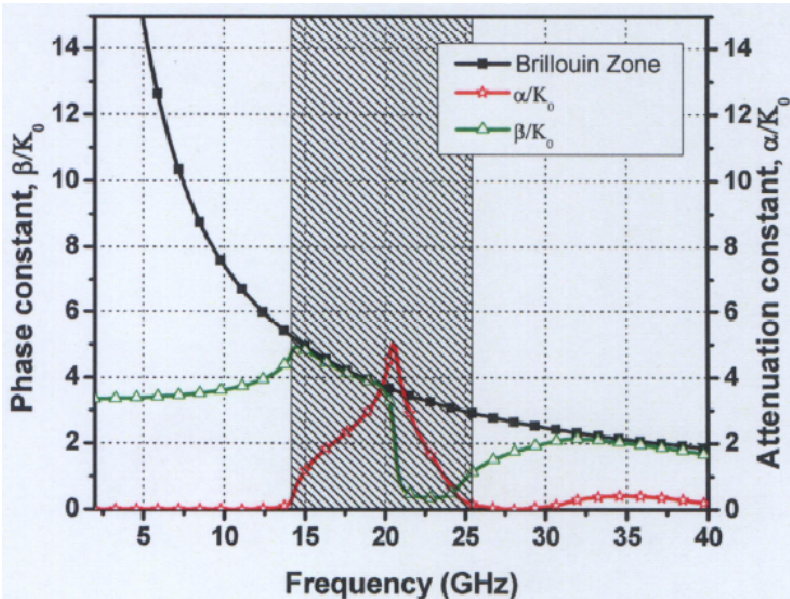


(b)

Fig. 5-19 Simulation results of the current distribution for reconfigurable filter; (a) Bandpass response, (b) Bandstop response.

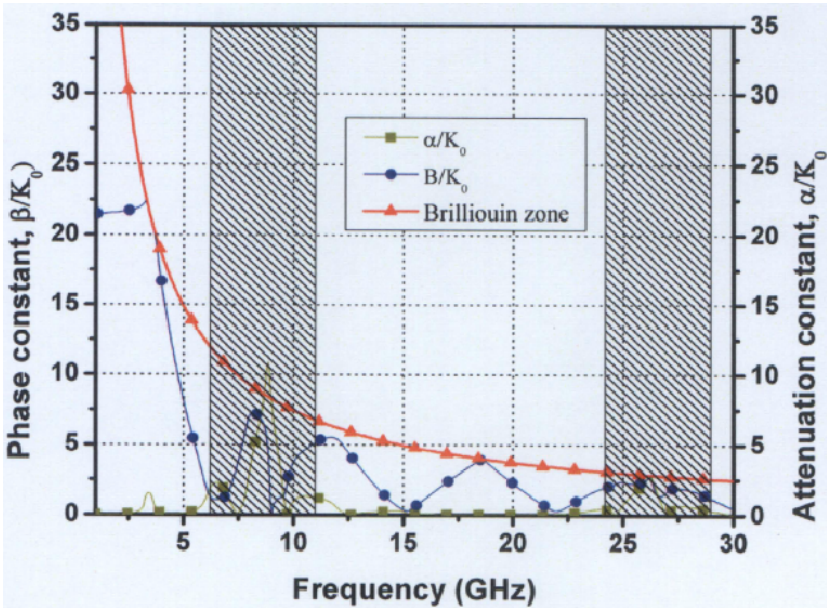
5.2.1.2 Propagation characteristics of the unit EBG cell

Fig. 5-20 (a) and (b) shows the dispersion diagram of the EBG with the smaller and the inclusion of the bigger slot respectively. Fig. 5-20 (a) shows the typical bandstop propagation characteristics whereas, Fig 5-20 (b) validates that the periodic structure has shown the bandpass behavior at the same frequency of the bandgap.



(a)





(b)

Fig. 5-20 Simulated dispersion characteristics of unit cell structure; (a) Bandstop filter phenomena; (b) Bandpass filter phenomena.

The curve starts to follow a Brillouin zone boundary at 3 GHz. From the simulation results of the unit cell, the bandgap occurs at 8.5 GHz. The attenuation curve indicates a normalized absolute value of 12. After that the curves start to fall when the bandpass phenomenon is approaching. The attenuation value of the bandpass filter is zero at the central frequency of 18 GHz. The attenuation curve starts to rise again when it approaches the second pole. However, it has absolute value of 4 due to the low rejection level in the second pole. The phase response rises fast due to the bandgap at 4 GHz, and then it fluctuates within the bandgap and the bandpass regions. Fig. 5-21 shows the phase response of the reconfigurable filter, which is linear in the bandpass and bandstop region respectively.

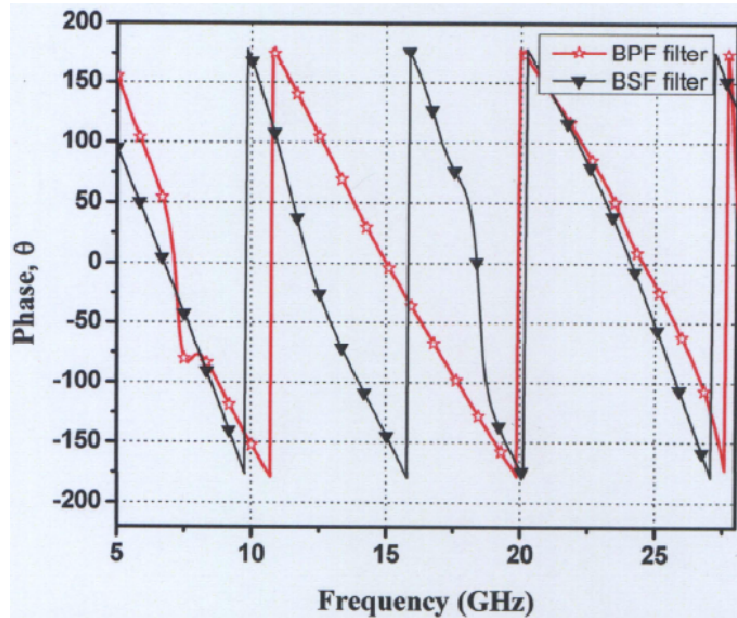
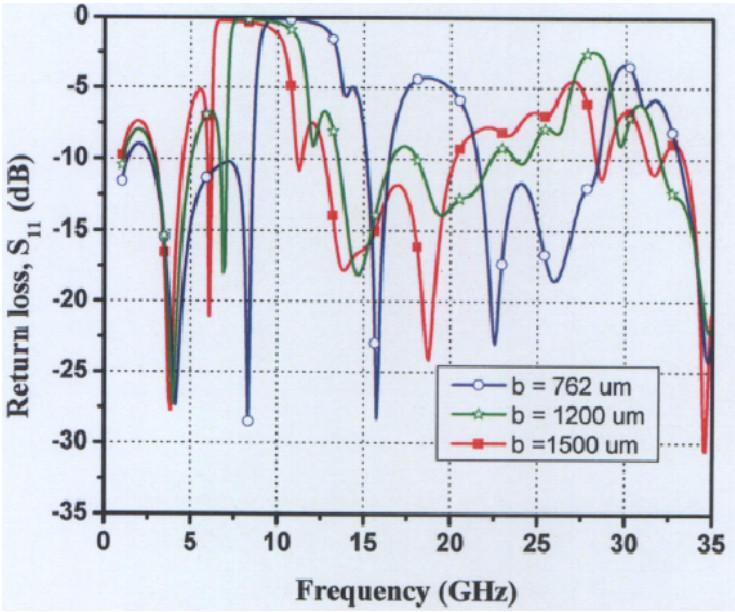


Fig. 5-21 Simulated phase response of the reconfigurable filter.

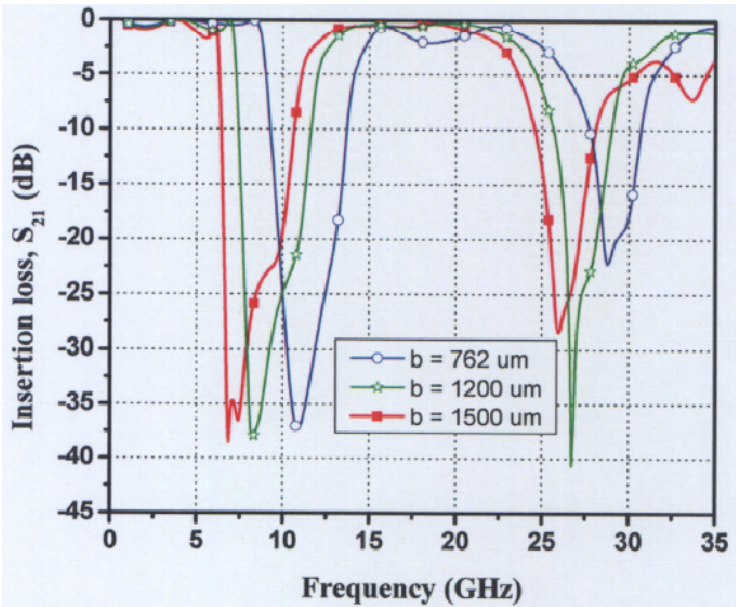
### 5.2.1.3 Effect of the bigger slot width $b$

In this subsection, the dimension of the bigger slot is varied. From the equivalent circuit, the change in the dimensions will affect the inductance  $L_2$  value. The change in the inductance will shift the resonant frequency. The inductance  $L_2$  changes when the dimension  $b$  is varied from  $762\ \mu\text{m}$ ,  $1200\ \mu\text{m}$  and  $1500\ \mu\text{m}$ . The simulation results are shown in Fig. 5-22 (a) and (b). The change in inductance will affect the return loss and the transmission curve. When the slot width is  $762\ \mu\text{m}$ , the resonant frequency is  $20.33\ \text{GHz}$ . Ripples are observed and the rejection level in the 2<sup>nd</sup> zero is less than 21 dB. The inductance value using the equivalent circuit is  $0.45\ \text{nH}$  and the other parameters remain constant. The bigger slot value is increased from  $1200\ \mu\text{m}$  to  $1500\ \mu\text{m}$ . The results indicate that when the value of the inductance  $L_2$  is  $1\ \text{nH}$ , the filter resonates at the centre frequency of  $17.43\ \text{GHz}$ .

Chapter 5 Micromachined Tunable Bandpass Filters



(a)



(b)

Fig. 5-22 Simulation results showing the influence of the change in the bigger slot width

$b$  (a) Return loss  $S_{11}$  and (b) Insertion loss  $S_{21}$ .

Chapter 5 Micromachined Tunable Bandpass Filters

The insertion loss curve,  $S_{21}$  is smooth in the passband region and shows rejection greater than 35 dB on the upper and lower sides of the passband. The extracted parameters of the filter are listed in Table 5-4.

Table 5-4 Extracted parameters of the variation in the bigger slot width  $b$

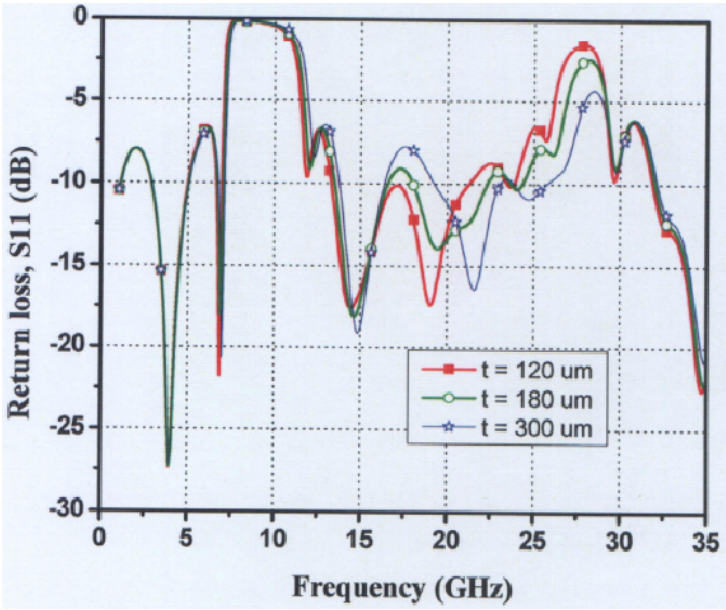
Variation in bigger slot width $b$ ( $\mu\text{m}$ )	762	1200	1500
Variable inductance $L_2$ (nH)	0.45	1	1.9
Resonant Frequency (GHz)	20.33	17.43	16.12
Inductance $L_1$ (nH)	0.54	0.54	0.54
Fixed Capacitance, $C_1$ (pF)	0.13	0.13	0.13
Resistance, $R_1$ (K $\Omega$ )	1.85	1.80	1.82
Fixed Capacitance $C_2$ (pF)	0.21	0.21	0.21
Resistance, $R_2$ (K $\Omega$ )	2	2.1	2.1

5.2.1.4 Effect of the transverse slot width  $t$

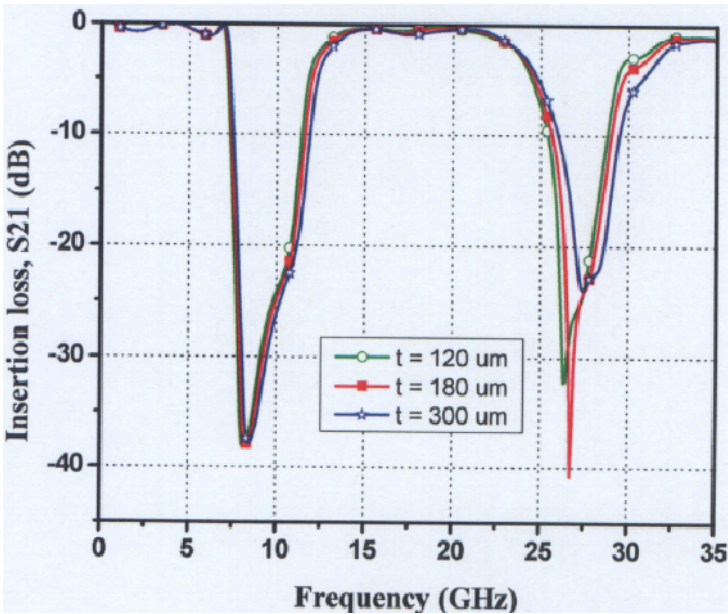
From the equivalent circuit, it is noted that when the transverse slot width  $t$  is changed, it will affect the capacitance of the filter. The change in width will affect the resonant frequency. The shift in resonance frequency is less compared to the case when the inductance is changed. The width is changed from 120  $\mu\text{m}$  to 300  $\mu\text{m}$ . The effective change in capacitance is 0.18 pF to 0.27 pF. The simulation results in Fig. 5-23 (a) show that for a width of 120  $\mu\text{m}$  the return loss  $S_{11}$  is less than -10 dB at the resonant frequency and ripples are observed in the passband.



Chapter 5 Micromachined Tunable Bandpass Filters



(a)



(b)

Fig. 5-23 Simulation results showing the effect of the change in the transverse slot width  $t$

(a) Return loss  $S_{11}$  and , (b) Insertion loss  $S_{21}$ .

Chapter 5 Micromachined Tunable Bandpass Filters

The optimum result occurs at 180  $\mu\text{m}$  when the rejection on both sides of the passband is greater than 35 dB and the insertion loss in passband is minimum. The parameter values of the inductance, capacitance and resistance are listed in Table 5-5.

Table 5-5 Extracted parameters of the variation of the transverse slot  $t$

Variation of transverse slot $t$ ( $\mu\text{m}$ )	120	180	300
Variable Capacitance $C_2$ (pF)	0.16	0.21	0.26
Resonant Frequency (GHz)	17.2	17.43	17.62
Inductance $L_1$ (nH)	0.54	0.54	0.54
Fixed Capacitance $C_1$ (pF)	0.13	0.13	0.13
Resistance $R_1$ (K $\Omega$ )	1.85	1.80	1.82
Fixed Inductance $L_2$ (nH)	1.00	1.00	1.00
Resistance $R_2$ (pF)	2.00	2.1	2.10

5.2.2 Experimental results and discussions

The RF performance of the reconfigurable filter is measured using the HP 8510C vector network analyzer with gold tip and with a 150  $\mu\text{m}$  pitch for the cascade microtech ground-signal-ground coplanar probes. The system is calibrated using standard short-open-load-through (SOLT) on wafer calibration technique. A 5-mm thick plastic plate is

Chapter 5 Micromachined Tunable Bandpass Filters

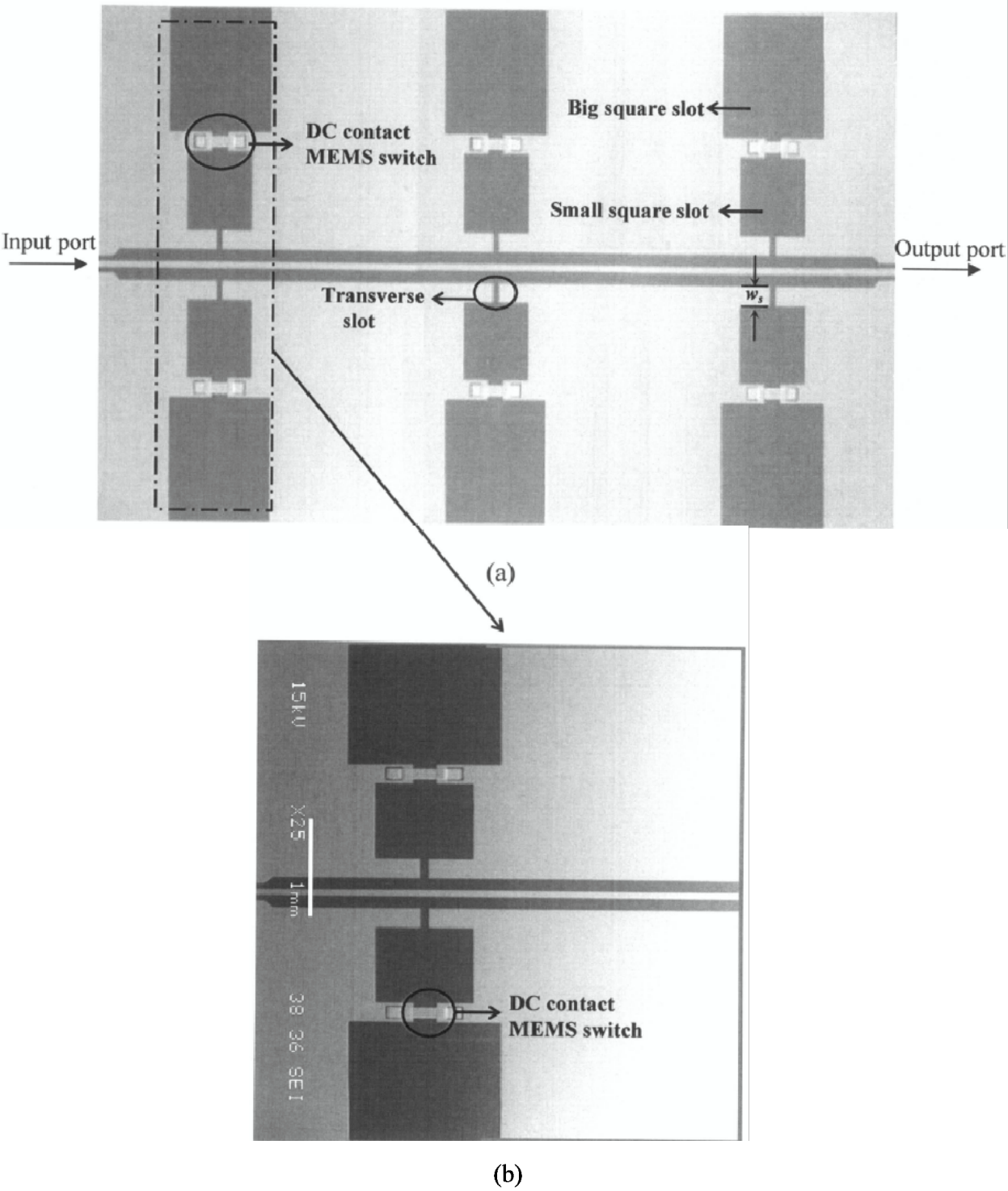


Fig. 5-24 SEM graph of the reconfigurable filter with MEMS switches, (a) Overview of the reconfigurable filter, and (b) Magnified image of the region with rectangular highlighted in (a).



Chapter 5 Micromachined Tunable Bandpass Filters

placed between the probe chuck and the sample to remove higher order mode propagation. All experiments are performed in the room temperature environment without any packaging. The reconfigurable filter is fabricated using gold material. The reconfigurable filter structure with DC contact MEMS switches is fabricated for a 50 Ω CPW transmission line with a signal line width of  $W = 70\text{ }\mu\text{m}$  and the gap width  $G = 115\text{ }\mu\text{m}$  as shown in Fig. 5-24 (a). The values of  $a$ ,  $b$ ,  $w_s$ , and  $d_s$  of the filter are presented in Table 5-3. The zoom view of the part of the switch of the reconfigurable filter is shown in Fig 5-24 (b). In order to show the validity of the equivalent circuit and the extracted parameters for the proposed unit cell, the reconfigurable filter is formed by cascading three unit cells with the DC contact MEMS switches  $C_s$  placed at the transverse slot as shown in Fig. 5-25.

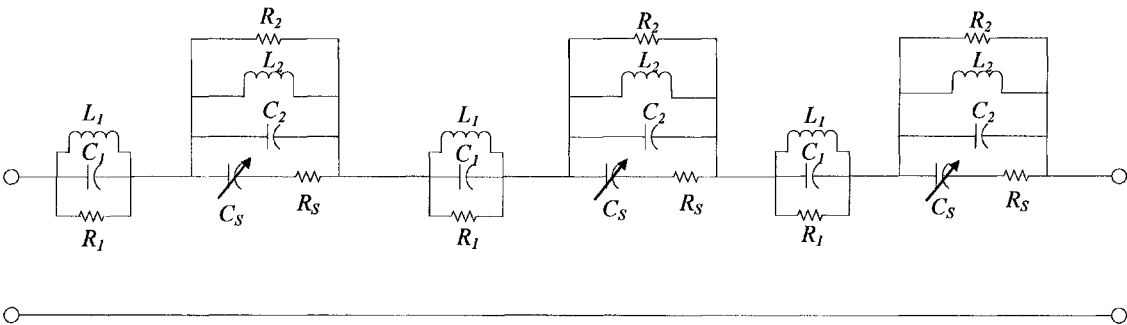


Fig. 5-25 The equivalent circuit of the reconfigurable filter.

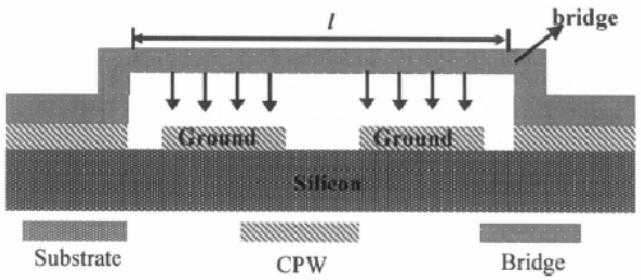
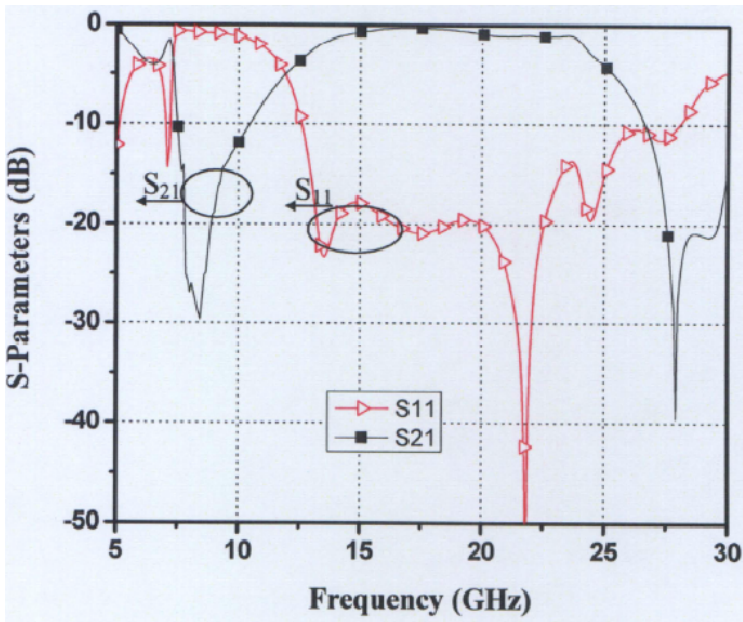
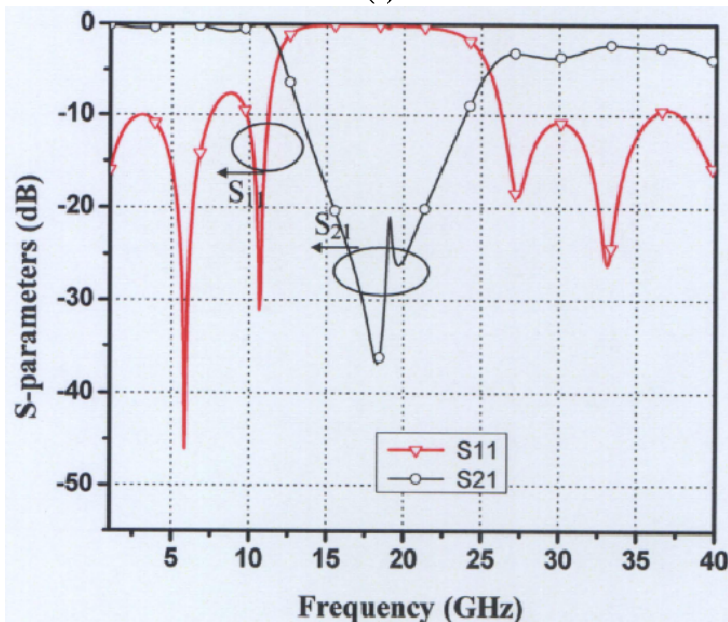


Fig. 5-26 Cross section of the MEMS DC contact switch.

Chapter 5 Micromachined Tunable Bandpass Filters



(a)



(b)

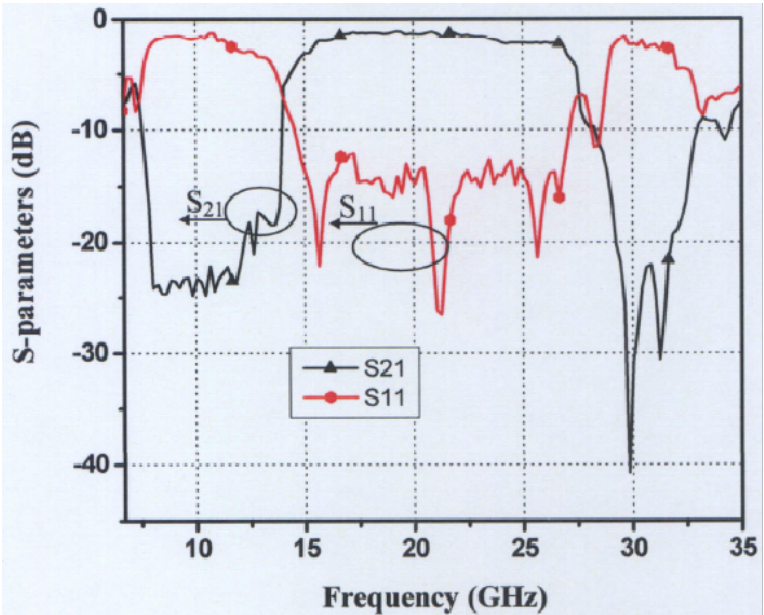
Fig. 5-27 Simulation results of the S-parameters of the reconfigurable filter (a) OFF state of switch, reconfigurable filter behaves as a bandpass filter and (b) ON state of switch, reconfigurable filter behaves as a bandstop filter.

### *Chapter 5 Micromachined Tunable Bandpass Filters*

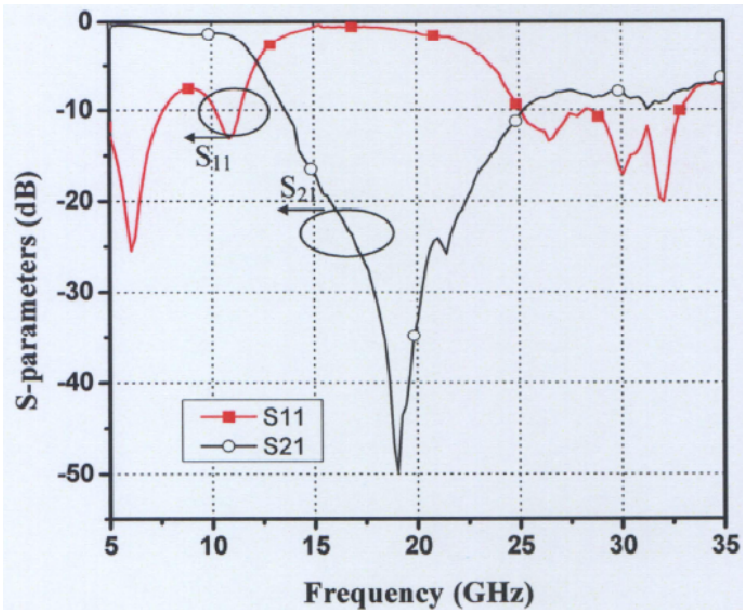
---

Figure 5-26 shows the cross section view of the switch. The width and the length of the bridges are  $50\text{ }\mu\text{m}$  and  $300\text{ }\mu\text{m}$ . The height of the switches is  $2\text{ }\mu\text{m}$ . The extracted values of the MEMS switch are  $C_s=50\text{fF}$ , and  $R_s=1\text{ }\Omega$ . The bias lines are designed for providing the DC voltage with a resistance of  $1000\text{ }\Omega$ . When the DC contact MEMS switches are up i.e. in the OFF state, the filter behaves like a bandpass filter while when they are down i.e. ON- state, the filter behaves like a bandstop filter. The simulation result of the reconfigurable filter are shown in Fig. 5-27. It has an insertion loss of  $0.9\text{ dB}$  at  $19.8\text{ GHz}$  and the  $3\text{-dB}$  bandwidth is  $9.6\text{ GHz}$ . The bandstop filter has an insertion loss of  $0.6\text{ dB}$ . The measurement results of the reconfigurable filter is shown in Fig. 5-28. When the DC contact MEMS switches are at the up-state i.e. not shortened, then the filter provides the function of the bandpass filter with the insertion loss of  $1.55\text{ dB}$  at  $20.1\text{ GHz}$ . The  $3\text{-dB}$  bandwidth is  $9.2\text{ GHz}$  and rejection is greater than  $20\text{ dB}$ . When the DC contact MEMS switches are at the down-state with applied DC bias voltage of  $38\text{ volts}$ , the top transverse slot and bigger square slot,  $b$  are shortened to ground, and it provides the function of the bandstop filter. The measurement results show that the resonant frequency of the bandstop is  $19.8\text{ GHz}$  and the insertion loss is  $1.2\text{ dB}$ . The  $20\text{-dB}$  rejection bandwidth changes from  $17\text{ GHz}$  to  $22.5\text{ GHz}$ . The simulation and measurement results are in good agreement.

Chapter 5 Micromachined Tunable Bandpass Filters



(a)



(b)

Fig. 5-28 Measurement results of S-parameters of the reconfigurable filter (a) OFF state of switch, reconfigurable filter behaves as a bandpass filter and (b) ON state of switch, reconfigurable filter behaves as a bandstop filter.

### 5.3 Summary

The Fabry-Perot tunable bandpass filter is designed, fabricated and experimented in this chapter. The F-P filter is realized by creating a defect cavity in the EBG periodic structures. A mathematical model is developed for the determination of the Q factor of the filter. Similarly, equations are also derived for the bandpass and bandstop phenomena of the EBG structures. The measurement result of the F-P filter shows a quality factor Q of 70 with an insertion loss of 4.0 dB. The capacitive MEMS switches are fabricated at the defect cavity to develop a tunable filter. The switch heights are varied with the bias voltage from 0 ~ 34 volts, and the resonant frequency is tuned. The result shows a tuning range of 7.5% with an insertion loss that varies from 4.1 to 7.35 dB.

The micromachined switching reconfigurable bandpass and bandstop filter is also designed in this chapter. An equivalent circuit model is derived for the reconfigurable circuit. The extracted parameters show both bandpass and bandstop characteristics. The dispersion characteristics are obtained to analyze the electromagnetic wave behavior within the unit cell of the bandpass filter and the bandstop filter using Floquet's theorem. The measurement results of the reconfigurable filter show that the insertion loss is 1.55 dB for the bandpass filter whereas the band rejection level is > 20 dB and the insertion loss in the passband is 1.2 dB for the bandstop filter. The micromachined reconfigurable filter is the first in the world that demonstrates bandpass and bandstop functions which can be switched at the same frequency.

## CHAPTER 6

### CONCLUSIONS

#### 6.1 Conclusions

In this thesis, the research focuses on the innovation of designing high performance tunable filters using electromagnetic bandgap structures (EBG) with micromachined switches. The design and fabrication of the CPW and MEMS capacitive switch are first investigated. Different parameters of the CPW structure are analyzed to realize an optimum design. Different metal properties and their influence on CPW structure are also examined. An electrical and a mechanical design of the micromachined switch are investigated in detail. The micromachined switch is fabricated using surface micromachining process. A new planarization method is developed to improve the isolation of the switch. The measurement results show that the contact area between the bridge and the dielectric layer is remarkably improved by 63%, and the isolation of the switch is improved by 2.2 dB at 15 GHz (29.3%) and 10 dB at 40 GHz (58.8%). The insertion loss of the switch is 0.1 dB at 15 GHz. The switch is able to meet the specifications in terms of the insertion loss  $< 0.3$  dB and return loss  $> 10$  dB.

A new fixed and tunable bandstop filter using unloaded and loaded EBG structures is developed. The frequency characteristics of the unit cells are studied. The dispersion diagram, which is a graphical representation of the dispersion relation for the periodic structures, is used to describe the propagation characteristics in the unit EBG cells. The extracted parameters show that the bandgap effect of the EBG cells which can be



accurately interpreted using circuit analysis theory. The new tunable filter is realized by loading MEMS capacitive bridges on the EBG bandstop filter. These bridges act as variable capacitors and are driven by externally applied control bias voltage. An equivalent circuit model is developed where its parameter values are extracted. The measurement results of the tunable bandstop filter show a tuning range from 19 GHz to 17.3 GHz. The insertion loss varies from 0.7 dB to 2.2 dB and meets the goal for the tunable bandstop filter design.

The Fabry-Perot bandpass filter is developed by creating a defect cavity in the EBG periodic structures. Its mathematical model is developed for the determination of the Q factor of the filter. The measurement result of the F-P filter shows a quality factor Q of 70 with an insertion loss of 4.0 dB. The capacitive MEMS switches are fabricated at the defect cavity to develop a tunable filter. The bridge gap heights are controlled by varying the bias voltage from 0 ~ 34 volts, and as a result the resonant frequency is tuned. The result shows the tuning range of 7.5% with an insertion loss which varies from 4.1 to 7.35 dB. The micromachined switching reconfigurable bandpass and bandstop filter is also developed. An equivalent circuit model is derived for the reconfigurable circuit. The extracted parameters show both bandpass and bandstop characteristics at the same frequency. The measurement results of the reconfigurable filter show that the insertion loss is 1.55 dB for the bandpass filter whereas the band rejection level is > 20 dB and the insertion loss in the passband is 1.2 dB for the bandstop filter. The micromachined reconfigurable filter is the first in the world that demonstrates bandpass and bandstop functions which can be switched at the same frequency. The insertion loss for F-P filter is slightly higher than specification, while others parameters like return loss, tuning range



and switching voltage meet the design specifications. The micromachined switch and the tunable filters developed have potential applications in the future wireless front end systems.

## 6.2 Recommendations

The thesis focuses on the innovation of micromachined tunable filters using EBG and the micromachined switches. The design, simulation and fabrication are discussed. Based on the current work, some recommendations are provided to improve the design and optimize the performance of the filters.

First, the improvement of the Q factor and the reduction of the insertion loss of the filters can be made possible by designing the filters on a less lossy dielectric substrate. Thick metallic deposition and a more compact design can further reduce the conductor loss of the filters.

Second, the EBG filters designed in the thesis are simulated using the commercial software's Zeland IE-3D and Agilent's ADS. The simulations and measurement results shown good agreement and the investigations are justified. However, analytical technique can also be used to examine the complex geometries of the EBG structures. The eigenvalue equation can be obtained for the EBG by Fourier series.

Third, the tuning range of the filters can be enhanced by varying the inductance rather than capacitance using MEMS switches as metal to metal switches rather than as capacitive varactors.

Finally, further research can be conducted to improve the mechanical performance of the micromachined switches.

## **Bibliography**

- [1] H. J. D. Santos. *Introduction to microelectromechanical (MEMS) microwave systems*, Norwood, MA: Artech House, 1999.
- [2] H. J. D. Santos, “MEMS-A wireless vision,” in *Proc. Int. MEMS workshop*, Singapore, 2001.
- [3] G. M. Rebeiz, *RF MEMS — Theory, Design, and Technology*, John Wiley & Sons, First Edition, June 15, 2002.
- [4] N. S. Barker, “Distributed MEMS transmission line,” Ph.D dissertation, EECS, Dept. Uni. Michigan. Ann Arbor, MI, 1999.
- [5] H. J. D. Santos. *Introduction to microelectromechanical (MEMS) microwave systems*, 2<sup>nd</sup> edit. Norwood, MA: Artech House, 2004.
- [6] S.D. Senturia, *Microsystem Design*, Kluwer Academic Publishers, Boston, 2001.
- [7] H. A. C Tilman, “MEMS components for wireless communications,” *16<sup>th</sup> European conference on solid state transducers*, Sept. 15-18, Prague, pp. 1-34, 2002.
- [8] J. J. Yao and M. F. Chang, “A surface micromachined miniature switch for telecommunications applications with signal frequencies from DC up to 4 GHz,” in *Int. Conf. Solid-State Sens. Actuators Dig.*, Stockholm, Sweden, pp. 384–387, June 1996.
- [9] C. L. Goldsmith, Z. Yao, S. Eshelman, and D. Denniston, “Performance of low-loss RF MEMS capacitive switches,” *IEEE Microwave Guided Wave Lett.*, vol. 8, pp. 269–271, Aug. 1998.

## Bibliography

---

- [10] C. Goldsmith, J. Randall, S. Eshelman, T. H. Lin, D. Denniston, S. Chen, and B. Norvell, "Characteristics of micromachined switches at microwave frequencies," in *IEEE MTT-S Int. Microwave Symp. Dig.*, San Francisco, CA, pp. 1141–1144, June 1996.
- [11] Z. J. Yao, S. Chen, S. Eshelman, D. Denniston, and C. Goldsmith, "Micromachined Low-Loss Microwave Switches," *IEEE Journal of Microelectromechanical Systems*, vol. 8, pp. 129–134, June 1999.
- [12] Robert E. Collin, *Foundations for microwave engineering*, Mc Graw-Hill, 1992.
- [13] David M. Pozar, *Microwave engineering*, John Wiley & Sons, 1998.
- [14] G. L. Matthaei, L. Yong, and E. M. T. Jones, *Microwave Filters, Impedance-Matching Networks, and Coupling Structures*, New York: McGraw-Hill, 1964.
- [15] Y. Ishikawa, T. Nishikawa, T. Okada, S. Shinmura, "Mechincally tunable MSW bandpass filter with combined magnetic units, " in *IEEE-MTT-S Int. Microwave Symp. Dig.*, pp. 143–146, 1990.
- [16] W. J. Keane, "YIG filters aid wide open receivers," *Microwave J.*, vol. 17, no. 8, Sep. 1980.
- [17] S. R. Chandler, I. C. Hunter, and J. C. Gardiner, "Active varactor tunable bandpass filters," *IEEE Microw. Guided Wave Lett.*, vol. 3, no. 3, pp. 70–71, Mar. 1993.
- [18] A. R. Brown and G. M. Rebeiz, "A varactor-tuned RF filter," *IEEE Trans. Microw. Theory Tech.*, vol. 48, no. 7, pp. 1157–1160, Jul. 2000.
- [19] L. Brillouin, *Wave propagation in periodic structures*, 2<sup>nd</sup> ed. Dover Publications, Inc. New York, 1953.

- [20] D. Sievenpiper, L. Zhang, R. F. J. Broas, N. G. Alexopolous and E. Yablonovitch, "High impedance electromagnetic surface with a forbidden frequency band," *IEEE Trans. Microwave Theory. Tech.*, vol. 47, no. 11, pp. 2059, 2074, Nov 1999.
- [21] A. Bayers, I. Rumsey, Z. Popvic, and M-P. May, "Surface wave guiding using periodic structures," *IEEE –APS Dig.*, vol. 1, pp. 342-345, 2000.
- [22] D. Sivenpiper, and E. Yablonovitch, "Eliminating surface currents with metallodielectric photonics crystal," *IEEE-MTT-S Int. Microwave Sym. Dig.*, vol. 1, pp. 663- 666, 1998.
- [23] N. C. Karmakar, "Improved performance of photonic bandgap microstripline structures using chebyshev distribution," *Microwave and Optical Technology Letter*, vol. 33, no. 1, pp. 1-5, April 2002.
- [24] V. Radisic, Y. Qian, R. Coccioli, and T. Itoh, "A novel 2-D photonic bandgap structures for microstrip lines", *IEEE Microwave and Guide Wave Lett.*, vol. 8, pp. 66-71, Feb. 1998.
- [25] B. Elamaram, I. M. Chio, L.Y. Chen and J. C. Chiao, "A beam-steerer using reconfigurable PBG ground plane," *IEEE MTT-S Int. Microwave Symp. Dig.*, pp. 835 –838, 2000.
- [26] I. Chang and B. Lee, "Design of defected ground structures for harmonic control of active microstrip antenna," *IEEE AP-S Int. Symp. Dig.*, pp. 852-855, 2002.
- [27] N. C. Karmakar, M. N. Mollah, "Investigations into nonuniform photonic-bandgap microstripline low-pass filters," *IEEE Trans. Microwave Theory Tech.*, vol. 51, pp. 564-572, Feb. 2003.

## Bibliography

---

- [28] L. E. Larson, R. H. Hackett, M. A. Melendes, and R. F. Lohr, "Micromachined microwave actuator (MIMAC) technology- a new tuning approach for microwave integrated circuits," in *Millimeter-wave monolithic circuits Symp. Dig.*, Boston, MA, pp. 27-30, June 1991.
- [29] J. Y. Park, G.H. Kim, K.W. Chung, and J.U. Bu, "Fully integrated micromachined capacitive switches for RF applications", *IEEE MTT-S International Microwave Symposium Digest*, Boston, MA, pp. 283-286, 2000.
- [30] K. E. Petersen, "Micromechanical membrane switches on silicon," *IBM Journal of Research and Development*, vol. 23, pp. 376-385, July 1971.
- [31] J. J. Yao, and M. F. Chang, "A surface micromachined miniature switch for telecommunications applications with signal frequencies from DC up to 4 GHz," in *Intl. Conf. Solid State Sens. Actuators Dig.*, Stockholm, Sweden, pp. 384-387, June 1996.
- [32] S. Pacheco, C. T. Nguyen, and L. P. B. Katehi, "Design of low actuation voltage RF MEMS switch," *IEEE MTT-S International Microwave Symposium Digest*, Boston, MA, pp. 165-168, June 2000.
- [33] N. S. Barker, and G. M. Rebeiz, "Distributed MEMS true time delay phase shifters and wideband switches," *IEEE Trans. Microwave Theory. Tech.*, vol. 46, no. 11, pp. 1881-1890, 1998.
- [34] D. Peroulis, S. Pacheco, and L. P. B. Katehi, "MEMS devices for high isolation switching and tunable filtering," *IEEE MTT-S International Microwave Symposium Digest*, Boston, MA, pp. 1217-1220, June 2000.

## Bibliography

---

- [35] L. Dussopt and G. M. Rebeiz, "Intermodulation distortion and power handling in RF MEMS switches, varactors and tunable filters," *IEEE Trans. Microw. Theory Tech.*, vol. 51, no. 4, pp. 1247–1256, Apr. 2003.
- [36] J.B. Muldavin and G.M. Rebeiz, "High isolation CPW MEMS shunt switches", *IEEE Microwave Theory Tech*, vol. 48, pp. 1045–1056, 2000.
- [37] J. B. Muldavin, and G. M. Rebeiz, " Inline capacitive and DC contact MEMS shunt switches," *IEEE Microwave Wireless Comp. Letters*, vol. 11, no. 8, pp. 334-336, 2001.
- [38] G. L. Tan, and G. M. Rebeiz, "A DC contact MEMS shunt switch, " *IEEE Microwave Wireless Comp. Letters* , vol. 12, no. 6, pp. 212-214, 2002
- [39] J. B. Muldavin, and G. M. Rebeiz, " All metal series and series/shunt MEMS switches," *IEEE Microwave Wireless Comp. Letters*, vol. 11, no. 9, pp. 373-375, 2001.
- [40] J. B. Muldavin, "Design and analysis of series and shunt MEMS switches," Ph.D. dissertation, Dept. Elect. Eng. & Comput. Sc., Univ. of Michigan at Ann Arbor, Ann Arbor, MI, US, 2001.
- [41] J. B. Muldavin and G. M. Rebeiz, "High isolation CPW MEMS shunt switches-part 1: Modeling," *IEEE Trans. Microwave Theory. Tech.*, vol. 48, no. 6, pp. 1045-1052, June 2000.
- [42] J. B. Muldavin and G. M. Rebeiz, "High isolation CPW MEMS shunt switches-part 2: Design," *IEEE Trans. Microwave Theory. Tech.*, vol. 48, no. 6, pp. 1053-1056, June 2000.

*Bibliography*

---

- [43] J. Rizk, G. L. Tan, J. B. Muldavin, and G. M. Rebeiz, “ High isolation W-band MEMS switches,” *IEEE- Microwave Wireless Comp. Lett.*, vol. 11, no.1, pp. 10-12, Jan. 2001.
- [44] D. Hyman, A. Schmitz, B. Warneke, T. Y. Hsu and J. Lam, “ GaAs- compatible surface micromachined RF MEMS switches,” *IEE Electronics Letters*, vol. 3, pp. 224-226, Feb. 1999.
- [45] G. L. Tan, and G. M. Rebeiz, “DC-26 GHz MEMS series- shunt switch absorptive switches,” *IEEE-MTT-S Int. Microwave Sym. Dig.*, pp. 325-328, 2001.
- [46] G. L. Tan, High performance RF MEMS circuits and phase shifters, PhD thesis, University of Michigan, Ann Arbor, 2002.
- [47] S. D. Senturia, *Microsystem Design*, Kluwer Academic Publishers, Boston, 2001
- [48] Z. Chen, M. B. Yu, and L. H. Guo, “Design and Fabrication of RF MEMS Capacitive Switch on Silicon Substrate with Advanced IC Interconnect Technology”, 6<sup>th</sup> *International Conference on Solid-State and Integrated-Circuit Technology*, pp. 739-741, 2001.
- [49] J. S. G. Hong, and M. J. Lancaster, *Microstrip filters for RF/Microwave applications*, John Wiley & Sons, Inc. 2001.
- [50] A. R. Brown, “High Q integrated micromachined components for 28 GHz fornt end transceiver,” PhD thesis, Uni. of Michigan, 1999.
- [51] J. Uher, and W. J. R. Hoefer, “Tunable microwave and millimeter wave band pass filter,” *IEEE Trans. Microwave Theory & Tech.* , vol. 39, pp. 643-653, Sept. 1991.



## Bibliography

- 
- [52] K. Hettak, N. Dib, and A. F. Sheta, "A class of novel uniplanar series resonant and their implementation in original applications," *IEEE Trans. Microwave Theory & Tech.*, vol. 46, pp. 1270-1276, Sept. 1998.
  - [53] E. R. Brown, "RF MEMS switches for reconfigurable integrated circuits," *IEEE Trans. Microwave Theory. Tech.*, vol. 46, no. 11, pp. 1868-1880, Nov. 1998.
  - [54] J. Hyoun, H. T. Kim, Y. Kwon, and Y. K. kim, "Tunable millimeter wave using planar waveguide and micromachined variable capacitors," *Journal of Micromech. Microeng.*, vol. 11, pp. 706-712, 2001.
  - [55] Y. Liu, A. Borgioli, A. S. Nagra and Robert A. York, "Distributed MEMS Transmission Lines for Tunable Filter Applications," *Int. J. RF and Microwave Computer-Aided Eng.*, Special issue, pp. 254-259, 2001.
  - [56] E. Fourn, A. Pothier, C. Champeaux, and P. Blondy, "MEMS switchable interdigital coplanar filter," *IEEE Trans. Microwave Theory & Tech.*, vol. 51, pp. 320-324, Jan. 2003.
  - [57] A. A. Tamijani, L. Dussopt and G. M. Rebeiz, "Miniature and Tunable Filters Using MEMS Capacitors," *IEEE Trans. Microwave Theory Tech.*, vol. 51, pp. 1878-1885, July, 2003.
  - [58] G. Kraus, C. Goldsmith, C. Nordquist, and P. Finnegan, "A widely tunable RF MEMS end-coupled filter," *IEEE MTT-S Int. Microwave Symp. Dig.*, pp. 429-432, June 2004.
  - [59] J. Brank, Zh. J. Yao and M. Eberly et al, "RF MEMS-Based Tunable Filters," *Int. J. RF and Microwave Computer-Aided Eng.*, Special issue, pp. 276-283, 2001.

## Bibliography

---

- [60] R. D. Streeter, C. A. Hall, R. Wood, and R. Madadevan, "VHF high power tunable RF bandpass filter using microelectromechanical (MEMS) microrelays," *Int. J. RF Microwave*, vol. 11, No. 5, pp. 261-275, 2001.
- [61] R. Gonzalo, P. De Maagt and M. Sorolla, "Enhanced patch-antenna performance by suppressing surface waves using photonic bandgap substrates," *IEEE Trans. Microwave Theory Tech.*, vol. 47, pp. 2131–2138, Nov.1999.
- [62] T. Akaline, M. A. G. Laso, T. Lopetgi, and O. Vanbesien, "PBG type microstrip filters with one end and two sided patterns," *Microwave and Optical Tech. Lett.*, vol. 30, no.1, pp. 69-72, July 2001.
- [63] D. Nesic, and A. Nesic, "Bandstop microstrip PBG filter with sinusoidal variation of the characteristics impedance and without etching in the ground plane," *Microwave and Optical Tech. Lett.*, vol. 29, no. 6, pp. 418-420, June. 2001.
- [64] Q. Xue, K. M. Shum, and C. H. Chan, "Novel 1-D photonic bandgap microstrip transmission line," *IEEE –APS Dig.*, pp. 354-356, 2003.
- [65] Y. Qian, F. R. Yang, and I. Itoh, "Characteristic of microstrip lines on a uniplanar compact PBG ground plane," *Asia Pacific Microwave Conf. Dig.*, pp. 589-592, 1998.
- [66] M. Rahman, and M. A. Stuchly, "Transmission line periodic circuit representation of planar microwave photonic bandgap structures," *Microwave and Optical Tech. Lett.*, vol. 30, no. 1, pp. 15-19, July. 2001.
- [67] N. C. Karamakar, and M. N. Mollah, "Microstrip lines on annular ring photonic bandgap structures," *Microwave and Optical Tech. Lett.*, vol. 20, no. 6, pp. 431-433, March 2002.

## Bibliography

---

- [68] G. Zhang, N. Yuan, Y. Fu and C. Zhu, "A novel PBG structure for microstrip lines," in *Proc. International Conference on Microwave and Millimeter Wave Technology*, pp. 1040-1042, 2002.
- [69] Q. Xue, K. M. Shum, and C. H. Chan, "Novel 1-D microstrip PBG cells," *IEEE Microwave and Guide Wave Lett.*, vol. 10, pp. 403-405, Oct. 2000.
- [70] V. Radisic, Y. Qian, and I. Itoh, "Novel architectures for high efficiency amplifiers for wireless applications," *IEEE Trans. Microwave Theory. Tech.*, vol. 46, no. 11, pp. 1901-1909, Nov. 1998.
- [71] C. Y. Hang, W. R. Deal, Y. Qian, and I. Itoh, "High efficiency transmitter front end integrated with planar antennas and PBG," *Asia-Pacific microwave Conf.* Australia, 2000.
- [72] Y. Q. Fu, G. Zhang, and N. Yuan, "A novel PBG coplanar waveguide," *IEEE Microwave and Wireless Compon. Lett.*, vol. 11, pp. 447-449, Nov. 2001.
- [73] Q. Xue, K. M. Shum, and C. H. Chan, "Characteristics of a compact CPW resonant cell," *Microwave and Optical Tech. Lett.*, vol. 37, no. 6, pp. 408-410, June 2003.
- [74] H. Shigesawa, M. Tsjui, and A. A. Oliner, "Conductor backed slot line and coplanar waveguide: Dangers and full wave analysis," *IEEE-MTT-S Int. Microwave Sym. Dig.*, pp. 199-202, 1998.
- [75] Y. Qian, D. Sievebpiiper, V. Radisisc, Y. Yablonovitch, R. Coccioli, and I. Itoh, "Microstrip patch antenna using novel photnics bandgap structures," *Microwave Journal*, vol. 42, no. 1, pp. 66-76, Jan. 1999.

## Bibliography

---

- [76] R. Coccioli, F-R. Yang, K-P. Ma, and I. Itoh, "Aperture coupled patch antenna on UC-PBG substrate," *IEEE Trans. Microwave Theory. Tech.*, vol. 47, no. 11, pp. 2123-2130, Nov 1999.
- [77] R. Gonzalo, P. D. Maagt, and M. Sorolla, "Enhanced patch antenna performance by suppressing surface waves using photonics bandgap substrates," *IEEE Trans. Microwave Theory. Tech.*, vol. 47, no. 11, Nov 1999.
- [78] K. M. Shum, Q. Xue, C. H. Chan, and K. M. Luck, "Investigation of microstrip reflectary using photonic bandgap structures," *Microwave and Optical Tech. Lett.*, vol. 28, no.2, pp. 114-116, Jan. 2001.
- [79] E. R. Brown, C. D. Parker, and E. Yablonovitch, "Radiation properties of a planar patch antenna on photonics crystal substrate," *J. Opt. Soc. Amer. B.*, vol. 10, no. 2, pp. 404-407, Feb. 1993.
- [80] S. K. Sharma, and L. Shafai, "Enhanced performance of an aperture coupled rectangular microstrip antenna on a simplified unipolar compact photonic bandgap (UC-PBG) structures," *IEEE -APS Dig.*, pp. 498-501, 2001.
- [81] R. Him, and H. Y. D. Yang, "Surface waves and leaky waves in integrated circuit structures with planar dipole loading," *IEEE -APS Dig.*, vol. 1, pp. 346-349, 2000.
- [82] Y. Kown, "A 44 GHz monolithic waveguide plane wave amplifier with improved unit cell design," *IEEE Trans. Microwave Theory Tech.*, vol. 46, pp.1237 -1241, Sept. 1998.
- [83] M. Kim, "A rectangular TEM waveguide with photonic crystal walls for excitation of quasi-optical amplifiers," *IEEE MTT-S Int. Microwave Symp. Dig.*, pp. 543 -546, 1999.

## Bibliography

- 
- [84] F-R. Yang, K-P, Ma, Y. Qian, and I. Itoh, "A novel TEM waveguide using uniplanar compact photonic bandgap (UC-PBG) structures," *IEEE Trans. Microwave Theory. Tech.*, vol. 47, no. 11, pp. 2092-2098, Nov. 1999.
  - [85] L. Zhu, "Slow-wave and bandgap transmission characteristics of finite-periodic coplanar waveguide," in *Asia-Pacific Microwave Conf. Dig.*, pp. 1153-1156, 2002.
  - [86] F-R. Yang, Y. Qian, R. Coccioli, and I. Itoh, "A novel low loss slow wave microstrip structures," *IEEE Trans. Microwave Guided Wave Lett.*, vol. 8, no. 11, pp. 372-374, Nov. 1998.
  - [87] T. Y. Yun and K. Chang, "Uniplanar one-dimensional photonic- bandgap structures and resonators," *IEEE Trans. Microwave Theory Tech*, vol. 49, pp. 549-553, Mar. 2001.
  - [88] Y. Qian, R. Coccioli, F-R. Yang, and I. Itoh, "Passive and active components design using PBG," *Terahertz Electronics proceedings, IEEE sixth Int. Conf.*, pp. 42-45, 1998.
  - [89] M. L. Her, Y. Z. Wang, C. M. Chang, and K. Y. Lin, "Coplanar waveguide (CPW) defected ground plane structure (DGS) for bandpass filter applications," *Microwave and Optical Tech. Lett.*, vol. 42, pp. 331-334, August. 2004.
  - [90] C. S. Kim, J. S. Park, D. Ahn, and J. Lim, "A novel 1 –D periodic defected ground structure for planar circuits," *IEEE- Microwave Wireless Comp. Lett.*, vol. 10, no.4, pp. 131-133, April 2000.
  - [91] D. Ahn, J. S. Park, C. S. Kim, J. Kim, Y. Qian, and I. Itoh, "A design of low pass filter using novel microstrip defected ground structure," *IEEE Trans. Microwave Theory. Tech.*, vol. 49, no. 1, pp. 86-93, Jan. 2001.

## Bibliography

---

- [92] L. Garde, M. J. Yabar, and C. D. Rio, "Simple modeling of DGS to design 1D PBG low pass filter," *Microwave and Optical Tech. Lett.*, vol. 37, no. 3, pp. 228-232, May 2003.
- [93] H. W. Liu, Z. F. Li, and X. W. Sun, "A novel fractal defected ground structures and it application to the low pass filter," *Microwave and Optical Tech. Lett.*, vol. 39, no. 6, pp. 453-456, Dec. 2003.
- [94] K- C. Chen, C-k. Tzuang, Y. Qian, and I. Itoh, "Leaky properties of microstrip above the perforated ground plane," *IEEE-MTT-S Int. Microwave Sym. Dig.*, vol. 1, pp. 69-72, 1999.
- [95] R. Coccioli, and I. Itoh, "Design of photonic band gap substrates for surface waves suppressions," *IEEE-MTT-S Int. Microwave Sym. Dig.*, vol. 3, pp. 1259- 1262, 1998.
- [96] K-P. Ma, J. Kim, F-R. Yang, Y. Qian, and I. Itoh, "Leakage suppressions in stripline circuits using a 2D photonic band gap lattice," *IEEE-MTT-S Int. Microwave Sym. Dig.*, vol. 1, pp. 73-76, 1999.
- [97] F-R. Yang, K-P. Ma, Y. Qian, and I. Itoh, "A uniplanar compact photonic bandgap (UC-PBG) structure and its applications for microwave circuits," *IEEE Trans. Microwave Theory. Tech.*, vol. 47, no. 8, pp. 1508-1514, Aug. 1999.
- [98] N. C. Karmakar, and M. N. Mollah, "Harmonic suppression of a bandpass filter using Binomially distributed photonic bandgap structures," *IEEE –APS Dig. 2003*.
- [99] A. Griol, D. Mira, J. Marti, and J. L. Corral, "Harmonic suppression in microstrip multistage coupled ring bandpass filters using defected ground plane," *Microwave and Optical Tech. Lett.*, vol. 39, no. 5, pp. 351-354, Dec. 2003.

## Bibliography

---

- [100] F-R. Yang, Y. Qian, R. Coccioli, and I. Itoh, "A novel uniplanar compact PBG structures for filter and mixer applications," *IEEE-MTT-S Int. Microwave Sym. Dig.*, vol. 3, pp. 919-922, 1999.
- [101] H. Y. D. Yang, N. G. Alexopoulos, and E. Yablonovitch, "Photonic bandgap materials for high gain printed circuit antennas," *IEEE Trans. Antennas & Propagat.*, vol. 45, no. 1, pp. 185-187, Jan. 1997.
- [102] S. Y. Lin, and K. L. Wong, "A conical pattern annular ring microstrip antenna with a photonic bandgap ground plane," *Microwave and Optical Tech. Lett.*, vol. 30, no. 3, pp. 159-161, August 2001.
- [103] M. Qui, and S. He, "High directivity patch antenna with both photonic bandgap substrate and photonic band cover," *Microwave and Optical Tech. Lett.*, vol. 30, no.1, pp. 41-44, July, 2001.
- [104] C. Caloz, C. C. Chang, Y. Qian, and I.Itoh, "A novel multilayer photonic band gap (PBG) structure for microstrip circuits and antennas," *IEEE –APS Dig.*, pp. 502-505, 2001.
- [105] A. K. Battacharya, "Analysis of multilayer infinite periodic array structures with different periodicities and axes orientations," *IEEE Trans. Antennas & Propagat.*, vol. 41, no. 10, pp. 371-378, Oct. 1993.
- [106] Y. L. Kuo, T. W. Chiou, and K. L. Wong, "A dual band rectangular microstrip antenna using novel photonic bandgap ground plane of unequal orthogonal periods," *Microwave and Optical Tech. Lett.*, vol. 30, no. 4, pp. 280-283, August 2001.



## Bibliography

---

- [107] M. Rahman, and M. A. Stuckly, "Wideband microstrip patch antenna with planar PBG structure," *IEEE –APS Dig.*, pp. 486-489, 2001.
- [108] N. Jin, A. Yu, and X. Zhang, "Enhanced 2 by 2 antenna array based on a dumbbell EBG structure," *Microwave and Optical Tech. Lett.*, vol. 39, no.5, pp. 395-399, Dec. 2003.
- [109] X. H. Shen, P. Delmotte, and G. Vandenbosch, "Enhancing the gain of microstrip antennas at different frequencies with one substrate –supersubstrate structure," *Microwave and Optical Tech. Lett.*, vol. 27, no.1, pp. 37-40, Oct. 2000.
- [110] R. Gonzalo, B. Martinez, P. Maagt, and M. Sorolla, "Improved patch antenna performance by using photonic bandgap substrate," *Microwave and Optical Tech. Lett.*, vol. 24, no.4, pp. 213-215, Feb. 2000.
- [111] M. Thevenot, M. S. Denis, A. Reineix, and B. Jecko, "Design of new photonic EBG to increase antenna directivity," *Microwave and Optical Tech. Lett.*, vol. 22, no. 2, pp. 136-139, July 1999.
- [112] J. Y. Park, C. C. Chang, and I. Itoh, "An improved low profile cavity backed slot antenna loaded with 2 D UC- PBG reflector," *IEEE –APS Dig.*, pp. 194-197, 2001.
- [113] X. J. Zhang, A. Q. Liu, M. F. Karim, A. B. Yu, and Z. X. Shen, "MEMS based photonic bandgap (PBG) bandstop filter," *IEEE-MTT-S Int. Microwave Sym. Dig.*, vol.1, pp. 1464- 1466, 2004.
- [114] L. H. Hsieh, and K. Chang, "Piezoelectric transducer bandstop filter," *Electronic Letters*, vol. 8, pp. 970-971, 2002.

## Bibliography

---

- [115] F. Martin, L. J. Carreras, and F. Falcone, "Frequency tuning in electromagnetic bandgap non linear transmission lines," *Electronic Letters*, vol. 39, pp. 440-442, 2003.
- [116] C. P. Wen, "Coplanar Waveguide: A Surface Strip Transmission Line Suitable for Nonreciprocal Gyromagnetic Device Applications," *IEEE Trans. Microwave Theory Tech.*, vol. 17, No. 12, pp. 1087—1090, Dec. 1969.
- [117] J. L. B. Walker, "A Survey of European Activity on Coplanar Waveguide," *1993 IEEE MTT-S Int. Microwave Symp. Dig.*, vol. 2, pp. 693—696, Atlanta, Georgia, June 14—18, 1993.
- [118] A. K. Sharma and T. Itoh (Editors), Special Issue on Modeling and Design of Coplanar Monolithic Microwave and Millimeter-Wave Integrated Circuits, *IEEE Trans. Microwave Theory Tech.*, vol. 41, no. 9, Sept. 1993.
- [119] T. Sporkmann, "The Evolution of Coplanar MMICs over the past 30 Years," *Microwave Journal*, vol. 41, No. 7, pp. 96—111, July 1998.
- [120] T. Sporkmann, "The Current State of the Art in Coplanar MMICs," *Microwave J.*, vol. 41, no. 8, pp. 60—74, Aug. 1998.
- [121] J. Browne, "Broadband Amps Sport Coplanar Waveguide," *Microwaves RF*, vol. 26, No. 2, pp. 131—134, Feb. 1987.
- [122] Technology Close-Up, *Microwaves RF*, vol. 27, no. 4, p. 79, April 1988.
- [123] J. Browne, "Coplanar Waveguide Supports Integrated Multiplier Systems," *Microwaves RF*, vol. 28, no. 3, pp. 137—138, March 1989.
- [124] J. Browne, "Coplanar Circuits Arm Limiting Amp with 100-dB Gain," *Microwaves RF*, vol. 29, no. 4, pp. 213—220, April 1990.

## Bibliography

---

- [125] J. Browne, "Broadband Amp Drops through Noise Floor," *Microwaves RF*, vol. 31, no. 2, pp. 141—144, Feb. 1992.
- [126] C. Veyres and V. F. Hanna, "Extension of the Application of Conformal Mapping Techniques to Coplanar Lines with Finite Dimensions," *Int. J. Electron.*, vol. 48, no. 1, pp. 47—56, Jan. 1980.
- [127] S. Gevorgian, L. J. P. Linner and E. L. Kollberg, "CAD Models for Shielded Multilayered CPW," *IEEE Trans. Microwave Theory Tech.*, vol. 43, no. 4, pp. 772—779, April 1995.
- [128] D. Peroulis, S. P. Pacheco, K. Sarabandi, and L. P. B. Katehi, "Electromechanical considerations in developing low voltage RF MEMS switches," *IEEE Trans. Microwave Theory Tech.*, vol. 51, no. 1, pp. 259—270, Jan. 2003.
- [129] A. B. Yu, A. Q. Liu and Q. X. Zhang and H. M. Hosseini, "Effects of surface roughness on electromagnetic characteristics of capacitive switches," *Journal of Micromechanics and Microengineering*, vol. 16, pp. 2157-2166, 2006
- [130] A. B. Yu, A. Q. Liu, X. Q. Zhang, L. Zhu, A. Alphones and S. A. Peter, "Improvement of isolation for RF MEMS capacitive shunt switch via membrane planarization," *Sensors & Actuators Physics A*, vol. 19, pp. 206-213, 2005.
- [131] Ansoft High Frequency Structure Simulator, Release 8.0.21, Ansoft Corporation, 2001.
- [132] S. G. Mao, M. Y. Chen, "Propagation characteristics of finite width conductor backed coplanar waveguides with periodic electromagnetic bandgap cells," *IEEE Trans. Microwave Theory. Tech.*, vol. 50, pp. 2624-2628, Nov. 2002.

## Bibliography

---

- [133] M. F. Karim, A. Q. Liu, A. Alphones and A. B. Yu, "A tunable bandstop filter via the capacitance change of micromachined switches," *Journal of Micromechanics and Microengineering*, vol. 16, no. 4, pp. 851-861, 2006.
- [134] R. Clarke, C. B. Rosenberg, "Fabry-Perot and open resonators at microwave and millimeter wave frequencies, 2-300 GHz," *J. Physics Sci. Instrum.*, vol. 15, pp. 9-23, 1982.
- [135] Jose. Correia, *Optical microsystem in silicon based on a Fabry-Perot resonance cavity*, Delft University Press, 1999.
- [136] H. Cam, S. Toutain, and G. Landrac, "Study of a Fabry-Perot cavity in the microwave frequency range by boundary element method," *IEEE Trans. Microwave Theory Tech.*, vol. 40, pp. 298-304, Feb. 1992.

## AUTHOR'S PUBLICATION

### **JOURNAL PAPERS**

- [1] M. F. Karim, A. Q. Liu, A. Alphones, and A. B. Yu, "A reconfigurable micromachined switching filter using periodic structures, " *IEEE Transaction on Microwave Theory & Tech.*, vol. 55 , no 6, pp. 1154-1162, June 2007.
- [2] M. F. Karim, A. Q. Liu, A. B. Yu and A. Alphones, "Micromachined tunable filter using fractal electromagnetic bandgap (EBG)," *Sensors and Actuators A*, vol. 133, pp. 355-362, 2007.
- [3] M. F. Karim, A. Q. Liu, A. Alphones and A. B. Yu, "A tunable bandstop filter via the capacitance change of micromachined switches," *Journal of Micromechanics and Microengineering*, vol. 16, no. 4, pp. 851-861, 2006.
- [4] M. F. Karim, A. Q. Liu, A. B. Yu, A. Alphones, and X. J. Zhang, "CPW bandstop filter using unloaded and loaded EBG structures," *IEE Proceedings on Microwave and Antenna Propagation*, vol. 152, no. 6, pp. 434-440, 2005.
- [5] M. F. Karim, A. Q. Liu, A. Alphones, Y. H. Lee and X. J. Zhang, "Low Pass Filter with Nonuniform EBG," *Microwave & Optical Technology Letters* , vol. 45, pp. 94-96, April 2005, USA.

### **CONFERENCES PAPERS**

- [1] M. F. Karim, A. Q. Liu, A. Alphones and A. B. Yu, "A novel reconfigurable filter using periodic structures," *International Microwave Symposium, IEEE Microwave Theory and Techniques Society (MTT-S)*, San Francisco, USA, 11-16 June, 2006.

- [2] M. F. Karim, A. Q. Liu, A. Alphones and A. B. Yu, "MEMS-based tunable bandstop filter using electromagnetic bandgap (EBG) structures," *Asia Pacific Microwave Conference (APMC) proceedings*, vol. 3, Dec 4-7, 2005.
- [3] M. F. Karim, A. Q. Liu, A. Alphones and A. B. Yu, "Fractal CPW EBG filter with nonlinear distribution," *Asia Pacific Microwave Conference (APMC) proceedings*, vol. 3, Dec 4-7, 2005.
- [4] M. F. Karim, A. Q. Liu, A. Alphones and A. B. Yu, "Micromachined tunable bandstop filters for wireless sensor networks," *IEEE Sensors*, USA, pp. 151-154, 30 October- 3 November, 2005.
- [5] X. J. Zhang, A. Q. Liu, M. F. Karim, A. B. Yu, Z. X. Shen, "MEMS based photonic bandgap (PBG) bandstop filter," *IEEE Microwave Theory and Techniques Society Digest (MTT-S)*, Boston, USA, pp. 1463-1466, 8-12 June 2004.
- [6] M. F. Karim, A. B. Yu, Y. H. Lee, A. Q. Liu, "MEMS-based-photonic bandgap using non-uniform period structure," *Conference of Design, Test, Integration and packaging of MEMS*, Switzerland 2004.
- [7] M. F. Karim, Y. H. Lee, A. Agarwal and A. Q. Liu, "Switchable MEMS Parallel Coupled Filter," *Asia-Pacific Conference of Transducers and Micro-Nano Technology*, vol 3, pp. 1038-1041, Japan 2004.
- [8] M. F. Karim, Y. H. Lee, A. Agarwal and A. Q. Liu, "Aperiodic Band Gap Structure Using MEMS Technology," *Asia-Pacific Conference of Transducers and Micro-Nano Technology*, vol 3, pp. 483-487, Japan 2004.